Thermal Sprayed Coating as a Structural Health Monitoring Sensor for Engineering Structures

by

Adekunle Sulaimon Ogunbadejo

A thesis submitted in partial fulfillment of the requirements for the degree of

Doctor of Philosophy

Department of Mechanical Engineering

University of Alberta

Abstract

Failure prevention in engineering components is vital to efficiently reducing costs and very crucial to preservation of lives. Crucial to this failure prevention is the requirement of knowing stresses within the components, not just to counter the risk of overloading but also to determine the onset of failure, and thus influence its economic and social consequences. Given the economic importance of failure, more emphasis should be placed on developing more effective and economically viable solution to failure prevention. In this doctoral research program, the main objective was to develop thermally sprayed coatings for use as structural health monitoring (SHM) sensors to monitoring in-service stresses through electromechanical measurements. The components of focus are wind turbine blades and pipes used in oil and gas. Mechanical blend of a nickel alloy (NiCoCrAlTaY) powder and titania (TiO_2) powder was used to fabricate flamed-sprayed coatings on steel plates, steel pipes and carbon fiber reinforced composite (CFRP) plates. The choice of the powder mixture was to optimize the piezoresistive response of the coating layer. To prevent electrical short circuiting of the bi-layered coating-substrate system, a flame-sprayed alumina (Al_2O_3) was deposited on all the substrates before depositing the conductive layer.

In the first stage of the experimental study, the impact of TiO_2 on the porosity, electrical resistivity, and gauge factor of NiCoCrAlTaY coating was investigated. Both tensile and cyclic tests were performed to investigate the piezoresistive sensitivity of the conductive layer on steel plates. To investigate the effectiveness of the coating to monitor stresses in pressurize vessel, experimental study was also conducted through internal pressurization with hydraulic oil at different pressures with the coating on steel pipes. Since the current trends in wind turbine blades fabrication is heavily tilted towards utilization of composites, tensile tests were carried out on CFRP coated with the nickel alloy through flame spray technique. The results suggested that the

coatings can perform as good surface strain monitoring sensors in steel and CFRP substrates. The gauge factor of the coating, which is a measure of strain sensitivity, reached 4.2 and 146 on CFRP and the steel substrates, respectively.

The second stage of the research involved using analytical modelling techniques to investigate the electromechanical interaction of the conductive layer with an elastic substrate in the bi-layered coating-substrate system. Effective material properties were used for the coating and the substrate was modelled as an elastic half-plane. Subsequently, analytical investigation was done on the effect of imperfect interfaces in the form of delamination and the effects of bending on the piezoresistive response of the coating-substrate system. Through the analytical model of the system, the strain distributions in each layer in the bi-layered coating-substrate system was established. Also, the load transfer mechanism, which plays a significant role in establishing the transfer function between substrate and the conductive layer, revealed that load transfer from the substrate to the conductive layer was mainly through the edges of the insulating layer .

Preface

The parts of Chapter 2; Sections 2.1.2, 2.1.3, 2.1.6, 2.1.7, 2.1.8, 2.2.1, and 2.2.4 regarding NiCoCrAlTaY coated on flat steel substrate has been published in:

A. Ogunbadejo, S. Chandra, A. McDonald, "Flame-sprayed NiCoCrAlTaY coatings as damage detection sensors", in: *International Thermal Spray Conference*, May 4–6, 2022 (Vienna, Austria), DVS-The German Welding Society, (2022), 6 pages on compact disk.

The parts of Chapter 3; Sections 3.1.1 and 3.2.1 regarding mathematical modelling of the interfacial stress within the bi-layered coating layer has been published in:

A. Ogunbadejo , S. Chandra, A. McDonald, "Analytical and numerical modelling of interfacial stress distribution of a piezoresistive coating layer ", in: *International Thermal Spray Conference*, May 24-27, 2021 (Québec City, Canada), ASM International, (2021), 6 pages on compact disk.

Acknowledgements

I would like to express my heartfelt appreciation to my esteemed supervisors, Professor André McDonald and Professor Sanjeev Chandra, for their unwavering guidance, support, and exceptional mentorship throughout my doctoral program. Their insights and expertise have been invaluable in helping me navigate my research data and present meaningful and insightful findings to the academic community. I would like to extend a special thanks to Professor McDonald for offering me the valuable opportunity to join his research group and for his patience and understanding during the challenges I encountered throughout my PhD program.

I am also immensely grateful to my research colleagues Sanhita, Saddam, and my former research colleague, Dr. Rakesh Bhaskaran Nair, for their unwavering support and encouragement in the laboratory. And our laboratory manager, Dr. Maria Ophelia Jarlingo, who always provided very valuable insights. I would also like to thank Jerry Han, my former research colleague, for being a constant source of support during challenging times. I am deeply appreciative of Steve Okocha, who has always been willing to listen and help alleviate difficult situations.

I am so grateful to Dr. Ramgopal Ramaraju for his technical support during my research visit to the University of Toronto (UofT), as well as the Centre for Advanced Coating Technologies staff and my colleagues at UofT.

My wife, Wakeelat Ogunbadejo, and my son, Mateen Ogunbadejo, are the center of my world and a constant source of joy in my life. I am also deeply grateful for the care and love provided by my mother, Mrs. Adesola Ogunbadejo, who has been an unwavering source of inspiration to me. She has dedicated her life to ensuring that her children become upstanding citizens and valuable contributors to society.

Table of Contents

List of Tables

List of Figures

Chapter 1

Introduction

1.1 Background

Damage can be described as changes to material or geometric properties of an engineering component or system that affect its performance. It is a fated phenomenon in engineering structures, and with influence from service conditions or environmental factors, it is susceptible to progressive accumulation and propagation [1, 2]. This implies that damage results in a significant deviation from a reference state where the system is considered healthy (undamaged state) to an unhealthy one. This could be significant enough to lead to failure of engineering components and subsequently causing unscheduled maintenance and shutdowns, litigation disputes and even fatal accidents. In 1978, the financial loss to material fracture alone was estimated to be $88 billion per year in the United States of America; about 4 percent of the gross national product [3]. This is equivalent to $358 billion per year in 2020 dollar [4]. Also, about 40% of failure cases have also been attributed to unserviceability of structural components [5]. Aside from that , failure of these components could be unforeseen because of complex material stresses and properties, the difficulty, in terms of cost and design, of implementing real-time structural health monitoring (SHM) of components is also one of the major hurdles.

Thus, the detection of damage at an early stage is crucial to the functionalities and service lives of structural systems such as wind turbine blades, pressure vessels, bridges, to mention a few. There are a few techniques employed in assessing the integrity of engineering components. These structural assessments and monitoring procedures have been based on strain measurements, acoustic emission, ultrasound, vibration, and thermography [6, 7]. They have been implemented

to monitor damages in mechanical parts; such parts of automobiles subjected to vibrations, aerospace application; wings of aircrafts, and civil engineering application, such as bridges [1, 6, 8, 9]. By extension, they have been used to significantly reduce lifecycle cost, minimize inspection time, and prevent unnecessary replacement of components. Despite these advantages, they usually require highly skilled inspectors to run, they are expensive, and most are not suitable for remote and real time monitoring [10].

One of the common ways of monitoring the occurrence and development of damage is strain-based approach [6]. In this approach, strain values or strain parameters such as strain energy and frequency response are directly affected by a physical property in the material due to an external load [11]. The response of this specific property, which is proportional to the strain-based parameter is then measured and analyzed. Some advantages of using strain measurement-based detection are that strain signals are sensitive enough to assess structural damages or failures and estimate damage sizes [7, 12]. For example, the strain rate of the wind turbine blade structure can be used to measure crack initiation caused by higher strain loads [13] while strain values and electrical resistance from surface piezoresistive gauges have also been used to detect delamination of a composite rotor blade and creep of engine compressor rotor blades, respectively [14].

In this regard, piezoresistive sensors work on the principle of change in electrical resistance due to an external load applied to the sensor. They have emerged as a damage monitoring need in structures because of their high sensitivity, fast signal response, low manufacturing cost and adaptability [15, 16]. These vital characteristics are part of the reasons why they have great application potential for on-line monitoring [6, 17], thus potentially providing an accurate predetermined schedule of service and inspection of engineering structures and systems. However, the identified gaps regarding their usage include relatively low sensitivity for the metallic strain

gauges, high hysteresis especially after sustaining few load cycles and temperature limitations for the adhesively bonded gauges. Also, at high interfacial stress, the adhesive bonded gauges could delaminate from the component they are monitoring thus giving false strain readings.

To mitigate these short falls, this research explores the viability of a thermally sprayed piezoresistive coating sensor. This is because thermal spray coatings have the flexibility of being fabricated to close these gaps. Traditionally, coatings have provided a wide range of functionalities such as protection against wear, corrosion, fire, and have also served aesthetic functions. Though most of these traditional applications of coatings are mostly done as an after-thought exercise to structural components, they have prolonged lives of the components with good efficiency [18, 19]. However, coatings are finding more crucial functionalities in the design of components than their traditionally passive protective capabilities. Thermal spray coatings are in this class of functional coatings [20]. They are fabricated by depositing heated and accelerated spray materials in the form of powder, wire, liquid or suspension on a selected substrate. The feedstock material, which would be in molten or partly molten state, after exiting the nozzle of the spray touch, are deposited on the surface of a target substrate (Fig. 1-1), thus, giving a structurally integrated coating-substrate system.

In the case of a structural health motoring (SHM) sensor design, this proper integration of the coating-substrate system is fundamental to efficient load transfer between the substrate and the coating. Thus, with good control of the spraying conditions of a thermal spray process, a thermally sprayed coating could be employed as a simple, yet effective real time SHM sensor for the components it is integrated with. A property of the coating such as electrical resistance that reliably varies against stress or strain in the component would be adopted in monitoring the state of the component. This cross-property relationship, which relies on both the physical properties of the

coating and substrate, will be effective in designing a sensor that will provide reliable feedback on the health of the engineering component on which it is monitoring.

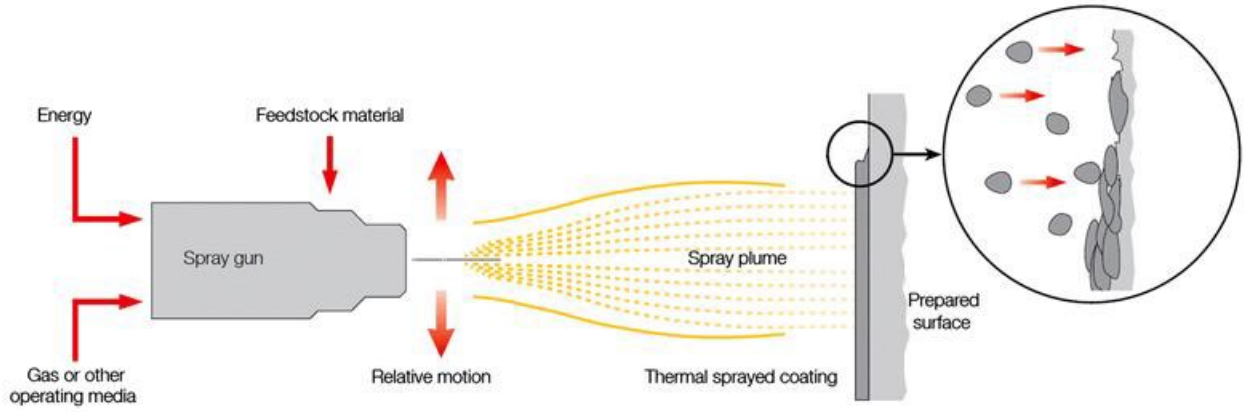

Figure 1-1 Schematic of the thermal spray process [21]

1.2 Mechanical Properties of Thermally Sprayed Coatings

Thermal spraying techniques are coating processes that apply metallic or non-metallic melted (or heated) coatings on a prepared surface. Energy sources are used to heat the coating precursor (which could be in powder, wire, or rod form) to a molten or partially molten state before their interaction with the prepared surface [21].

During thermal spraying, the interaction of sprayed particles with the substrate is carefully controlled through the spraying parameters such as oxygen/acetylene ratio, powder feed rate, velocity of spray particles, plasma power, stand-off distance, transverse velocity, arc voltage and current. A successful deposition of the thermally sprayed coating usually results in the formation of a unique lamellar microstructure [22 - 26]. The lamellar microstructure is due to the layered splat formation because of successive impact of molten droplets on the surface of the substrate

[27]. The microstructure contributes to the anisotropic mechanical properties of the thermally sprayed coating.

This unique microstructure is different from other conventional coating processes such as electrostatic coating, electrodeposition, physical and chemical vapor deposition. Therefore, thermally sprayed coatings generally have mechanical properties that are quite different from the coating processed through these aforementioned processes. These properties are easily influenced by a change in the properties of the spray material or a change in the spray process conditions. In other words, the mechanical properties of the same coating material will be different with different particle size of starting material, different combinations of spray parameters or thermal spray technique employed. Thus, the flexibility to influence the mechanical properties of the thermally sprayed coating. With respect to this, a lot of effort has gone to using spray parameters and post spraying techniques to manipulate the mechanical properties of deposited coatings for target applications. This will be discussed in the next paragraphs.

With the objective of comparing the mechanical performance of thermally sprayed nanocrystalline Cr_3C_2-25(Ni20Cr) powder and its conventional counterpart, high-velocity oxyfuel (HVOF) technique was used to deposit both range of particle sizes. And with the same spray parameters, it was found out the hardness of coating fabricated from nanocrystalline powder was 20 % higher than the one from the conventional micro-sized powders [23] (Table. 1-1). Also, the surface roughness was 40 % lower while the elastic modulus and fracture toughness were roughly the same. In their atmospheric plasma spraying (APS) of Fe-based powder, Kumar, *et al.* [28] found out that varying the plasma power and number of passes of APS system have significant effects on the porosity, thickness, and devitrification of the resulting coating. Still on using deposition parameters to influence coating properties, Movahedi, *et al.* [29] also showed how

varying the fuel/oxygen ratio affects the crystallization characteristics of the mechanically alloyed amorphous Fe-Cr-Mo-P-B-C-Si powder during HVOF spraying, thereby affecting its mechanical properties.

Table 1-1 The mechanical properties of the two types of Cr_3C_2-25(Ni20Cr) [23]

Properties	**Crystalline Cr_3C_2-25 (Ni20Cr) powder**	**Conventional Cr_3C_2-25 (Ni20Cr) powder**
Roughness(μm)	4.72 ± 0.22	16.43 ± 0.45
Elastic modulus (GPa)	193 ± 19	195.5 ± 22
Hardness (MPa)	11,400 ± 65	9786.6 ± 100
Indentation toughness ($MPa.m^{-1/2}$)	2.75 ± 0.50	2.73 ± 0.50

`Aside from the spray parameters, some post-deposition can also improve specific mechanical properties of the thermally sprayed coating. Friction stir processing (FSP) has been used to refine the microstructure of high-velocity flame spray (HVFS) Ni-Cr-Al_2O_3 coatings on 316L stainless steel. The processed coating showed nearly two times enhancement in its microhardness compared to as-spayed coating along with increase in fracture toughness [30] (Fig. 1-2).

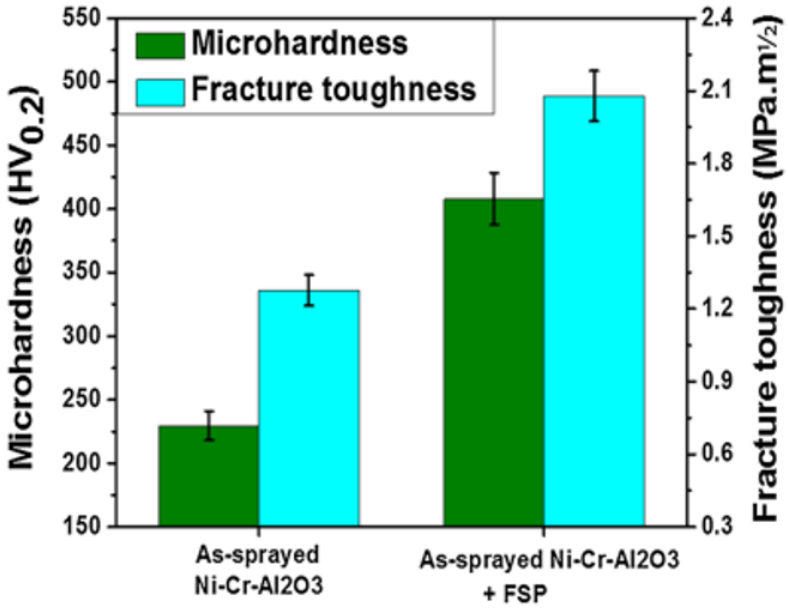

(a)

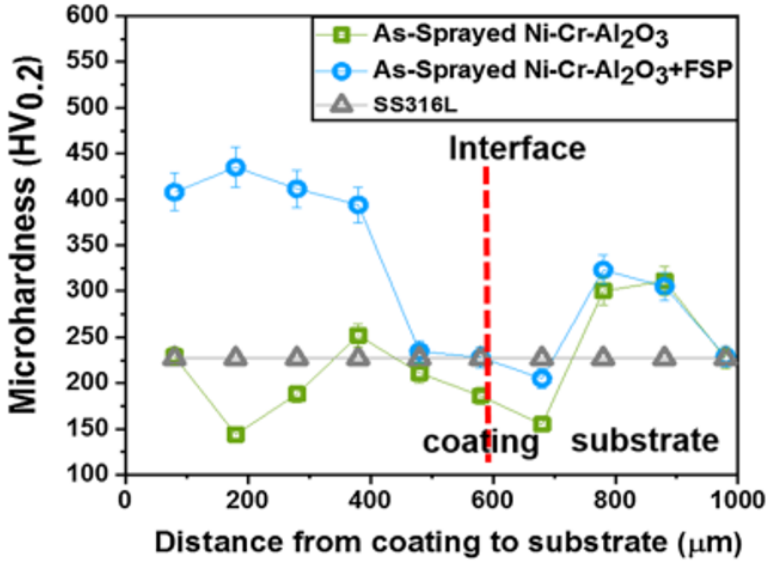

(b)

Figure 1-2 Plots showing (a) average surface microhardness and fracture toughness, and (b) variation of microhardness across the coating depth of HVFS as-sprayed and FSPed Ni-Cr-Al_2O_3 coating [30]

Also, conducting cold and hot pressing on flame-sprayed aluminium, Al and mechanically blended aluminium powders and silicon carbide, SiC particles (Al/SiCp) decreased and increased their porosities and wear resistance, respectively. Fig. 1-3 to Fig. 1-6 showed how the porosities and wear of these two processes compare to the as-sprayed coatings. It is glaring from these figures that the post-deposition processes can have a great influence on the microstructure of the deposited coating.

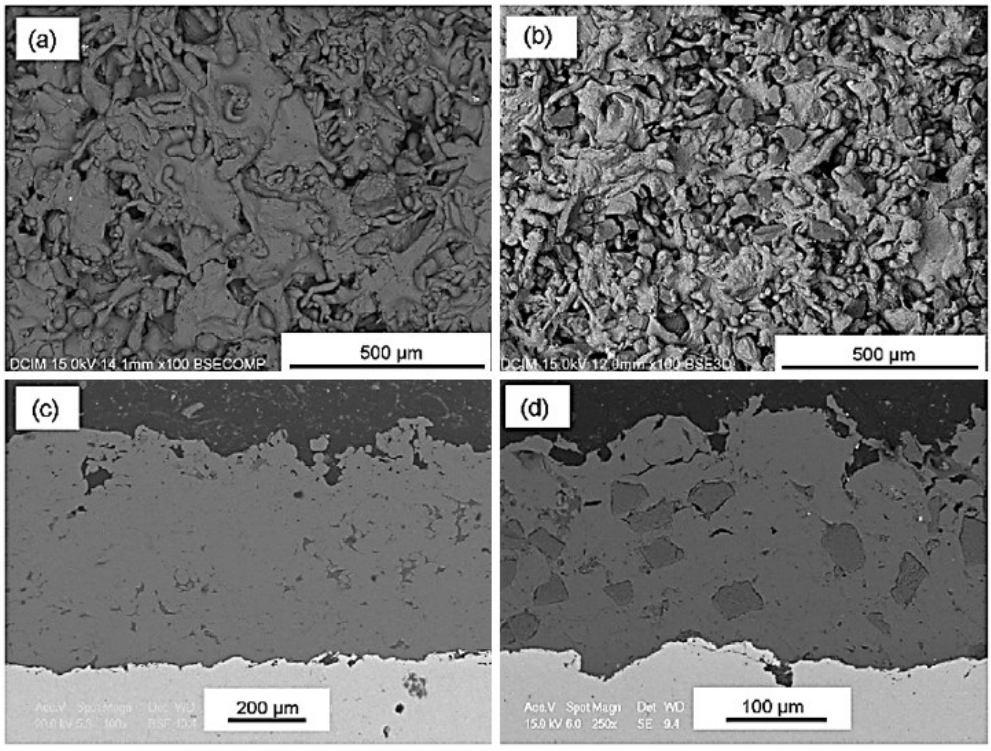

Figure 1-3 Top view of the as-sprayed (AS) coatings: (a) pure aluminium; (b) Al/SiCp composite; cross-section of the (c) pure aluminium and (d) Al/SiCp composite [31]

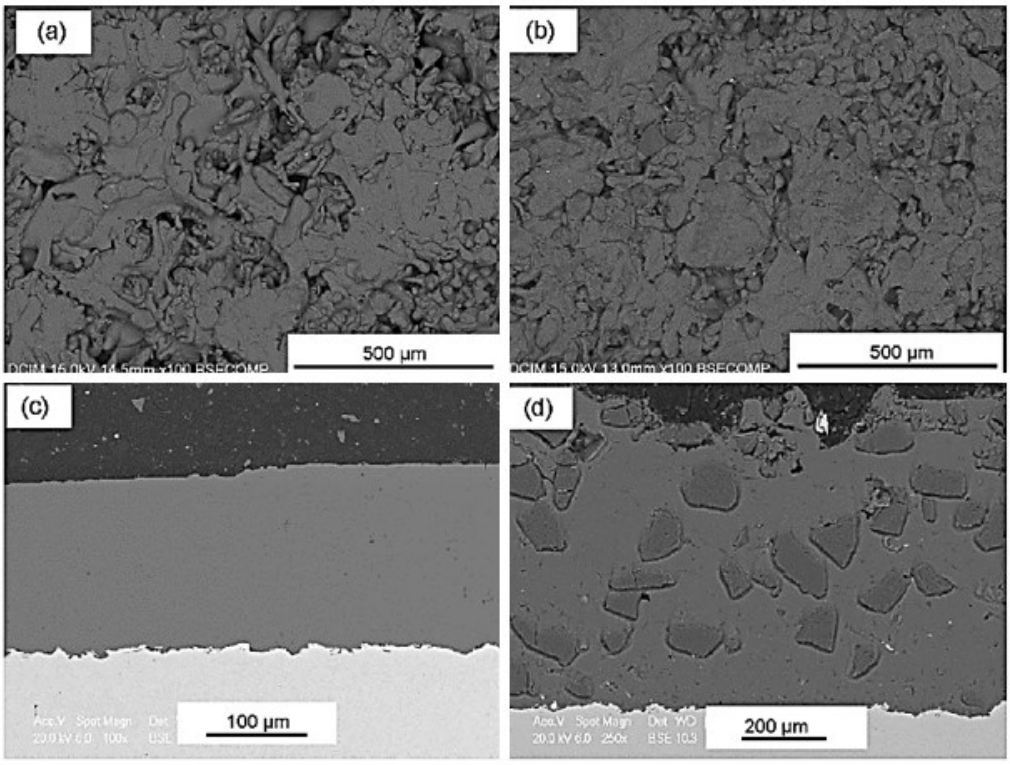

Figure 1-4 Top view of the cold-pressed (CP) coatings: (a) pure aluminium; (b) Al/SiCp composite; cross-section of the (c) pure aluminium and (d) Al/SiCp composite [31]

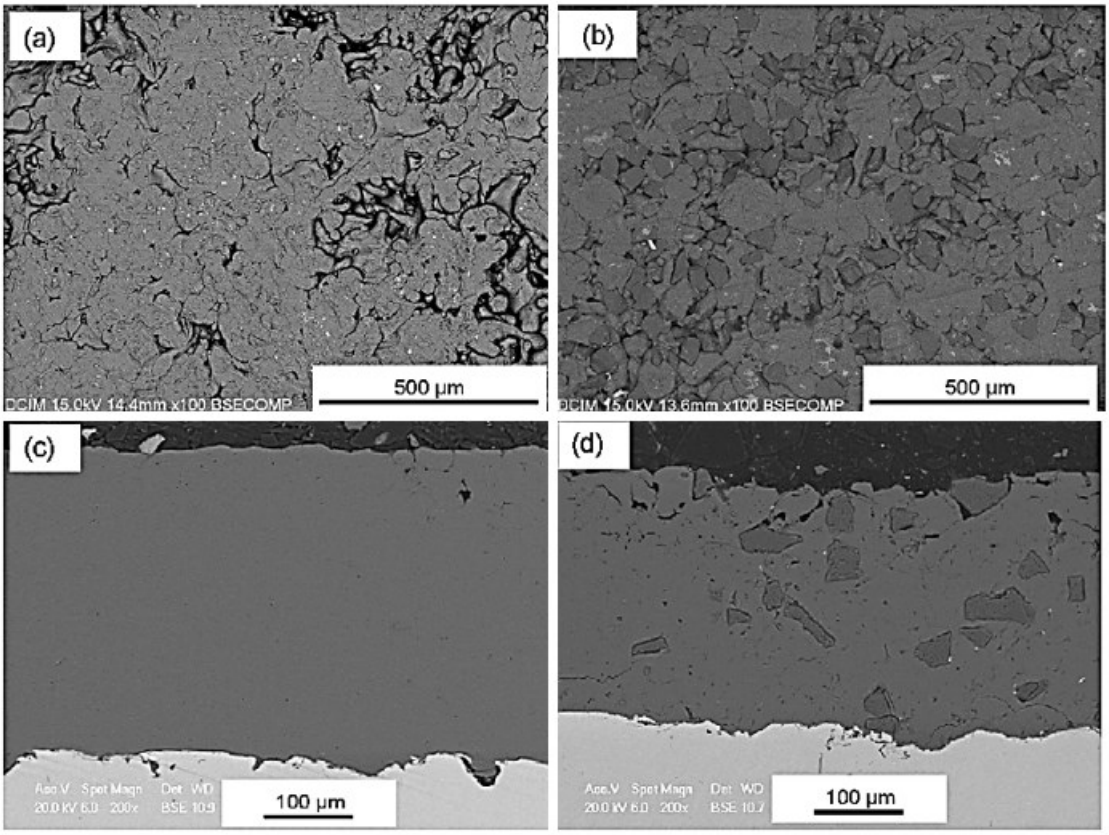

Figure 1-5 Top view of the hot-pressed (HP) coatings: (a) pure aluminium; (b) Al/SiCp composite; cross-section of the (c) pure aluminium and (d) Al/SiCp composite [31]

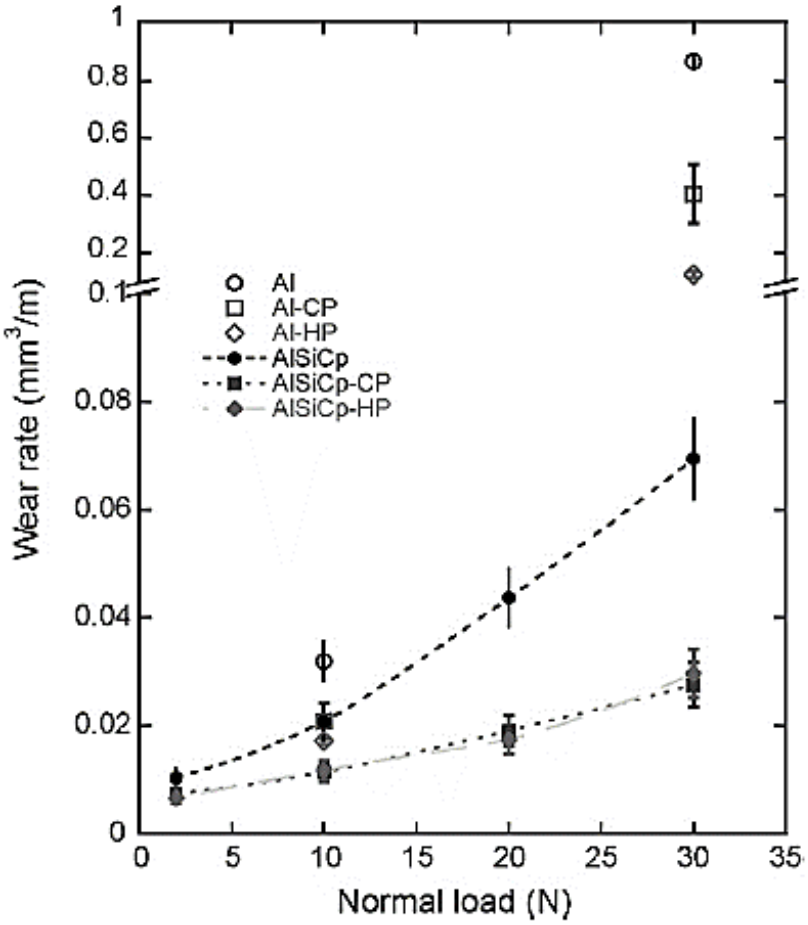

Figure 1-6 Wear rate versus normal load obtained from ball-on-disc wear tests of pure aluminium and Al/SiCp composite coatings for different post-spraying processes: no treatment (AS), cold-pressed (CP) and hot-pressed (HP) [31]

1.3 Electrical Properties of Thermally Sprayed Conductive Coatings

Just as different thermal spray techniques produce different mechanical properties of the coating with the same starting material, the electrical properties of a coating can also be affected by any change in spraying conditions. Brandland, *et al.* [32] established that the electrical resistivity of the plasma sprayed titania coatings increased when distance between structural defects was of the same order as the mean free path of the charge carriers. They were also able to

show how the titania particle temperature at impact vary with the resistivity of the coating (Fig. 1-7).

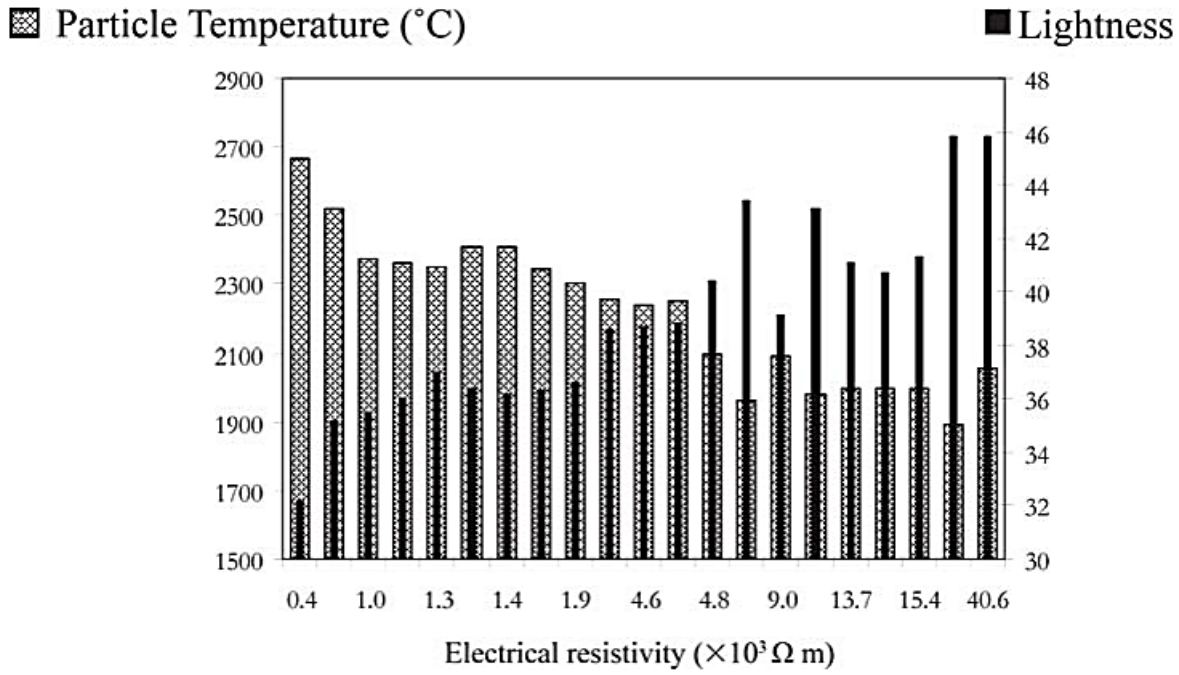

Figure 1-7 Variation of APS TiO_2 coatings electrical resistivity with particle temperature at impact (white bar) and lightness value (black bar) of coatings [32]

While slight variation in spray parameters for a particular feed stock could significantly affect the electrical properties of a thermally sprayed coating, it has been shown in another work that using different thermal spray deposition techniques on a particular feedstock might significantly affect its electrical properties. This has been shown by Sharma *et al.* [27] in their deposition of Ni-Al coating through 4 different thermal spray deposition techniques; air plasma spray (APS), twin wire-arc (TWA), high velocity oxy-fuel (HVOF) and cold spray (CS). It was observed that Ni-Al coating sprayed through APS and CS showed comparable values of electrical resistivities despite the vast difference in their porosities and oxide contents. However, in the same

work, Ni-Al sprayed through HVOF has much lower resistivity than that sprayed through CS despite slight differences in their porosities and oxide contents. Further, Ni-Al sprayed through TWA has about half the resistivity of APS despite showing similar porosity and oxide content. Other researchers also experimented with thermally deposited Ni and Ni-20Cr resistors [33, 34] (Fig 1-8) to fabricate heating plate and found the resistivities of the coatings to increase and decrease, respectively after annealing at temperatures in the range 200 to 400 ^{o}C. This was attributed to the healing of structural defects and ordering of atoms of the coatings, respectively.

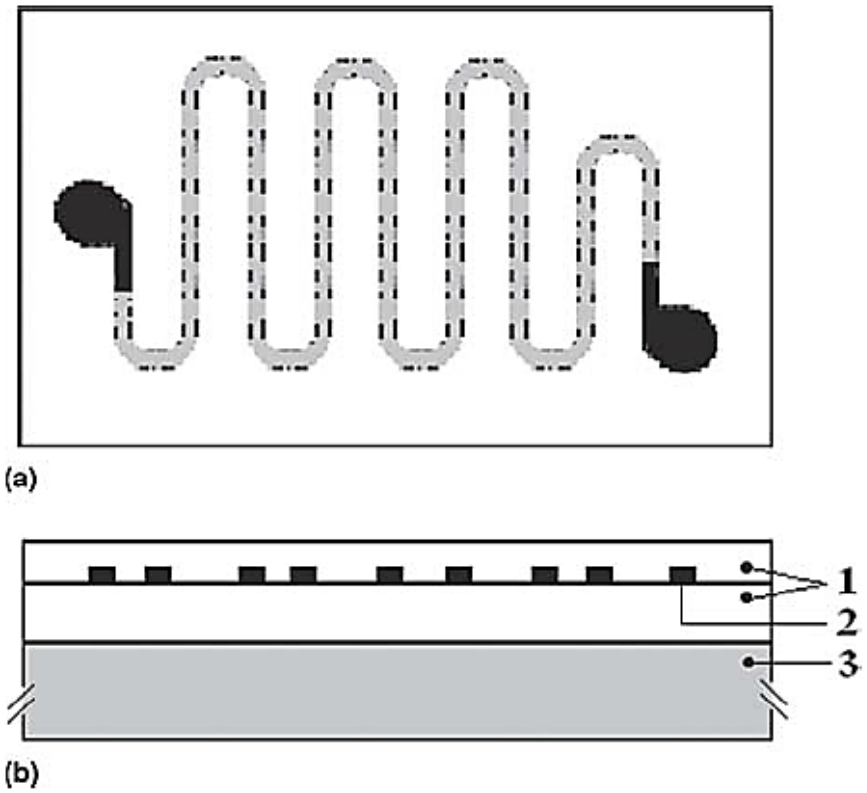

Figure 1-8 Heating plate design consisting of (1) alumina coatings, (2) heating meander, and (3) metal coupon (substrate) from (a) top view and (b) cross-sectional view [33, 34]

1.4 The Potential of Thermally Sprayed Coatings as Structural Health Monitoring Piezoresistive Sensors

There are electrically conductive coatings that have been fabricated through different thermal spray processes that can potentially serve as SHM sensors. Thin Al coatings were fabricated through flame spray and deposited on cured glass and basalt (Fig. 1-9) [35]. It was concluded that an SHM system of the coating-polymer system, with electrical resistance as the monitoring parameter, is possible with the right selection of coating materials and spray parameters; the sensitivity (measured through gauge factor) of fabricated coating could be increased by careful manipulation of spray parameters.

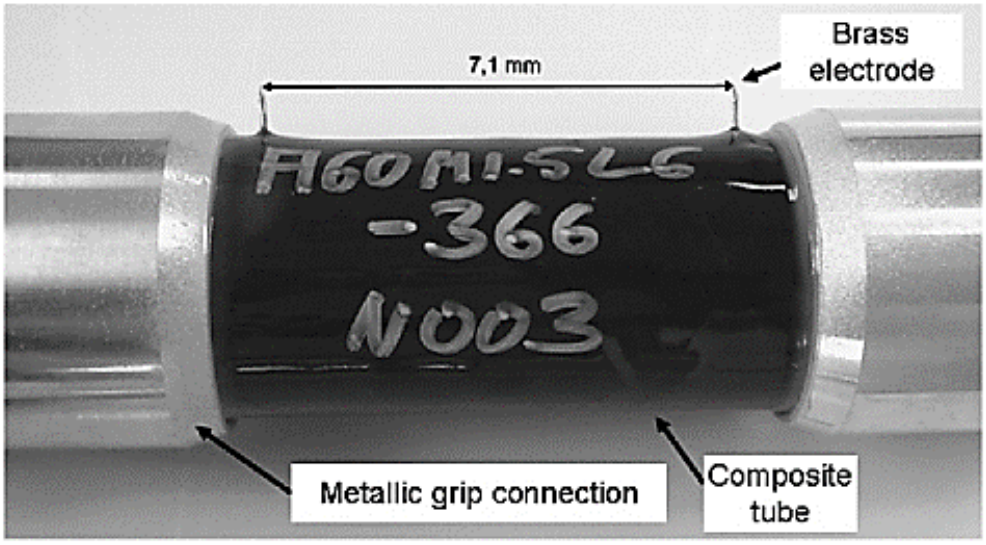

Figure 1-9 Basalt fiber composite specimen with embedded aluminum coating [35]

In the same vein, Fasching, *et al.* [36] investigated the potential of thermally sprayed zinc as strain gauge sensor (Fig 1-10). In their work, the electrical resistance of the thermally sprayed gages changed in response to applied strain, but the coating remained deformed after removal of the stress. This was attributed to excessive oxidation and poor cohesive bonding of the sprayed

zinc and a recommendation to either use better spraying conditions, material with suitable properties or appropriate postprocessing of the sprayed coating was suggested.

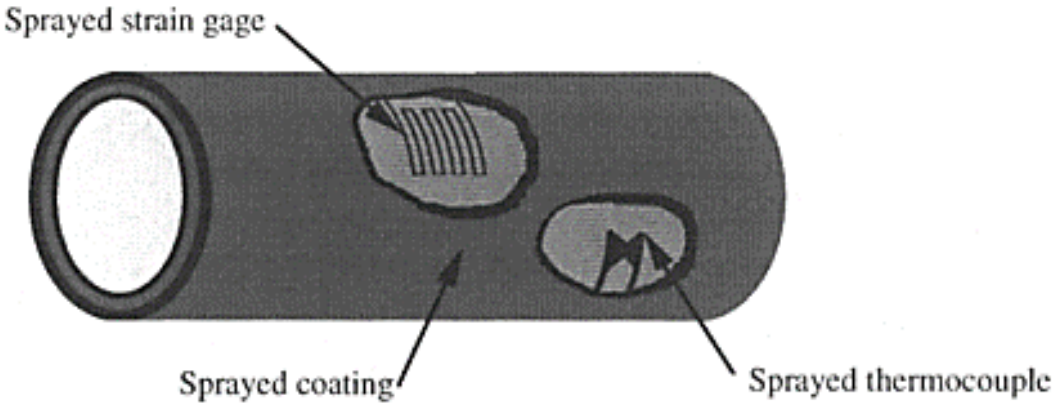

Figure 1-10 Thermally sprayed coating with embedded thermally sprayed zinc sensors [36]

A notable advantage of using thermal spray coating in sensory functions is that the production and the installation of the sensor occur simultaneously, saving time on installation and allowing for a straightforward sensor fabrication. With this advantage, using masking materials before spraying the coating further brings a huge flexibility to the sensor such that it can be individually designed for a particular application. Further adding to this flexibility is that the advantage of improving a target property of the coating through the mechanically blending with another material before spraying. In this light, the thermal and electrical response of thermal-spray E-type thermocouples consisting of 62Cu/38Ni and 80Ni/20Cr which is similar to the industry standard E-type composition of constantan (60Cu/40Ni) and chromel (90Ni/10Cr) was measured over temperatures ranging from ambient up to 900^{o}C, and the results were comparable with industry-

standard E-type thermocouples [37, 38]. The lead wires were integrated with the gauge pattern as shown in Fig. 1-11.

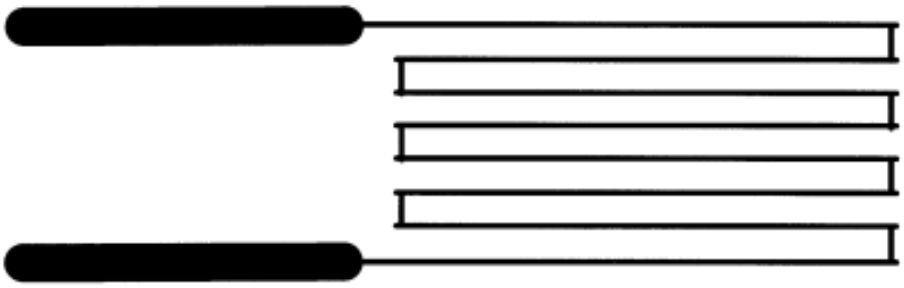

Figure 1-11 Schematic of strain gauge layout with the integrated lead fabricated at same time as gauge pattern [37]

Gonzalez, *et al.* [39, 40] researched the suitability of thermally sprayed Al-12Si as a piezoresistor on a fiber reinforced polymer composite (FRPC) substrate (Fig. 1-12). The potential of the sprayed Al-12Si coating for detecting strain induced damage was found to be limited to the late stages of failure [39, 40], where fibre breakage and delamination affect the integrity of the FRPC structure. A higher sensitivity of the coating was proposed by selecting an appropriate coating material.

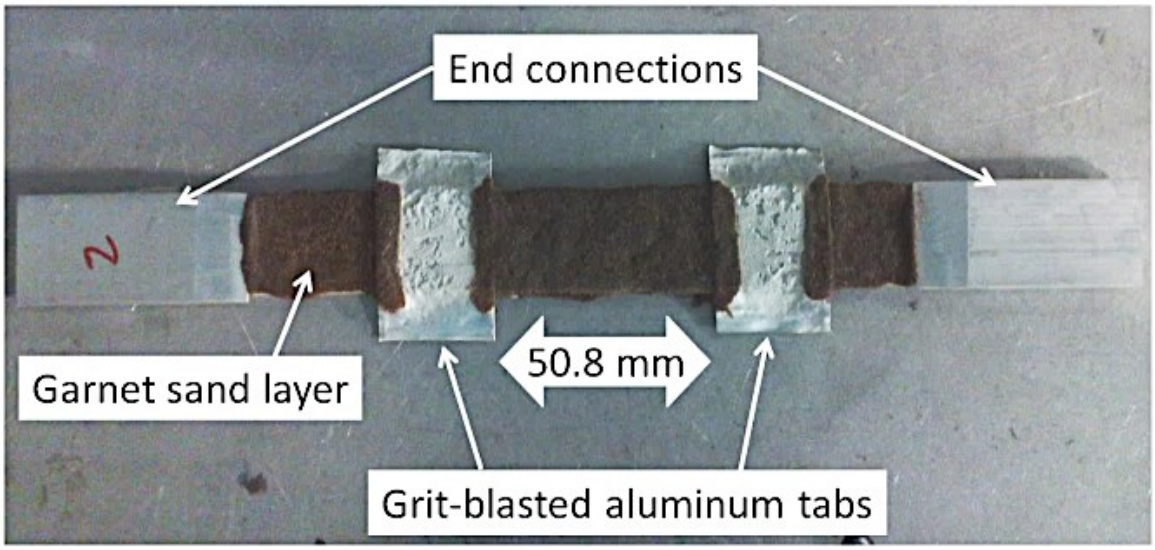

Figure 1-12 Composite specimen prior to flame spray deposition of Al-12Si [39, 40]

1.5 Modelling of Piezoresistive Response of Thermally Sprayed Sensors

For a comprehensive damage detection protocol, fabrication of the sensor is most times accompanied by modelling techniques. In this regard, different modelling techniques have attempted to predict the response of piezoresistive sensors. Panozo, *et al.* [41] developed an analytical model to predict the piezoresistive response of carbon nanotube (CNT) filled polymers. The model, which took into consideration the elongation and lateral contraction of the CNT when uniaxial load is applied (Fig. 1-13), considered the variation of the electrical tunneling resistance and morphological parameters such as topology of the nanotubes, their waviness and degree of entanglement [41].

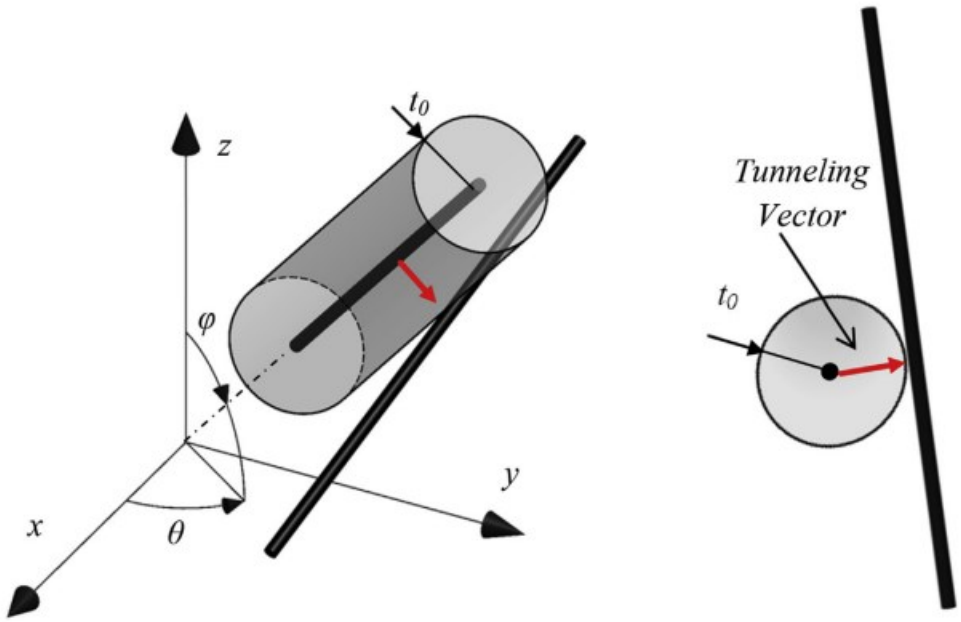

Figure 1-13 Schematic of the reciprocal position of adjacent CNTs prospective view (left) and cross-sectional view (right) [41]

Numerical simulation was also utilized in optimizing the piezoresistive behaviour CNT filled polymers to establish the electrical property-strain relationship of the CNT's [42]. The analysis showed there is potential in utilizing the piezoresistive nature of the CNT filled polymers as SHM sensors. Some other works have been done using analytical models and numerical simulations in damage detection protocols for robust characterization of sensors [43 - 50]. For example, Zhu and Chung [43] developed an analytical model for piezoresistive carbon fiber polymer composite under flexural loads. The model was characterized by simultaneous increase and decrease in surface electrical resistances during flexure. The surface resistances were correlated to electrical conduction through the reinforcing fiber and conduction through the fiber-fiber contact for the longitudinal and through-thickness conductions, respectively. Similarly, Kuronuma *et al.* [44] used an analytical model to describe the piezoresistive response of carbon nanotubes by

considering the tunneling effect. Their model predicted the extent to which the contact configurations of the nanotubes affected electrical resistance response and strain sensitivities. The authors claimed that the model was highly useful in designing a carbon nano tube-based polymer with high strain sensing capabilities. In their investigation on strain transfer for surface attached optical fiber strain sensors, Wan *et al.,* [45] employed a shear lag model to predict strain transfer characteristics in the fiber strain sensors.

Studies have also been done on analytical modelling of micromechanical systems [46 – 49]. Moradi and Sivoththaman [49] analyzed the transmission of strain fields in adhesively bonded MEMS strain sensors and quantified the influence of the system's material parameters on the overall strain transmission while Hindrichsen *et al.* [18] analytically compared the sensitivities of thick and thin piezoelectric films for MEMs applications.

Significant attention has also been paid to utilizing electromechanical properties of thermal-sprayed coatings for different functionalities such as measuring or assessing friction and wear conditions of tribological contact zones [51], in wearable electronics [15], and for damage detection [14, 37, 39, 52]. Regarding thermally sprayed coating, Gonzalez, *et al.* [39] also developed a descriptive model in their work on thermally deposited Al-12Si on fiber reinforced polymer composite substrate for the relationship between relative resistance change and strain of the coating layer while considering its effective mechanical and electrical properties (Eq. (1-1)) [39]:

$$\frac{\Delta R}{R_o} = e^{(1+2v+c+\beta c)\varepsilon_x} - 1 = e^{a\varepsilon_x} - 1, \tag{1-1}$$

where ΔR is the change in electrical resistance, R_o is the electrical resistance without mechanical load, and $a = 1 + 2v + c + \beta c$ is a constant.

Though the model was cleverly developed, it needed to be extended to a multi-layer coating-substrate system for the case of electrically conductive coating and substrate. Of equal importance is to extend the analytical model to situations where there is imperfect integration between the coating layer and the substrate since this imperfection will have significant effect on the load transfer mechanism within the system.

1.6 Summary

Damage is an unavoidable occurrence in in-service engineering components, its early and real time detection will greatly reduce the huge cost lost to failure of engineering and its catastrophic implications. Efforts are still ongoing regarding implementing damage detection protocols in structural health monitoring. Special attention was paid on strain-based approach to damage detection, which is one of the most common and efficient ways of monitoring the health of structural components. Here, a cross-property relationship; relationship between strain in the substrate and electrical resistance of the strain monitoring device is utilized. To mitigate some of the existing gaps of using strain-based sensors such as such as susceptibility to creep, hysteresis, relatively low shear bond and temperature limitations, a review on the potentials of using thermally sprayed as damage detection sensors was done. This set a new precedence for the traditional functions of coating which is primarily protecting the surface of components. Structurally integrated coating-substrate, which have been made through thermal spraying show promise as a strain-based damage detection sensor.

To further improve this capability of thermally sprayed coating, there should be enough flexibility in influencing their physical properties, specifically mechanical and electrical properties. To this consideration, there are quite a few research exhaustively dedicated to the flexibility in improving specific properties of thermally sprayed coating. Though the as-sprayed

physical properties of the coatings could be exemplary, it was found that the functionality of the coatings can further be greatly improved through both spray parameters and post-deposition processes.

Furthermore, modelling techniques, descriptive or predictive ones have also been employed for an exhaustive damage monitoring technique. Modelling tools are quite useful in proving insight into processes that are otherwise difficult to experiment or observe to draw up very useful conclusions regarding the state of the system. In this respect, piezoresistive responses of potential damage detection sensors such as carbon nanotubes filled polymers, micromechanical systems, and thermally sprayed coatings have been modelled to make their strain sensing functionality a more robust one.

Overall, this chapter set the precedence to further exploring the promising potential of thermally sprayed coating in damage detection protocols.

1.7 Objectives

The main objective of this doctoral research was to fabricate a functional piezoresistive NiCoCrAlTaY with TiO_2 coating using flame spray technique. Specifically, the research work is aimed at:

i) Designing a bi-layered coating system with NiCoCrAlTaY-TiO_2 layer as a functional top layer and Al_2O_3, as the insulating layer sandwiched between the substrate and the top layer.

ii) Determining the suitable combination of flame spray parameters and feedstock material properties to deposit the functional coating system on steel and carbon fiber reinforced polymer substrates.

ii) Characterizing the microstructure and mechanical properties of the coating.

iii) Assessing the piezoresistive performance and ability of each coating layer to exhibit electrical responses to changes in the mechanical properties that correlate to in-service health of the base structure.

iv) Developing mathematical models based on piezoresistive constitutive relation to study the material and geometrical effects on the piezoresistive response of the bi-layered coating system.

1.8 Organization of the Thesis Document

The present thesis document has several chapters with the following structure: Chapter 1 summarizes the background and literature review for piezoresistive damage detection approach. In Chapter 2 of this thesis document, a comprehensive study of bi-layered piezoresistive coating-substrate systems was done. The discussion about the impact of reinforcing titania on the microstructure of the fabricated coatings and their electrical performance has been included in this chapter. Furthermore, the performance of the developed coating systems, as strain sensing coating, was discussed in detail. Chapter 3 presents the details related to the development of the analytical models focused on predicting the piezoresistive response of coating-substrate system. This is to further establish strain transfer mechanism within the system. Cases for both perfectly integrated coating-substrate system and a non-integrated one, in the form of delamination, are presented. In Chapter 4, the model developed in Chapter 3 was further modified to include bending effects in the coating layers. Chapter 5 summarizes the conclusions from this thesis. Finally, Chapter 6 provides the suggestions for future work for extension and modification of this research work.

Chapter 2

Fabrication and Electromechanical Test of Bi-Layered Coating-Based Piezoresistive System

To fabricate a good piezoresistive sensor through flame spray technique, the target properties were influenced right from the selection of the feed stock. For instance, a material or combination of materials (NiCoCrAlTaY-TiO_2) that potentially have excellent electrical conductivity while also having good piezoresistive response were methodologically chosen. Since the flame spray technique uses a combustion process to melt the feedstock powder, the potential chemical reactions that could improve these target properties through combustion process for the selected material(s) were well understood before the deposition of the sensor.

Aside this crucial electrical property, the sensor also needs to have good toughness and ductility to absorb enough stress without fracture and plastic deformation, respectively. In this regard, there was methodological selection of the spray parameters. In this work, the evaluation of the sensor's strain measurement ability was done on steel and carbon fiber reinforced polymer (CFRP) because they are commonly used in the renewable, and oil and gas industries. Since the substrates are electrically conductive, there was a need for an electrically insulating layer to prevent short-circuiting of the system. Thus, the insulating layer was methodologically chosen and fabricated to have similar mechanical properties to the component and the piezoresistive layer in order to minimize property mismatch within the system.

To ascertain that these target properties were achieved, characterization of the fabricated coating system, namely: NiCoCrAlTaY/TiO_2 – piezoresistive layer, Al_2O_3 – insulating layer, and

steel/CFRP - substrates was done for both before and after deposition on the substrates. The characterization was done through scanning electron microscopy (SEM), X-ray diffraction (XRD), temperature coefficient of resistance (TCR) measurements, indentation tests and electromechanical measurements.

The SEM was done to observe features such as thickness, homogeneity, coating continuity, adhesion, and porosity of the coating system while the XRD was done to study the chemical composition and degree of crystallinity in the coating layer since the types of chemical species present influence its strain sensitivity. A posteriori correlation of some of these observed features was done with the electromechanical properties of the coating layers.

It was desired that the sensitivity of the piezoresistive layer to temperature changes is as low as possible because it is undesirable for temperature changes to contribute to strain changes in piezoresistive applications. Hence, the need for the TCR tests. Also, its sensitivity to electrical resistance and strain changes should be high enough to correctly measure defects. Also, there should be a correspondence between the electrical resistance and strain changes to establish a correlation between them for sensor design purposes. Thus, the need for in-situ voltage and strain measurements of the coating system.

The results confirmed that the nickel alloy has enough strain sensitivity, which are up to 2 orders of magnitude more than an average metallic strain sensor. Also, it has low enough temperature coefficient of resistance. The elastic property mismatch between the coatings and the substrate from the nanoindentation test was also discussed and through the cyclic tests, the mechanical durability of the coating system was established.

Overall, the results obtained for the coating layers indicated their potential utilization in the industry on mass scale as strain sensors. On a final note, the NiCoCrAlTaY-TiO_2 coating was

fabricated on the flat steel samples while only the NiCoCrAlTaY was fabricated on carbon fiber polymer reinforced polymer (CFRP) and cylindrical steel samples.

Sections 2.1.2, 2.1.3, 2.1.6, 2.1.7, 2.1.8, 2.2.1, and 2.2.4 regarding NiCoCrAlTaY coated on flat steel substrate have been published in:

A. Ogunbadejo, S. Chandra, A. McDonald, "Flame-sprayed NiCoCrAlTaY coatings as damage detection sensors", in: *International Thermal Spray Conference*, May 4–6, 2022 (Vienna, Austria), DVS-The German Welding Society, (2022), 6 pages on compact disk.

2.1 Experimental Method

The details surrounding the coating from its fabrication to its testing on the two substrates; steel and carbon fiber reinforced polymer (CFRP) were discussed in the following sections.

2.1.1 Feedstock Powder

The morphology of the feedstock for the insulating layer, alumina (Al_2O_3, Amdry 6060, Oerlikon Metco, Westbury, NY, USA) is angular due to its manufacturing technique (fused and crushed) and its size distribution was 5 to 45 μm (-45+5 μm). Mechanical blend of nickel alloy (NiCoCrAlTaY, Amdry 997, Oerlikon Metco, Fort Saskatchewan, AB, Canada) and titania (TiO_2, Metco 102 Oerlikon Metco, Fort Saskatchewan, AB, Canada) powders was used as the piezoresistive layer. Their respective morphologies are spheroidal and angular while their respective size distributions are 5 to 38 μm (-38+5 μm) and 11 to 45 μm (-45+11 μm). The nickel alloy powder was manufactured through gas atomization and the titania was fused and crushed. The backscattered electron modes of the micrographs showing the powder morphologies of the conductive layers are shown in Fig. 2.1.

The fabrication of both the insulating and conductive layers was done through flame spray (FS) process.

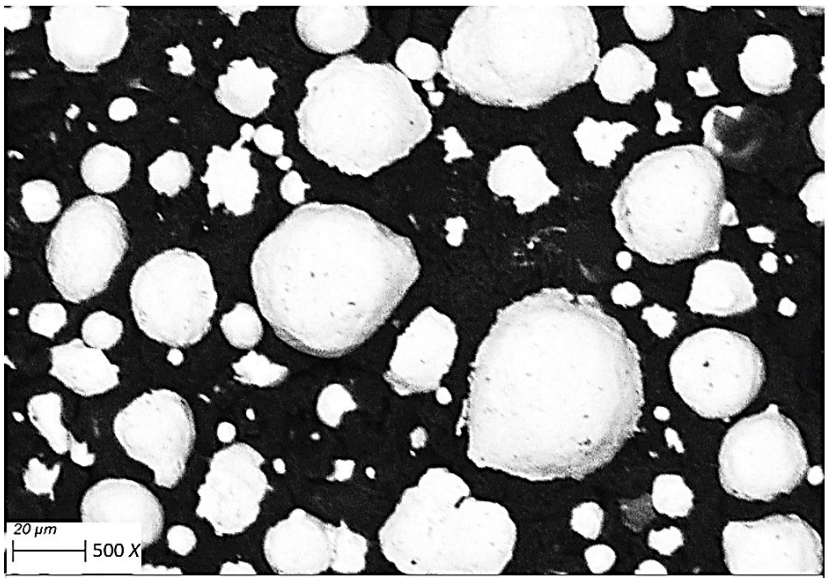

(a)

(b)

Figure 2-1 Back-scattered scanning electron microscope images taken at 500X magnification from (a) NiCoCrAlTaY powder, and (b) TiO_2 powder

2.1.2 Substrate preparation

For the flat steel samples, two sets of dimensions were used for the study; a 120-mm (4.72-in) long and 20-mm (0.79-in) wide 'dog bone' samples with a 50 mm × 10 mm (1.97 in x 0.39 in) gauge (Fig. 2-2 (a)) and 25 x 25 mm (1 in x 1 in) samples were fabricated. Both dimensions were fabricated from a 6-mm (0.24-in) thick A36 steel plate (A36/44w mild steel hot rolled flat bar, Metal Supermarkets, Edmonton, AB, Canada) through water jet cutting. The former was for electromechanical tests and the later for SEM and XRD characterization. Both samples were mounted for each deposition simultaneously to ensure identical coating structure. Similar preparations were done for the flat CFRP (chemical-resistant PAEK and carbon fiber sheet, McMaster Carr, Elmhurst, IL, USA) samples. The dimension for electromechanical test CFRP sample is 230 mm x 20 mm x 2 mm (9.06 in x 0.79 in x 0.088 in) and 25 mm x 25 mm x 2 mm (1 in x 1 in x 0.088 in) for coating characterization as shown in Fig. 2-2 (b).

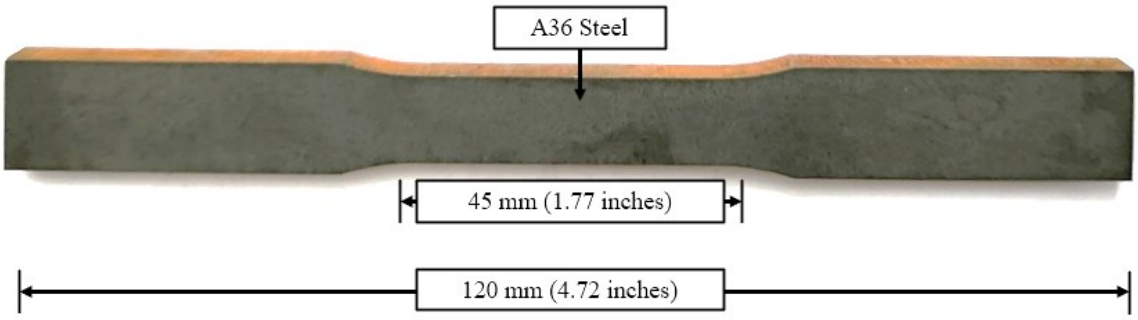

(a)

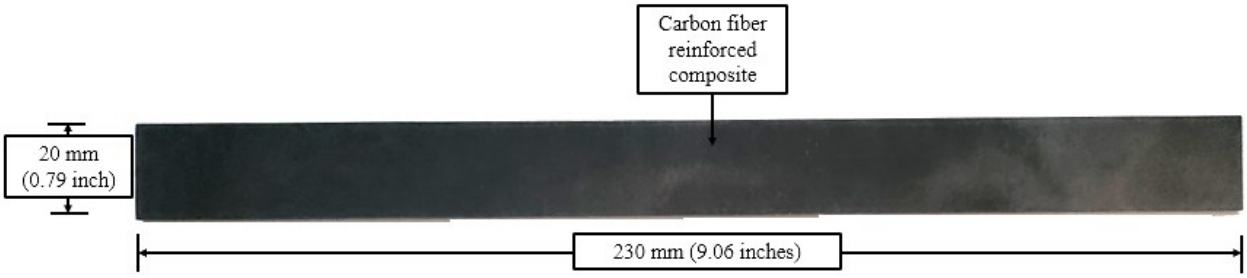

(b)

Figure 2-2 (a) Steel sample and, (b) carbon fiber reinforced polymer (CFRP) sample for the electromechanical tests

For the cylindrical steel sample, a 254-mm (10-in) long, 51-mm (2-in) diameter carbon steel pipe was used in this work. The carbon steel pipe was Schedule 40 pipe of ASTM carbon steel pipe (ASTM A333-6) which is widely used various industries. To facilitate the simulation of an internal pressurization of the pipe, a pipe assembly was made by butt-welding two A420 WPL6 end caps, each including a 19-mm (0.75-in) Class 3000 A350 LF2 threadolet to the ends of the pipe (Fig. 2-3). After the welding-processes, the total length of the assembly that consisted of the pipe, the two end caps, and the two threadolets was 381 mm (15 in). The pipe assembly is shown

in Fig. 2-4. All the parts of the pipe making up the pipe assembly were rated 103.42 MPa (15000 psi)

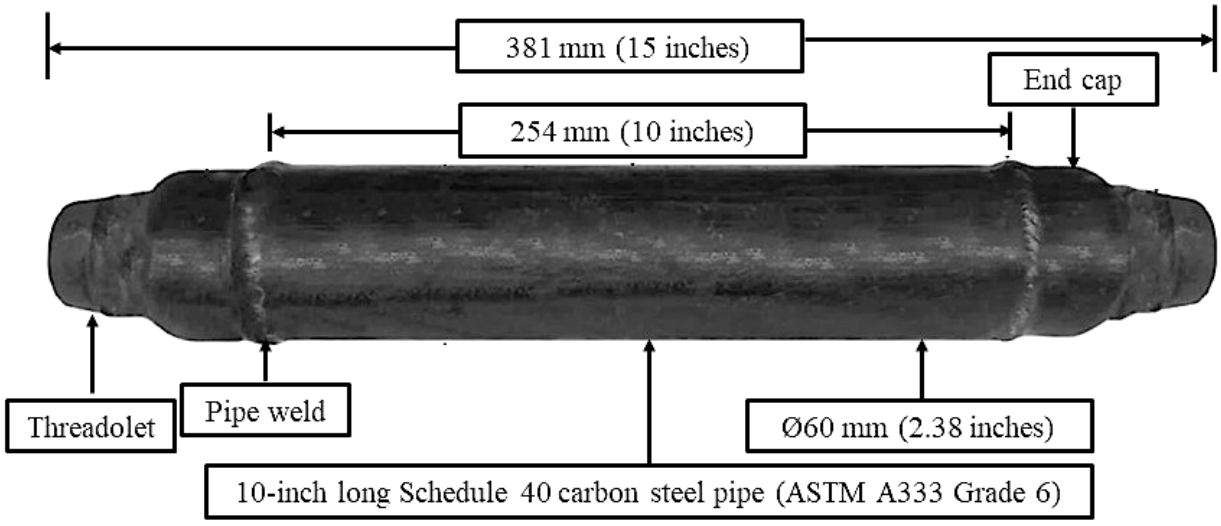

Figure 2-3 The pipe used as a substrate after welding the end caps.

All the steel samples were grit-blasted with #24 alumina grit size at an air pressure of 621 kPa (90 psig). To minimize the residual stress due to impingement of the grit particles, the grit-blasting was limited to 2 passes. This was enough to create the desired roughness required for high adhesive shear stress between the flame sprayed alumina and the steel substrate. For the dog-bone sample, only the gauge section was grit-blasted while the entire surface was roughened for the 25 mm x 25 mm (1 in x 1 in) samples. For the cylinder sample (Fig. 2-4), only the mid-section was grit-blasted. To avoid deposition of the coating layers on the parts not required to be sprayed, a masking tape (170-10S Red, Green Belting Industries, Mississauga, ON, Canada) was used to cover these parts during the grit blasting and thermal spraying stages.

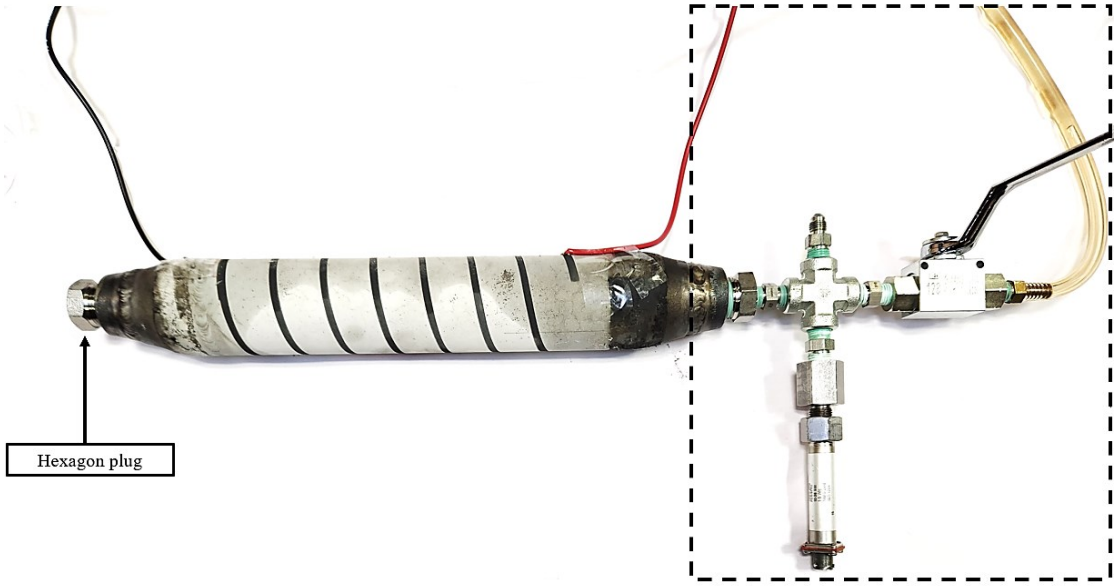

(a)

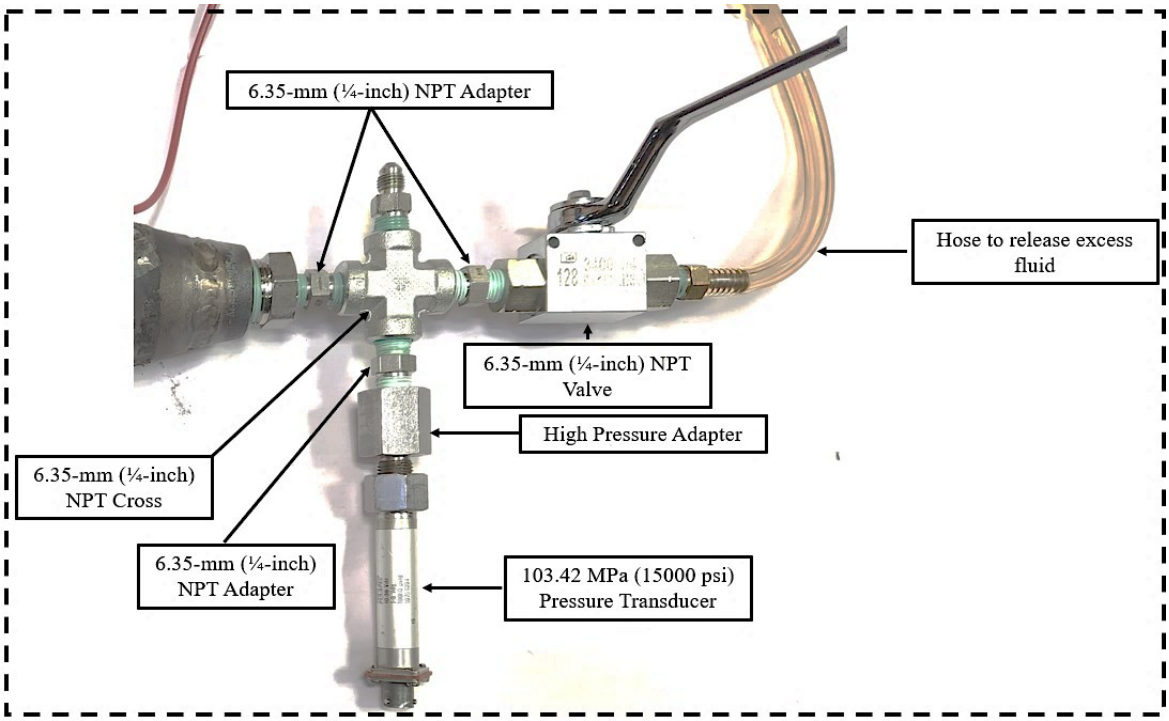

(b)

Figure 2-4 (a) A pipe assembly installed with pressure transducer, adapters, and valves with (b) zoomed in part of the assembly to show a more detailed view

For the CFRP sample, same grit size of alumina was used to spray its gauge section but at an air pressure of 414 kPa (60 psig). A comparatively lower air pressure was used to minimize the exposure of the carbon fibers in the CFRP samples. Pictures of the substrates for both before and after grit-blasting are shown in Fig. 2-5.

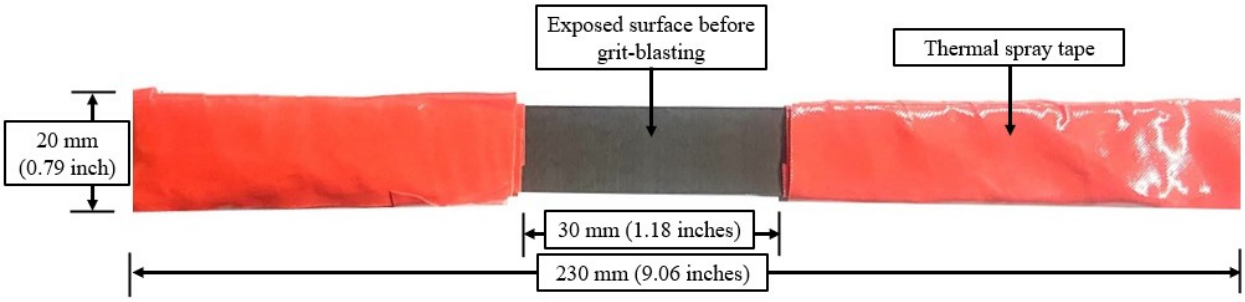

(a)

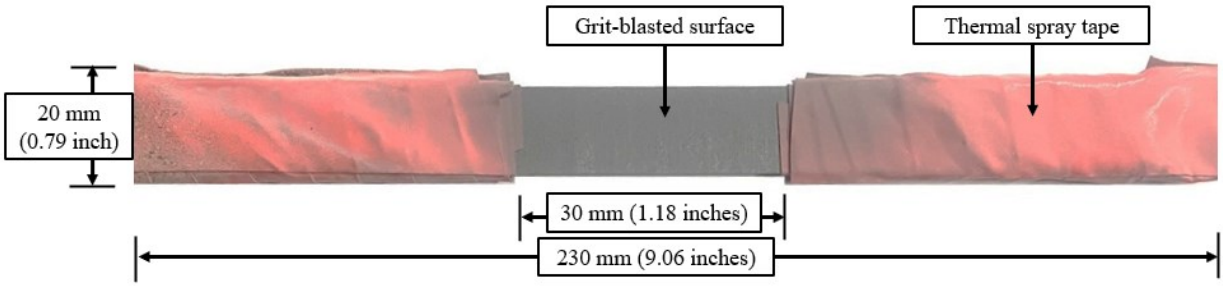

(b)

Figure 2-5 The carbon fiber reinforced polymer (a) before grit-blasting and, (b) after grit-blasting

2.1.3 Deposition of Coating Layers

Fabrication of coating system for flat steel samples

Just before the deposition of the insulating layer, the steel samples were pre-heated by passing the lighted flame spray torch twice over the surface of the samples to minimize the residual stresses that would be generated during the cooling and solidification of the alumina particles. The

same oxy-acetylene fuel ratio used for the pre-heating process was also used for the deposition process.

To deposit the coating layers, the feedstocks were continuously fed to an oxy-acetylene flame spray torch (6P-II, Oerlikon Metco, Westbury, NY, USA) through a volumetric powder feeder (5MPE, Sulzer Metco, Westbury, NY, USA). The torch was installed on a programmable robot (HP-20, Motoman, Yaskawa Electric Corp., Waukegan, IL, USA) to ensure a consistent and repeatable deposition The flow rate meter (FMR), which is a relative rate at which powder is being delivered to the torch, was used in this study to be indicative of different flow rates for different powders because of the variations on material densities. Argon is the primary carrier gas for the powder while the secondary gas, hydrogen was used to contribute to the flame heat content and acceleration of the powders [53, 54]. The steel sample, after the deposition of the insulating and the conductive layers is shown in Fig. 2-6.

Fabrication of coating system for carbon fiber reinforced polymer samples

For the carbon fiber reinforced polymer (CFRP) samples, it was found that exposing the whole area of the gauge section resulted in no deposition of the alumina with significant degradation of the CFRP. Therefore, a large percentage of the gauge section area was protected from the flame of the torch with the help of an overlay masking before depositing the insulating layer (Fig. 2-7). Thus, a grid pattern of the alumina was first sprayed on the CFRP before depositing NiCoCrAlTaY over the alumina with the overlay masking still over the surface of the CRFP. A 40-second pause between each pass was done to prevent the CFRP from thermal degradation. A silver-filled conductive polymer (EP21TDCS, Master Bond, Hackensack, NJ, USA) was deposited at the terminals of the deposited nickel alloy grid for proper electrical

connection between the conductive layer and the power supply. The CFRP after the deposition of the insulating layer and the conductive layer are shown in Figs. 2-8 (a) and (b). The systematically chosen spray parameters used for the deposition of both the insulating and conductive layers are listed in Table 2.1.

The grid pattern of the NiCoCrAlTaY was to increase its effective length of the conductive layer and thus its electrical resistance. It should be noted that the conductive layer strip thickness was chosen to optimize between the electrical resistance of the nickel alloy layer and its required surface area for strain computation with digital image correlation technique.

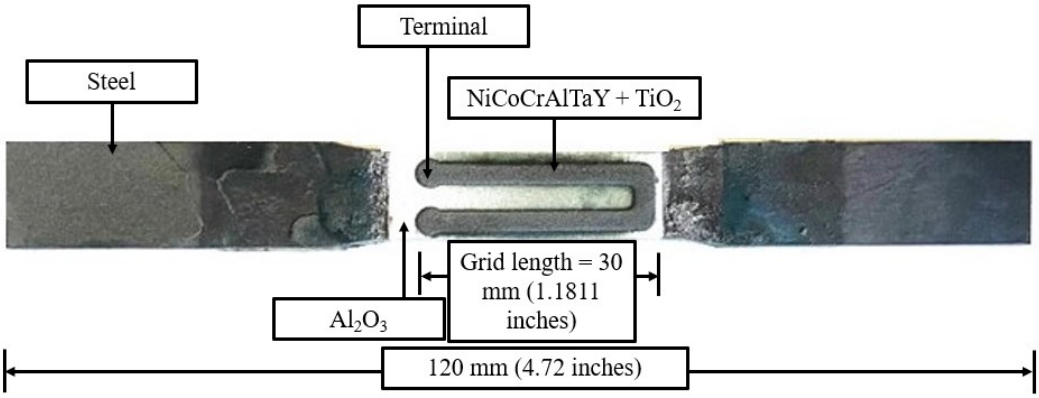

Figure 2-6 Steel sample after deposition of alumina and nickel alloy

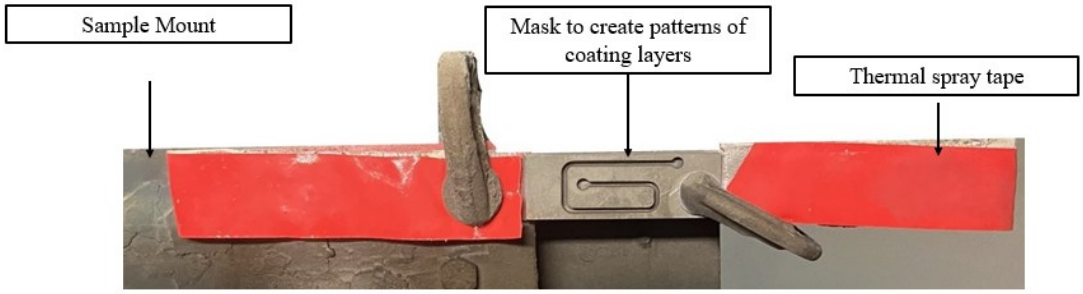

Figure 2-7 The CFRP mounted for alumina and nickel alloy deposition.

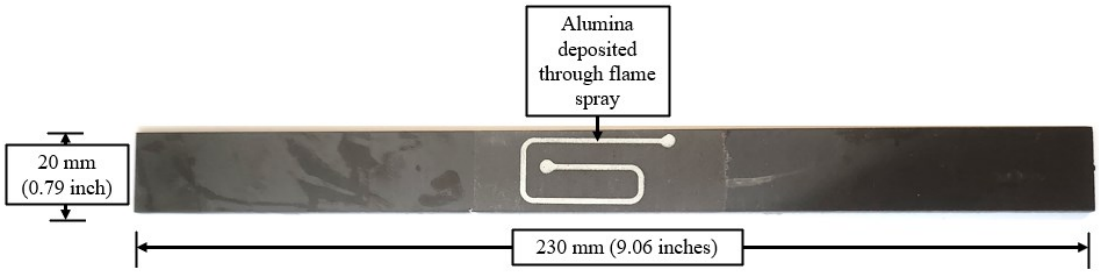

(a)

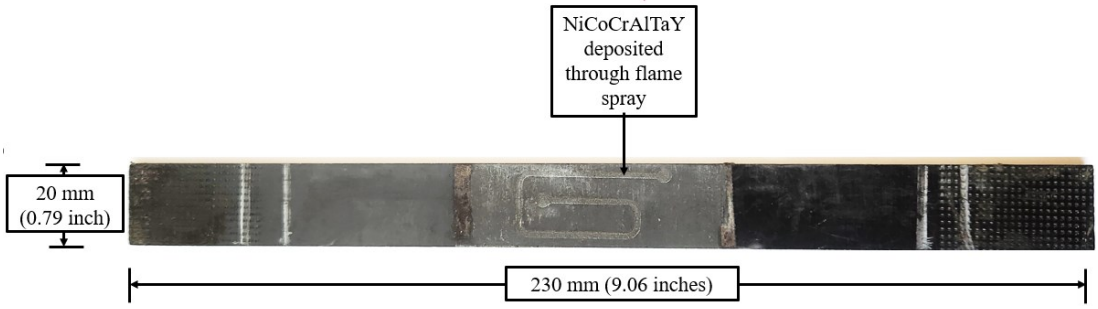

(b)

Figure 2-8 The CFRP (a) after deposition of alumina, and (b) after deposition of the nickel alloy over the alumina.

Fabrication of coating system for cylindrical samples

The pipe, held by a rotating chuck, was made to rotate at a particular speed while the torch was also set at a particular linear speed depending on the coating to be deposited (Table 2-1). Rotational speed of 600 rpm was used for the Al_2O_3 and NiCoCrAlTaY while the torch speed selected for both was 24 mm/s. The combination of the rotational and linear speeds was carefully selected to ensure uniform coatings around and along the pipe. Before depositing the conductive layer, the thermal tape was used to cover the ends of the pipe since just the middle section is required to be sprayed. To increase the electrical resistance of the conductive layer, a helical pattern of the layer was sprayed over the alumina layer by covering the pipe, after deposition of the alumina. These various stages of deposition are shown in Figs. 2-9 and 2-10.

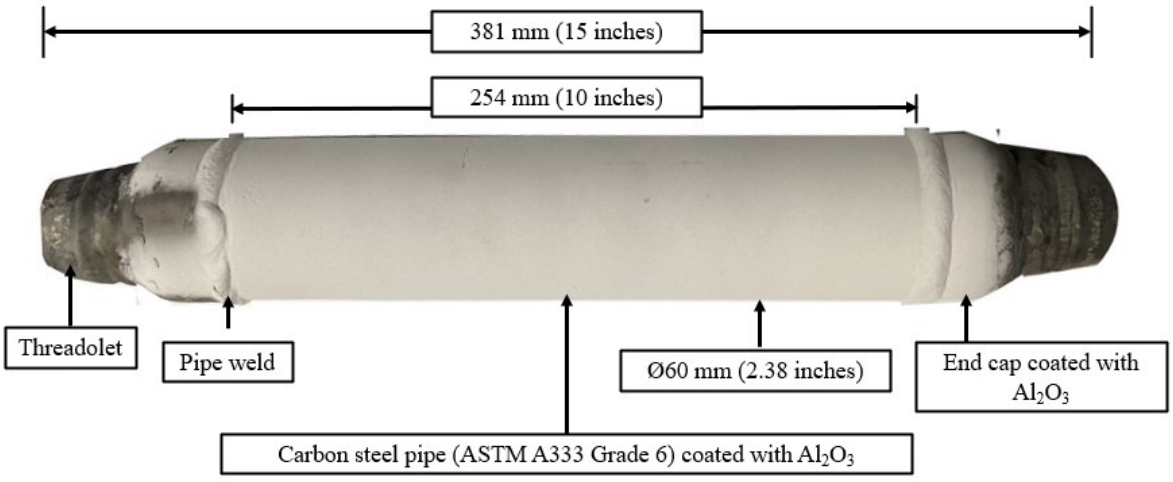

Figure 2-9 Schedule 40 carbon steel pipe (ASTM A333 Grade 6) after deposition of Al_2O_3

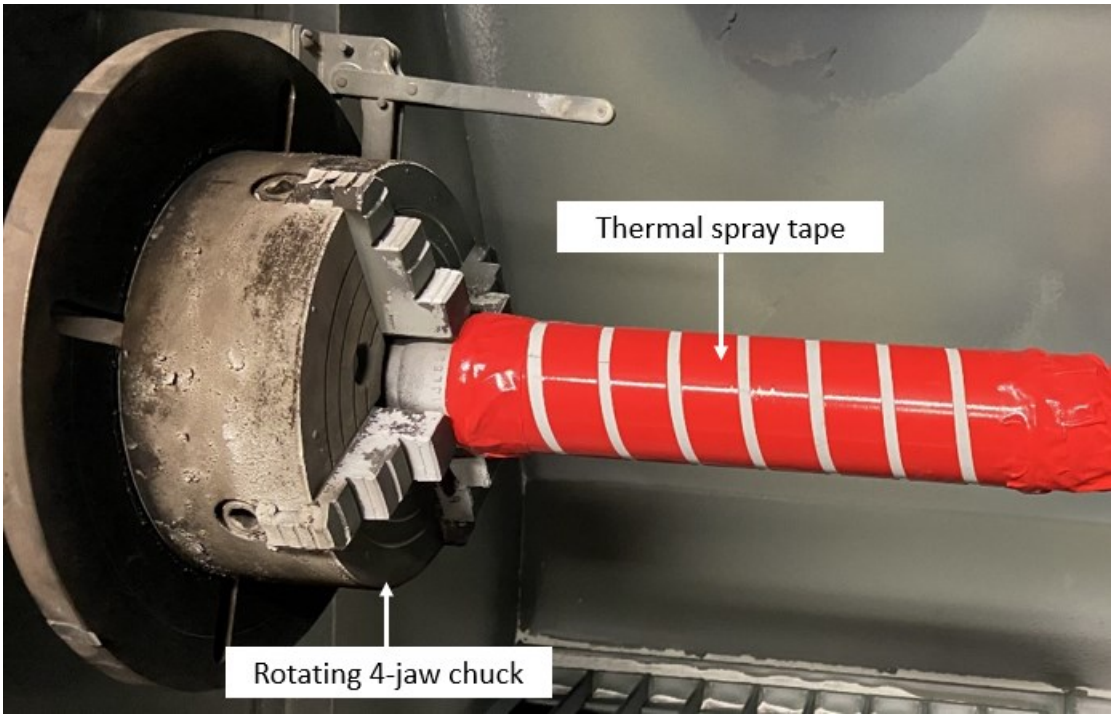

(a)

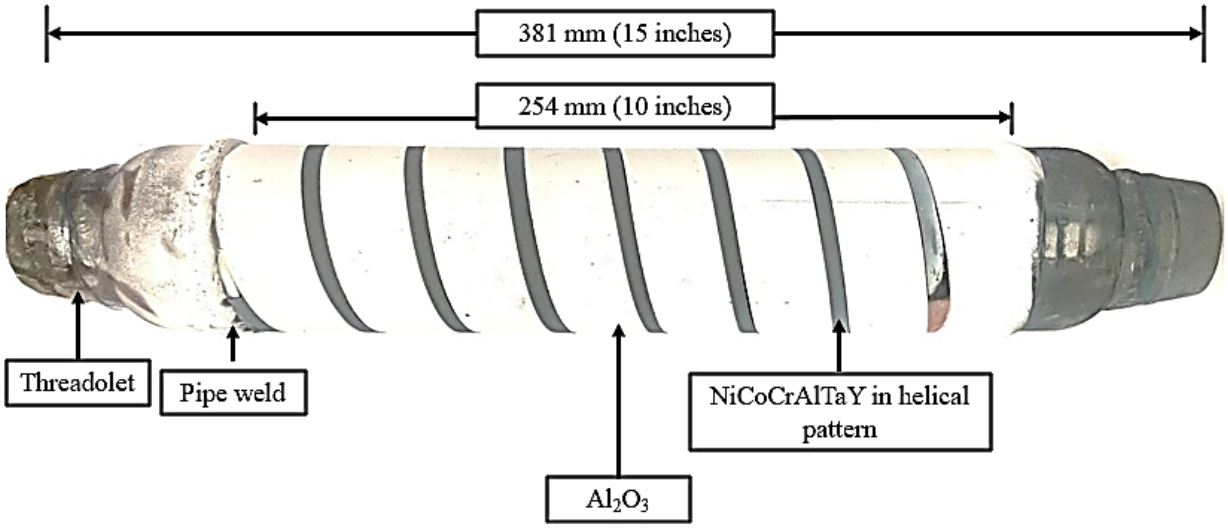

(b)

Figure 2-10 Schedule 40 carbon steel pipe (ASTM A333 Grade 6) (a) just before deposition of NiCoCrAlTaY, and (b) after deposition of helical pattern of NiCoCrAlTaY

Table 2-1 Spray parameters for the CRFP, flat steel and cylindrical steel samples

Coatings geometry / Spray parameter	Pipe		Flat steel				Flat CFRP	
	Al_2O_3	NiCoCrAlTaY	Al_2O_3	NiCoCrAlTaY	NiCoCrAlTaY-TiO_2 20 wt. %	NiCoCrAlTaY-TiO_2 40 wt. %	Al_2O_3	NiCoCrAlTaY
Stand-off distance [mm]	127	177.8	127	177.8	177.8	177.8	177.8	177.8
Transverse speed of torch [mm/s]	24	24	300	350	350	350	350	350
Acetylene flow rate [m^3/h]	1,32	1.20	1.32	1.20	1.20	1.20	1.32	1.20
Oxygen flow rate [m^3/h]	1.92	1.80	1.92	1.80	1.80	1.80	1.92	1.80
Argon flow rate [m^3/h]	0.56	0.56	0.56	0.56	0.56	0.56	0.56	0.56
Number of passes	1	1	3	3	3	3	2	2
Powder feed rate [FMR]	100	80	100	80	80	80	100	80
Increment [mm]	3	3	3	3	3	3	3	3
Wait time between passes [s]	-	-	-	-	-	-	40	40
Rotating speed of cylinder [rpm]	600	600	-	-	-	-	-	-

2.1.4 Temperature Coefficient of Resistance Measurement

In the context of piezoresistivity, an unfortunate characteristic of piezoresistors is that their electrical resistance changes with temperature. In this research, it was thought that the problem could be transcended by evaluating the temperature coefficient of resistance of the coating and then compensating for subsequent measurements. In this context, the temperature measurement employed in this work applied the linear approximation of the resistance versus temperature relationship between room temperature (which is the temperature the electromechanical tests would be carried out) and the maximum temperature reached at the maximum voltage [55].

A direct current (DC) power supply (1902B DC, B&K Precision Corporation, Yorba Linda, CA, USA) was employed to supply the required voltage to the conducting layer of the coating-substrate system. Initially, a digital multimeter (34461A Digital Multimeter, Keysight Technologies, Mississauga, ON, Canada) was used to measure the electrical resistance through four-point Kelvin connection technique. Subsequently, five K-type thermocouples (Twidec 3M K-Type Sensor Probe, Suzhou, Jiangsu, 215008, CN) were employed to record the surface temperature of the conductive layer. A voltage of 7 V and constant current of 5 A were supplied to the coating-substrate systems and a data acquisition system (SCXI-1600, National Instruments, Austin, TX, USA) was used to log the current, voltage and surface temperature changes at 2 Hz.

The electrical resistance, electrical resistivity and temperature coefficient of resistance were thereafter calculated according to Eqs. (2-1) to (2-3), respectively:

$$V = IR, \tag{2-1}$$

where V, I and R are the voltage supply, current supply, and bulk resistance of the conductive layer, respectively.

$$\rho = \frac{RA}{l}, \tag{2-2}$$

where ρ, R, A and l are the resistivity, bulk resistance, cross-sectional area, and effective length of the conductive layer, respectively. And

$$R = R_o\left[1+\alpha\left(T-T_0\right)\right], \tag{2-3}$$

where R is the bulk resistance at temperature, T. R_o is the reference bulk resistance at reference temperature, T_o. α is the temperature coefficient of resistance.

2.1.5 Nanoindentation Test

To evaluate the elastic modulus, hardness and consequently elastic property mismatch for the coating substrate system, nanoindentation was performed using a Bruker Hysitron TI Premiere Nano indenter. The indentations were performed at a load of 5,000 μN using a sharp three-faced pyramid Berkovich diamond tip indenter. The loading and unloading cycles were separated by 30 s. At least 20 indents, for a dwell time of 15 s, were taken for each coating to ensure consistency and the closest 10 were averaged for final determination of the mechanical properties. To relate these mechanical properties of the indentation load-displacement data, a classical approach [56] which focuses on the elastic modulus, E, and hardness, H was adopted. In this approach, the initial unloading contact stiffness is related to the elastic modulus of the coating layers while the hardness is related to the maximum load applied on the coating and the contact area. Figure 2-11 shows the typical loading and unloading curve for the indentation [57].

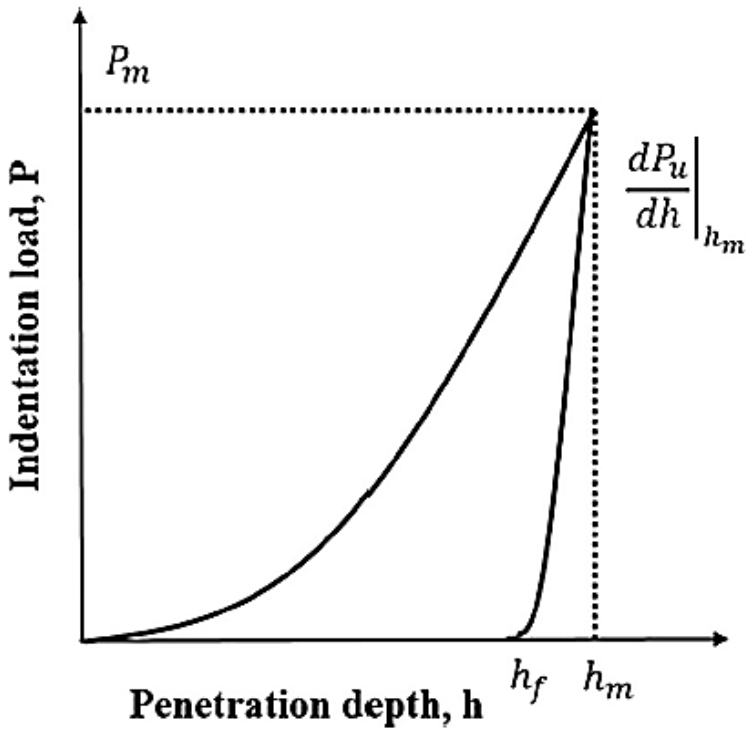

Figure 2-11 Schematic representation of load versus indenter displacement data for an indentation experiment [57].

The relationships described above are given as [57]:

$$S = \left(\frac{dP}{dh}\right)_{h_m} = 2E_r\sqrt{\frac{A}{\pi}}, \tag{2-4}$$

where S is the initial unloading contact stiffness, $\left(dP/dh\right)_{h_m}$ is the unloading slope at the maximum displacement h_m, A is the projected contact area at the maximum load and E_r is the reduced modulus given by:

$$\frac{1}{E_r} = \frac{1-\nu_i^2}{E_i} + \frac{1-\nu^2}{E}. \tag{2-5}$$

In Eq. (2-5), v, E, v_i, E_i are the Poisson's ratio and Young's modulus of the coating and the indenter, respectively. The hardness, H of the coating layers was then calculated from:

$$H = \frac{P_{\max}}{A}, \tag{2-6}$$

$P_{\max}$ is the maximum load applied.

2.1.6 Electromechanical Tests

Electromechanical test on steel samples

For the flat steel samples, the coating-substrate system was subjected to two types of mechanical loading: quasi-static cyclic and quasi-static uniaxial tensile loadings. For the cyclic loading, the system was subjected to 1000 extension and compression loading cycles in a servo hydraulic testing system (MTS 810 Systems Corporation, Minneapolis, MN, USA) between 0 and 0.4 mm at a stroke rate of 0.5 mm/min. To significantly collapse the pores in the flame sprayed nickel alloy thereby getting a more consistent electrical resistance changes, a 40 extension and compression cycles between 0 and 0.2 mm was initially done at the same stroke rate on the coating-substrate system before the 1000 loading cycles. For the uniaxial tensile test, the same stroke rate was also used till failure of the system.

In the case of CFRP samples, a uniaxial tensile test at a stroke rate of 1 mm/min was done till the failure of the coating-substrate system. This was done with the same servo hydraulic testing system employed for the steel substrate.

For the cylindrical steel samples, cyclic internal pressurization of the pipe was done at the rate of 41.4 MPa/min (6000 psi/min) for 100 cycles. The cylinder was subjected to a minimum

internal pressure of 0 MPa (0 psi) and maximum internal pressures of 31 MPa (4500 psi), 41.4 MPa (6000 psi) and 55.2 MPa (8000 psi) for each 100 cycles. The pressurization was done through a hydraulic pressure intensifier. A pressure transducer (Omega Sensing Solutions, St-Eustache, QC, Canada) installed at one of the ends of the pipe was employed to directly monitor the internal pressure of the pipe to ensure it matches the pressure from the pressure intensifier.

Because the radius of the cylinder is less than 20 times the wall thickness, it is categorized in this work as a thick-walled cylinder [58, 59]. In a thick-walled cylinder, it is not accurate to assume that the radial and hoop stress distributions are uniform along the thickness of the cylinder. However, the axial stress can be assumed to be uniform provided there are no thermal stresses [58, 60, 61]. Thus, equilibrium and compatibility equations could be employed to analyze the states of stresses and strains along the radius of the cylinder.

For each instance of substrate electromechanical testing, *in situ* electrical measurement was carried out during the quasi-static mechanical loadings and internal pressurization to measure the real time electrical voltage changes. The real-time voltage changes were measured and logged with a multifunction DAQ device (USB-6800 NI Company, Austin, TX, USA). A DC power supply (1902B DC, B&K Precision Corporation, Yorba Linda, CA, USA) was used as the supply voltage source. The schematic of the electrical set-up is shown in Fig. 2-12. In the bridge configuration used, R_1 and R_3 are precision resistors while R_2 and R_x are resistances of the potentiometer used to balance the bridge (before the application of mechanical loads) and flame sprayed coating, respectively. Before the tests, R_2 is adjusted to balance the bridge voltage, V_g to zero. V_s is the supply voltage and V_x is the instantaneous voltage across R_x. All data were logged at 4 Hz.

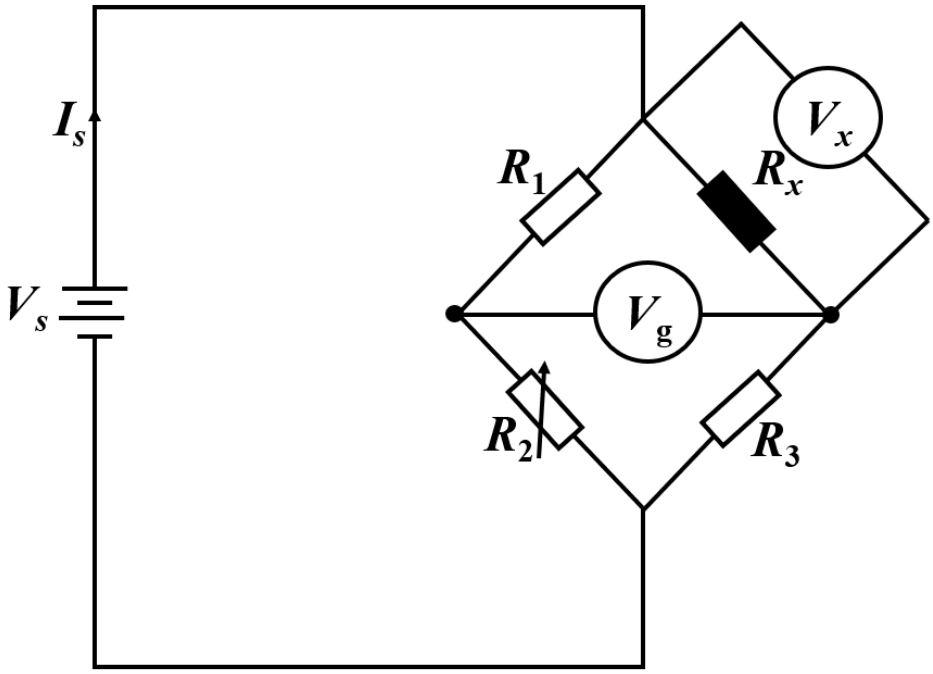

Figure 2-12 Schematic of the electrical set-up for the electromechanical test.

2.1.7 Digital Image Correlation

For the flat samples (steel and CFRP), Promon U750 High Speed camera (AOS Technologies AG, Taefernstrasse 20 CH-5405 Baden-Daettwil, Switzerland) was used to record time stamped images, at 4 Hz frame rate in real time. The images are taken just before the specimen was subjected to the loading (reference image) and then during deformation (deformed image). The set-up is shown in Fig. 2-13 (a).

The recorded images were analyzed through a digital image correlation (DIC) software (Vic-2D v6 software, Correlated Solutions, Inc., Irmo, South Carolina, USA) for strain computation. For the cylindrical sample, two high speed cameras (Hadland Imaging, Santa Cruz, CA, USA) positioned at symmetric angles were used to record the time stamped images at 4 Hz frame rate in real time.

Before images were taken, calibration of the cylinder was done simultaneously in both cameras, and the synchronized target images are used to fully calibrate the system in one step. Thereafter, images are taken just before the specimen was subjected to the loading (reference image) and then during deformation. The recorded images were analyzed through a digital image correlation (DIC) software (Vic-3D 9 software, Correlated Solutions, Inc., Irmo, South Carolina, USA) for strain computation. The set-up for the strain measurement of the cylinder and a sample of the images from both cameras' views of the cylinder before deformation are shown in Fig. 2-14 (a) and (b).

Unlike the conventional extensometer, the DIC technique is a non-invasive technique as the camera does not have direct contact with the surface of the sample. The software tracks the unique surface patterns and creates a mesh of the surface by applying stereo-triangulation. The displacement and surface strains are then calculated by comparing the recently created surface mesh to the initial surface mesh. To create distinct patterns on the surface of the specimen, a speckle pattern is sometimes applied to the surface to create a well-contrasted image. However, speckle pattern was not applied to the coating on the steel substrates as the coating produced contrasted images (Figs. 2-13 (b) and 2-14 (b)) with shiny spots that could be easily tracked for strain computation. But the application of speckle pattern was needed for the CFRP substrate (Fig. 2-15) because of the poor contrast. Before strain computation, an area of interest (AOI) was selected on the image representing the undeformed specimen. The AOI is further divided into subsets. The grids formed by the subsets are then digitally tracked by the Vic 2D v6 (for flat samples) and Vic 3D 9 (for cylindrical sample) software in the time stamped images of the loaded specimen.

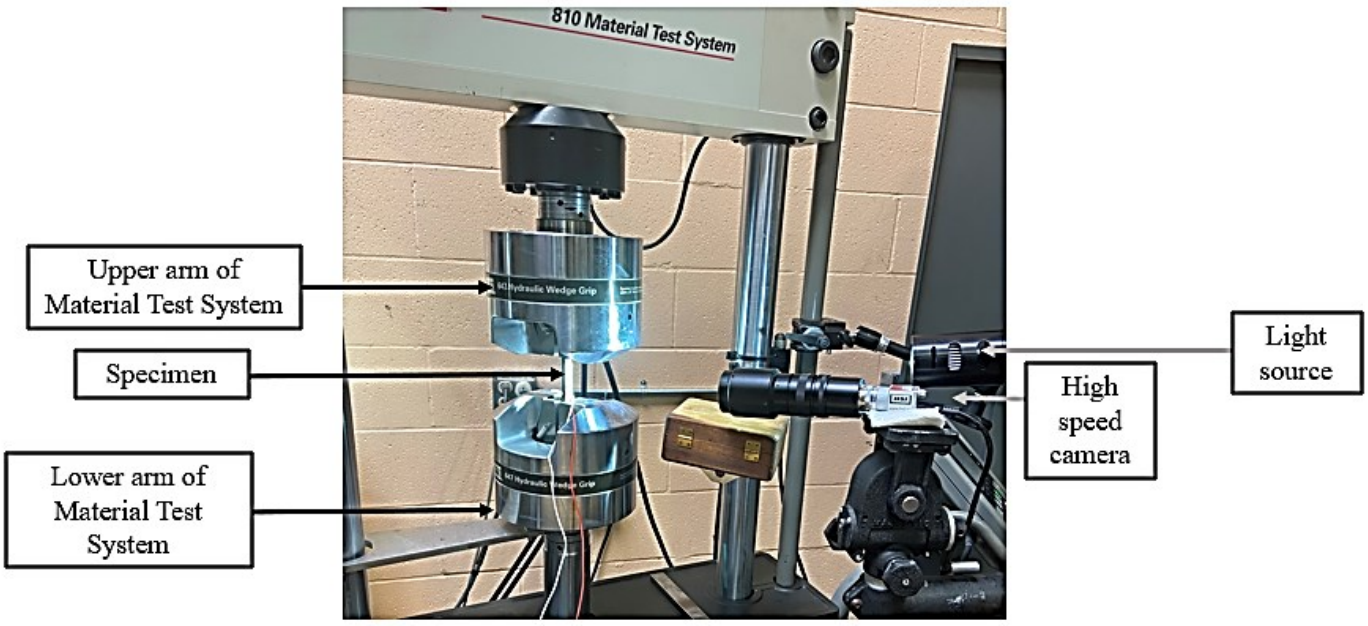

(a)

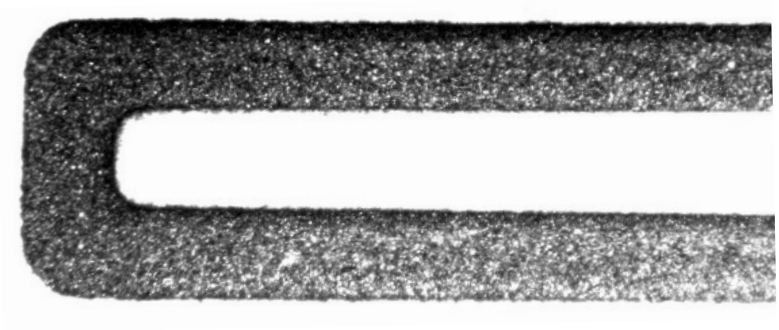

(b)

Figure 2-13 Strain measurement set up for the (a) flat samples and (b) a sample image of the steel substrate from fast imaging camera before deformation.

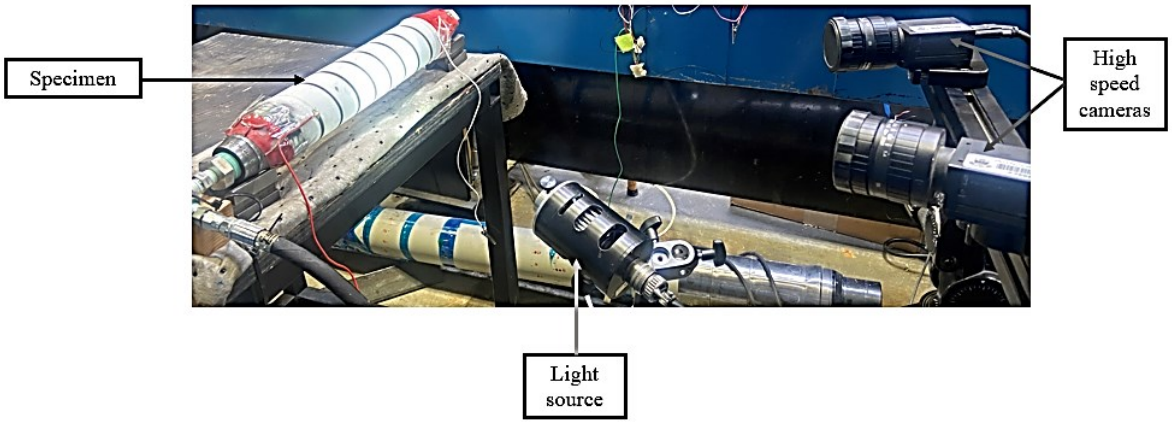

(a)

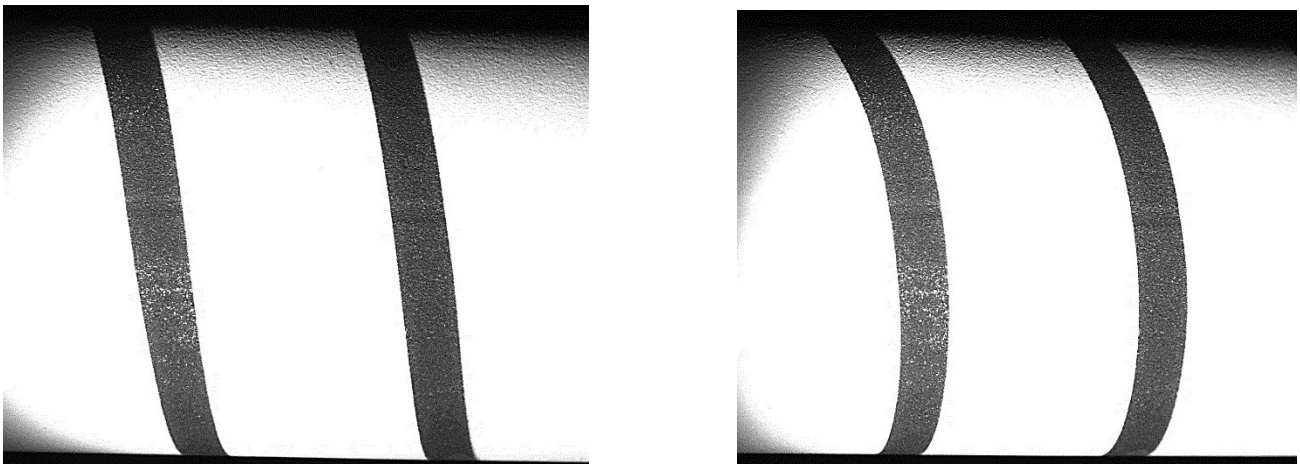

(b)

Figure 2-14 (a) Strain measurement set up for the steel cylinder, and (b) sample images of the steel cylinder from the views of the fast-imaging cameras before deformation.

Figure 2-15 Image from fast imaging cameras used to measure 2D strain for carbon fiber reinforced polymer (CFRP)

2.1.8 Sample Preparation for SEM and XRD

The cross sections of the gauge sections for the mechanically loaded and unloaded flat coating-substrate systems were observed through a scanning electron micrograph (SEM) equipped with backscattered electron detector (Zeiss Sigma 300 VP-FESEM, Carl Zeiss Canada Ltd., Toronto, ON, Canada). Since the gauge section could not fit into the mount in the SEM for the flat sample, it was carefully sectioned into three parts. The parts were cold mounted in an epoxy resin (LECO, Mississauga, ON, Canada) and then metallographically prepared for the SEM examination. The surface preparation was done by grounding the cross sections with 180, 240, 320, 400, 600, 800 and 1200 silicon carbide grit papers (LECO, Mississauga, ON, Canada), respectively and then polishing the surfaces using 3 μm and 1 μm diamond pastes (LECO, Mississauga, ON, Canada), respectively. To prevent anomalous contrast in the backscattered SEM

images due to charging effect of the non-conductive Al_2O_3 layer, a thin film of carbon was deposited on the coatings by using a carbon evaporation device (EM SCD 005, Leica Baltec Instrument, Balzers, Liechtenstein). For the flat steel substrate subjected to cyclic loading, the metallographic preparation was done on the coating-substrate system at specific mechanical loading cycles: 300 and 1000 cycles to monitor the interfaces and crack propagation within the coatings. Also, the sample subjected to destructive uniaxial tensile loading was examined with SEM. ImageJ (Rasband, W.S., ImageJ, U. S. National Institutes of Health, Bethesda, MD, USA) coupled with MATLAB was employed to determine the average thickness, percentage composition and porosity of each coating layer.

The X-ray diffraction (XRD) of the coated sample was conducted to examine the phase evolution accompanying the coating deposition. XRD utilizes monochromatic X-rays generated by a cathode ray tube, which are filtered and collimated before being directed towards a crystalline sample. The interaction between the incident X-rays and the sample produces diffracted rays through constructive interference, following Bragg's Law [62]:

$$n\lambda = 2d \sin \theta, \tag{2-7}$$

where n is the diffraction order, λ is the wavelength of the incident rays. d is the distance between atomic planes, θ is angle of the incident rays.

These diffracted X-rays are then detected, processed, and counted. By scanning the sample through a range of 2θ angles, XRD captures diffraction patterns from various lattice planes, enabling the determination of the crystalline material's lattice structure and orientation [60, 61].

2.2 Results and Discussion

2.2.1 Coating characterization

Scanning electron microscopy on coated steel substrate

The microstructural properties and defects of a coating layer influence its physical properties [63 - 70]. With respect to this, features such as delamination, cracks, pores, and inclusions can affect the electrical and mechanical properties of the NiCoCrAlTaY. Flame spray technique is known to produce relatively porous coatings compared to other thermal spray deposition techniques [71 - 73]. This porous nature of the deposited coating by flame spray process can be seen in Fig. 2-16 to 2-18.

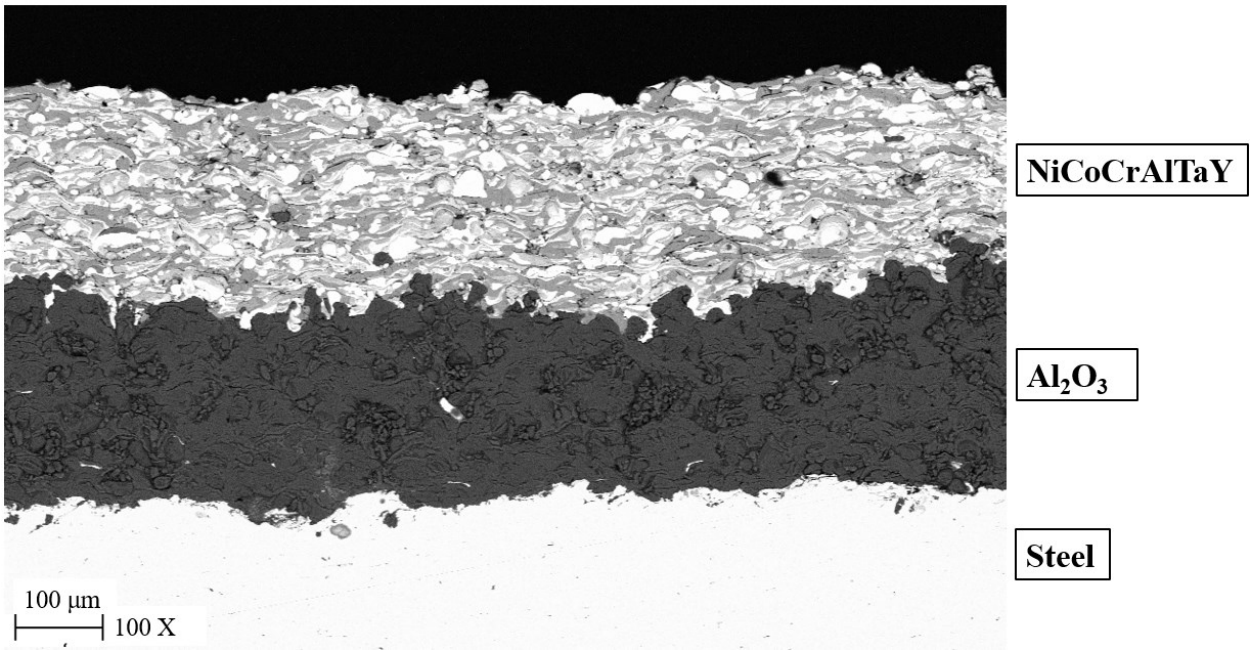

Figure 2-16 Back-scattered SEM image of the unloaded bi-layered coating-substrate system with NiCoCrAlTaY as the conductive layer

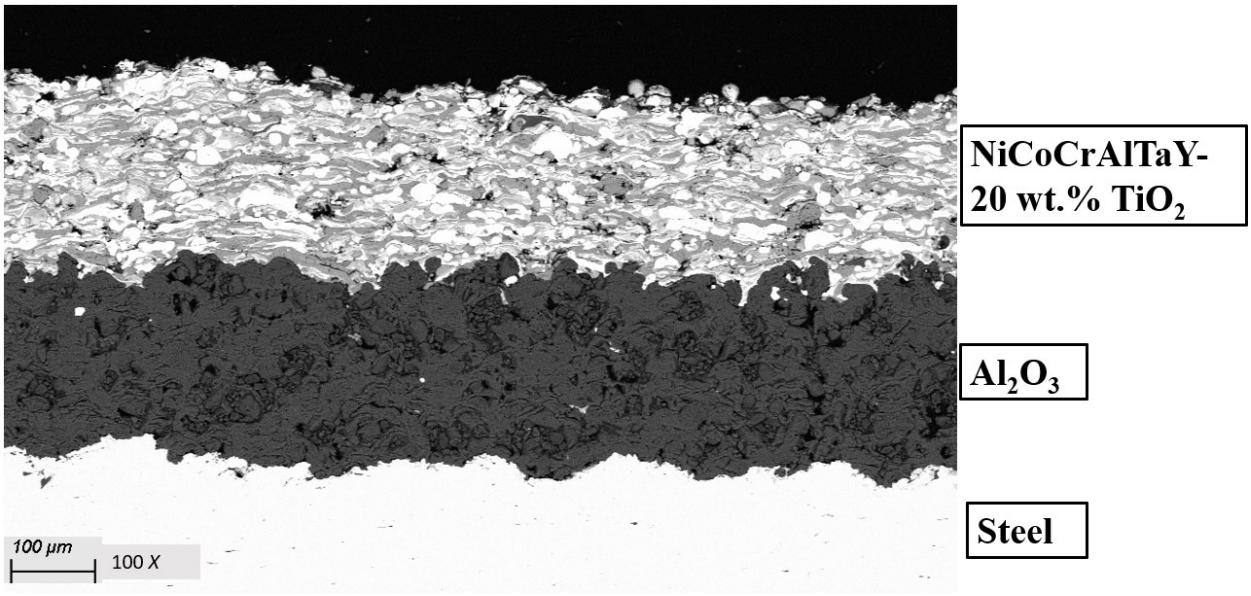

Figure 2-17 Back-scattered SEM image of the unloaded bi-layered coating-substrate system with NiCoCrAlTaY-20 wt.% TiO_2

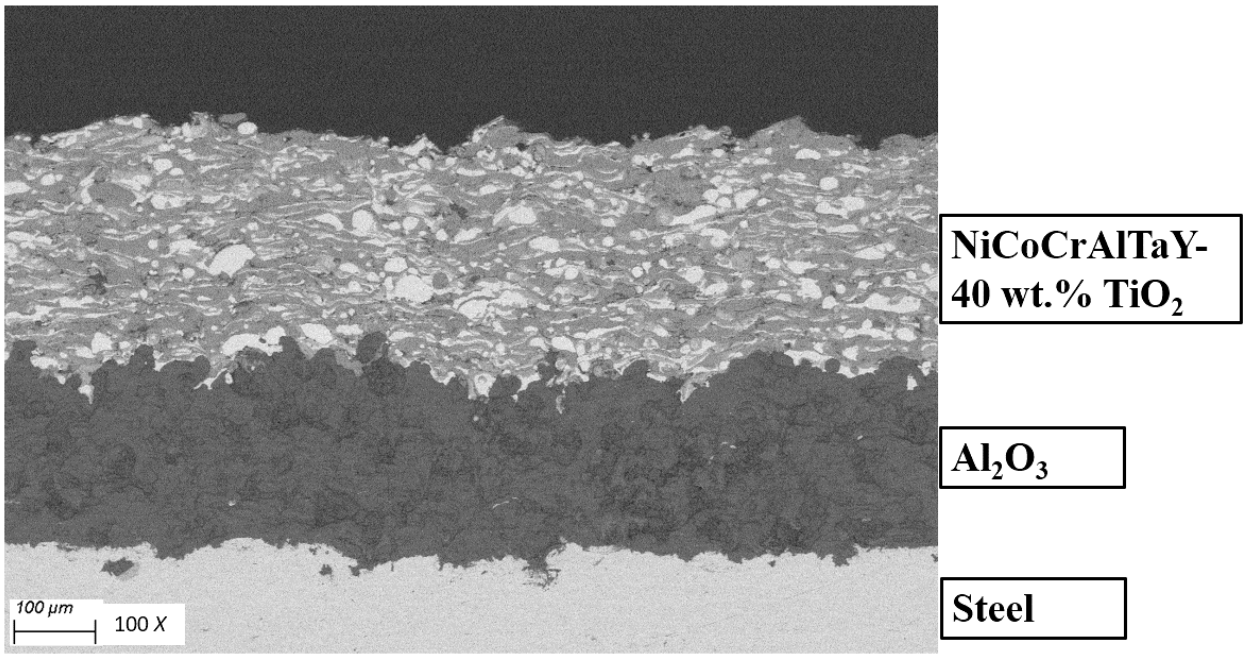

Figure 2-18 Back-scattered SEM image of the unloaded bi-layered coating-substrate system with NiCoCrAlTaY- 40 wt.% TiO_2

The presence of porosity reduces the effective cross-sectional area of the conductive layer and consequently causes an increase in its electrical resistance comparatively to the bulk material. This is because the presence of pores restricts electron flow through the material [74]. In this regard, the presence of pores in the nickel alloy coating might be beneficial with respect to its electrical resistance which can increase its sensitivity to strain changes. However, too many pores might also compromise the mechanical integrity of the coating. It is believed that the porosity range for the conductive layer in this work is well within the range of uncompromising elastic properties [75].

A scanning electron microscope (Zeiss Sigma 300 VP-FE, Carl Zeiss Canada Ltd., Toronto, ON, Canada) was used in backscattered electron mode to take micrographs of the cross-sectional area of the coating substrate system. It can be seen in Fig 2-16 that the nickel alloy penetrated the alumina layer. The penetration of the NiCoCrAlTaY coating into the alumina coating was mainly due to the presence of the network of these connected pores. This interlocking of the coating layers provided a better adhesive bonding which was very crucial to maintaining coating layers integrity when it was subjected to mechanical loading. Care was also taken to make sure the thickness of the alumina was enough to interlock with the nickel alloy without the nickel alloy penetrating deep enough to reach the substrate as this might cause short-circuiting of the system.

TiO_2 was also mechanically blended with NiCoCrAlTaY to increase the electrical resistance and possibly the piezoresistive response. As shown in Figs. 2-17 and 2-18, the TiO_2 (dark phases in the top layer) is well dispersed in the matrix. This dispersion was because the solid-solid interface energy of the NiCoCrAlTaY and TiO_2 phases was minimized to keep the system energy at the lowest, resulting in the penetration of the TiO_2 into the NiCoCrAlTaY [76 - 81]. Also, the porosities in the NiCoCrAlTaY - TiO_2 coatings were formed mostly at the interface of the

NiCoCrAlTaY and TiO_2 which is due to the difference in their surface energies because of their starkly different pre-sprayed morphologies. There is also evidence of mechanical interlocking between the NiCoCrAlTaY/ NiCoCrAlTaY - TiO_2 and Al_2O_3 which promotes the adhesion between the piezoresistive layer and the insulating layer. It is evident from the SEM images that there is good adhesion within the coating-substrate system and there are no delamination and cracks within the system.

Besides providing proper electrical insulation to the steel substrate and thereby avoiding short circuiting of the system, the intimate adhesion between the alumina and the substrate ensures efficient load transfer, through shear forces, from the substrate to the nickel alloy layer [82 - 83]. It should be noted that this load transfer is crucial to the functionality of the nickel alloy coating layer as a strain sensor. The good adhesion was maintained throughout the cyclic tests for all cases of the nickel alloy layer as can be seen in Fig. 2-19 to 2-24. This alludes to the fact that this is a well integrated coating-substrate system. It should also be noted that the final composition of the mechanically blended nickel alloy and titania differ significantly from the pre-deposited composition since there is little control over this final composition. This is shown in Table 2-2.

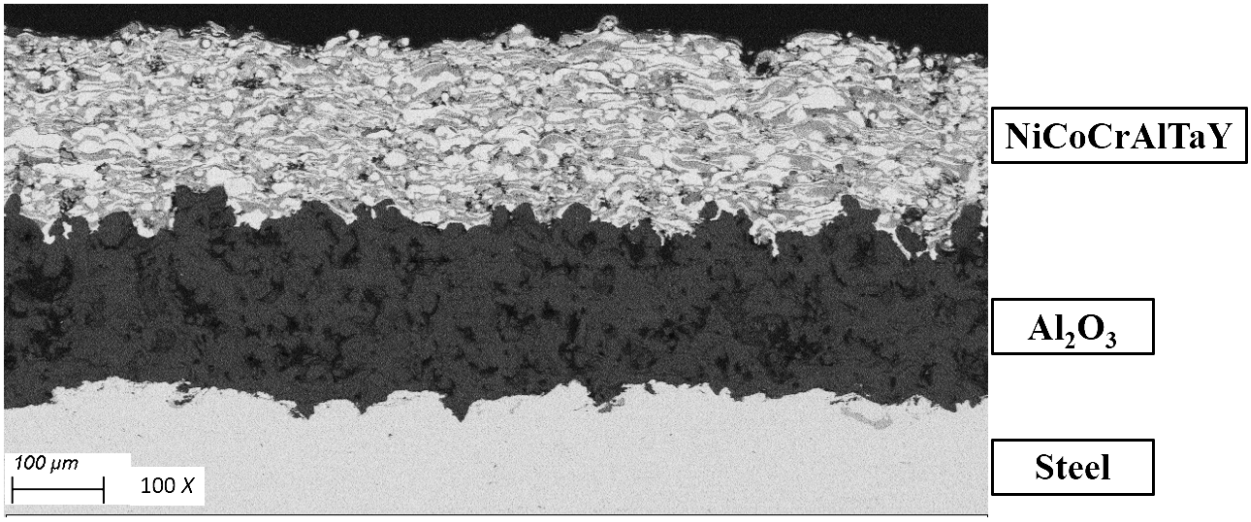

Figure 2-19 Back-scattered SEM image of the bi-layered coating-substrate system after 300 loading cycles for NiCoCrAlTaY as the conductive layer

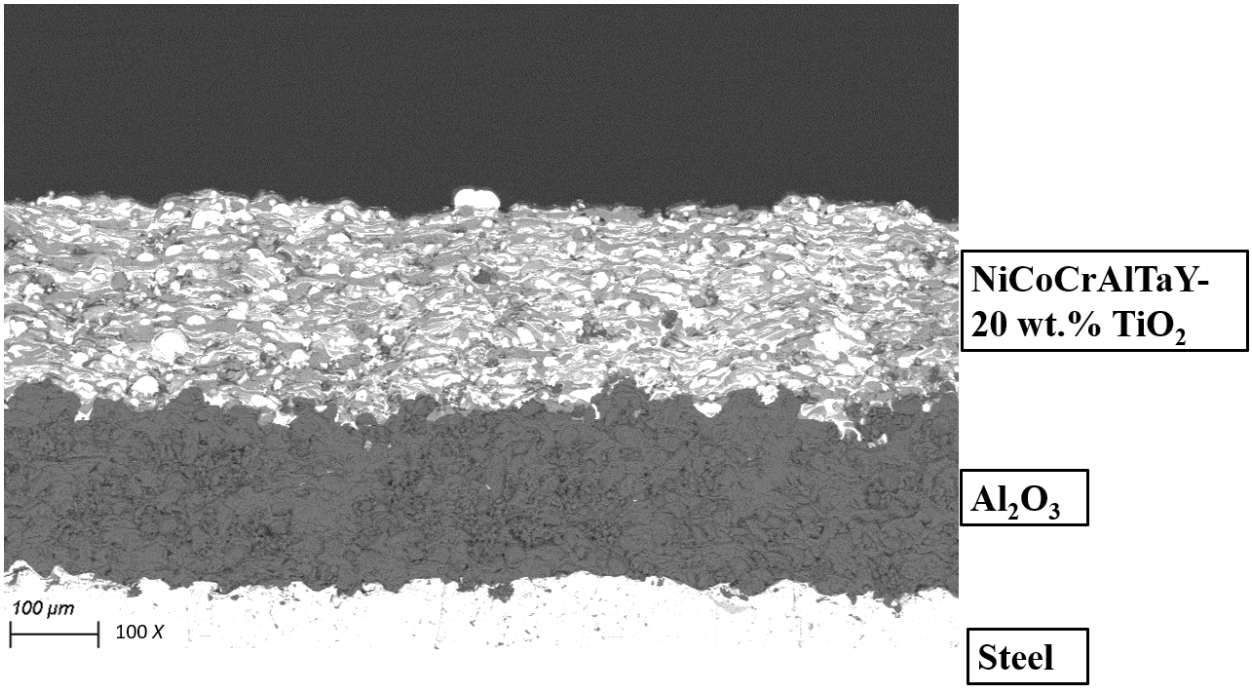

Figure 2-20 Back-scattered SEM image of the bi-layered coating-substrate system after 300 loading cycles with NiCoCrAlTaY-20 wt.% TiO_2 as the conductive layer

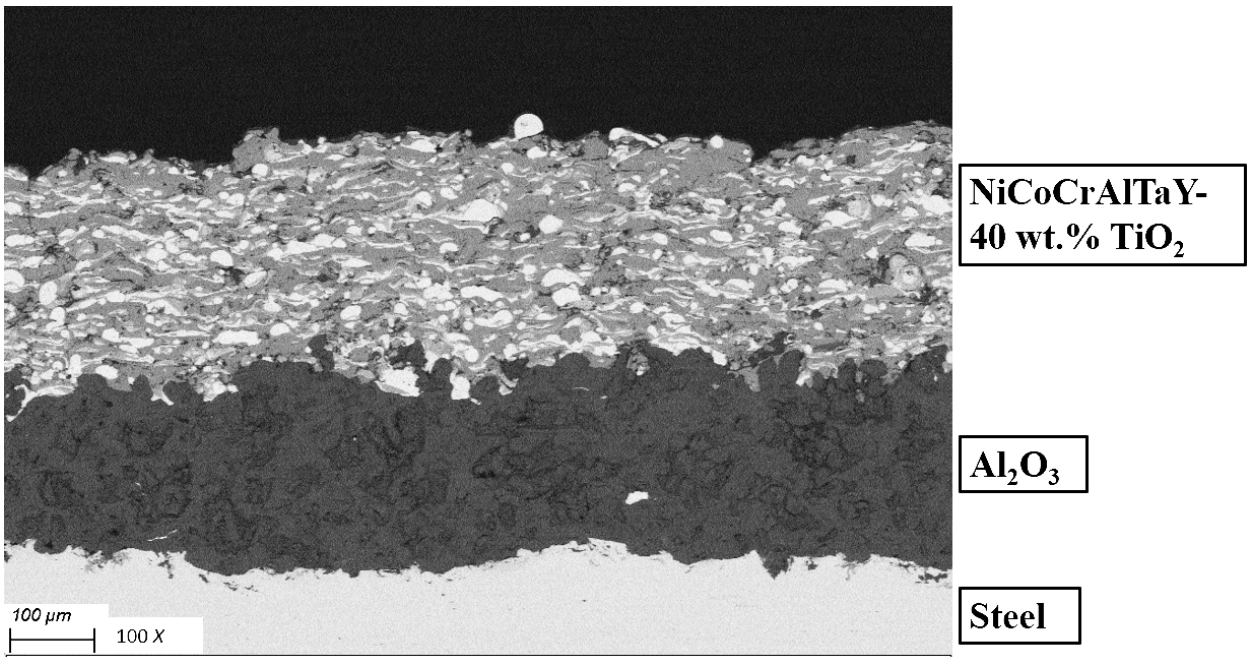

Figure 2-21 Back-scattered SEM image of the bi-layered coating-substrate system after 300 loading cycles with NiCoCrAlTaY- 40 wt.% TiO_2 as the conductive layer

Table 2-2 Thickness, porosity, and composition of the coating layers

Coating on flat steel substrate	**Average thickness [µm] (n = 5)**	**Average porosity [%] (n=5)**	**TiO_2 after deposition (vol.%)**
NiCoCrAlTaY	201 ± 5	1.823 ± 0.23	0
NiCoCrAlTaY – 20 wt. % TiO_2	197 ± 6	1.775 ± 0.35	39.95
NiCoCrAlTaY – 40 wt. % TiO_2	198 ± 4	1.572 ± 0.27	72.05
Al_2O_3	175 ± 6	23.11 ± 5.50	-

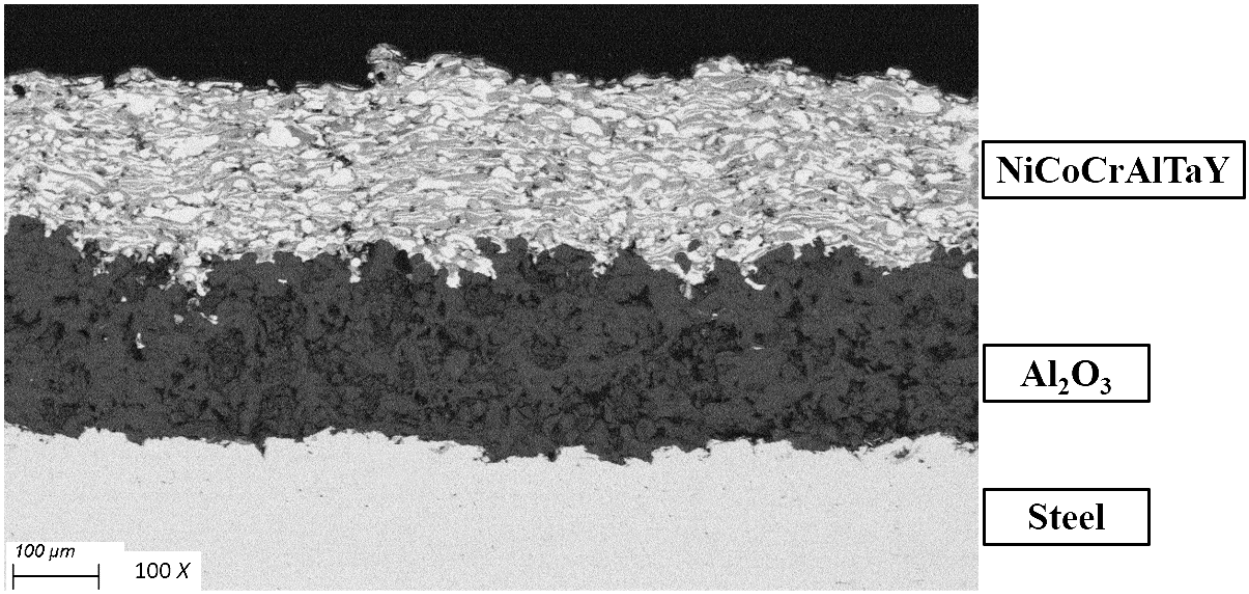

Figure 2-22 Back-scattered SEM image of the bi-layered coating-substrate system after 1000 loading cycles with NiCoCrAlTaY as the conductive layer

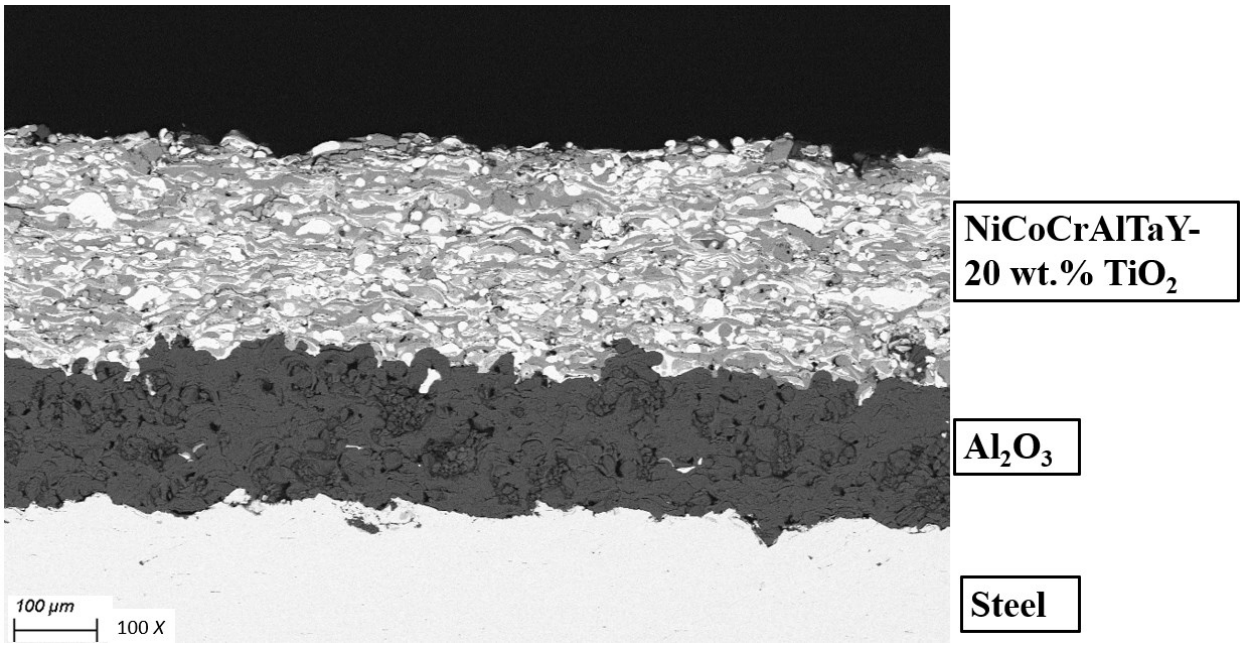

Figure 2-23 Back-scattered SEM image of the bi-layered coating-substrate system after 1000 loading cycles with NiCoCrAlTaY- 20 wt.% TiO_2 as the conductive layer

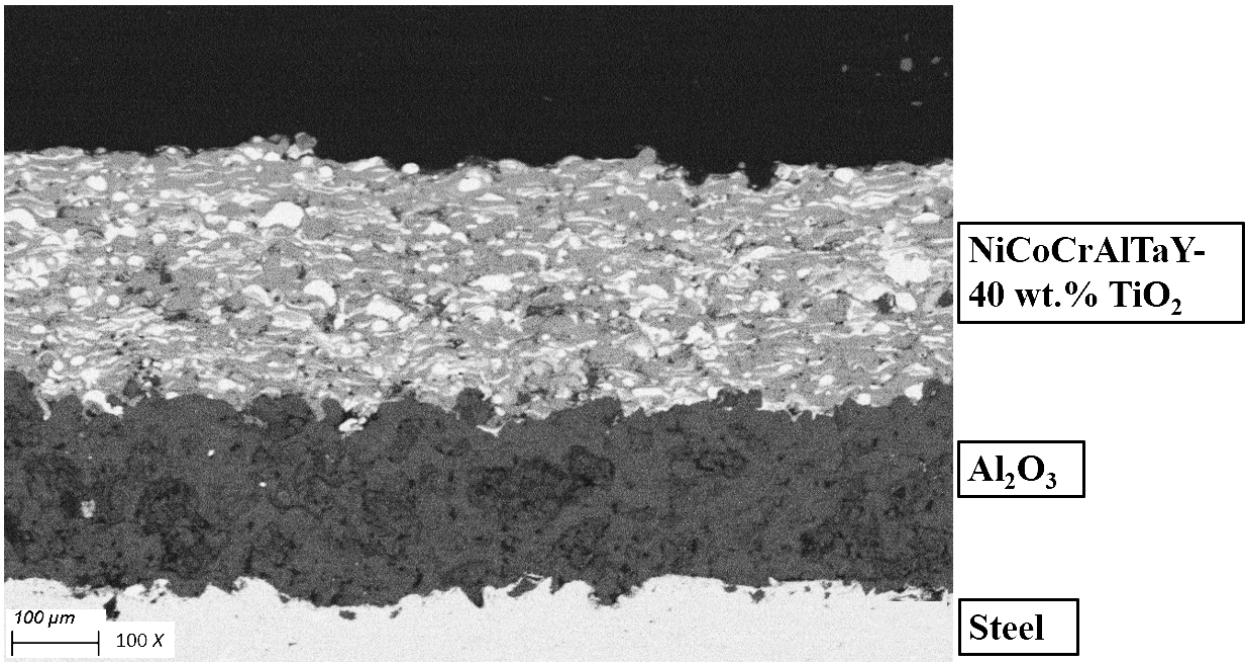

Figure 2-24 Back-scattered SEM image of the bi-layered coating-substrate system after 1000 loading cycles with NiCoCrAlTaY- 40 wt.% TiO_2 as the conductive layer

No crack propagation was observed in the cyclically loaded specimen and the interfaces were still intact which gave credence to the fact that thermally sprayed coatings can be fabricated to be intimately bonded to each other or the substrate. However, cracks propagation can be observed in the conductive layers for the uniaxial tensile test because the specimen was loaded to failure. It is interesting to observe that the interfaces still seemed intact (Fig. 2-25) for this uniaxially loaded test. The EDS maps of the conductive layer was done to understand the elemental composition and their possible oxidation. The distribution of the elemental constituents can be seen in the elemental maps shown in Figs. 2-26 and 2-27.

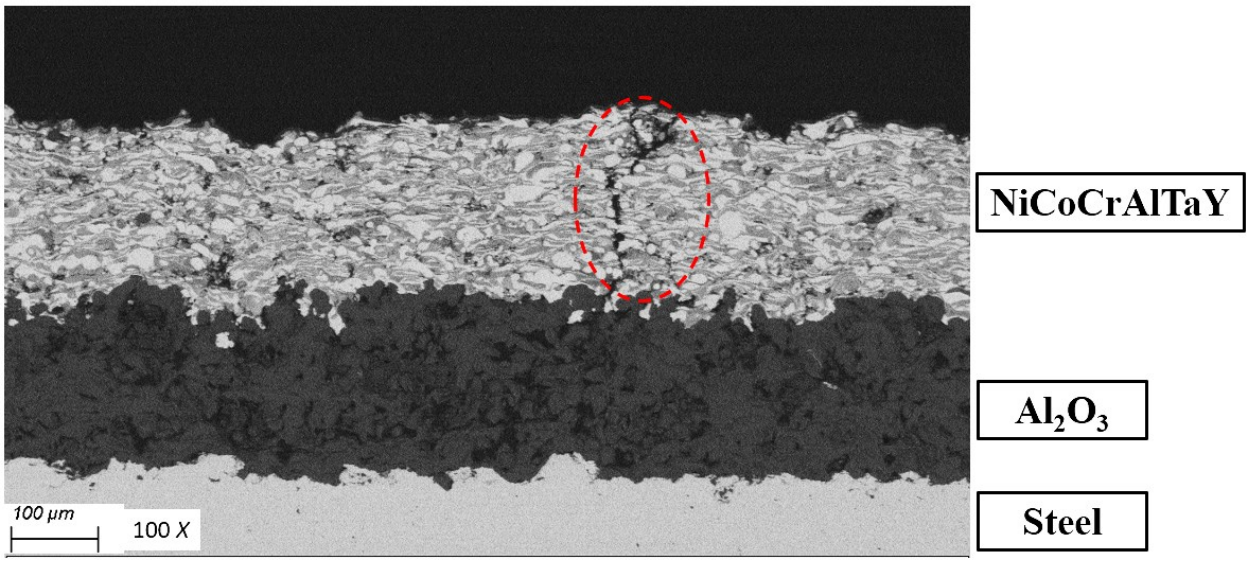

Figure 2-25 Back-scattered SEM image of the bi-layered coating-substrate system showing cracks after uniaxial tensile loading with NiCoCrAlTaY as the conductive layer

According to the EDS maps of the elemental constituents for the NiCoCrAlTaY layer in Fig. 2-26, all the elemental components seemed oxidized but there is stronger indication that Cr, Ta, and Y were oxidized. The light regions are mainly indicative of nickel and cobalt while aluminum oxide mainly occupies the darker regions [59, 84]. All other elemental components or their oxides occupy both regions simultaneously.

For the NiCoCrAlTaY-TiO_2 there was indication of the presence the following elemental oxides: Al and Ta. There is little or no indication of the presence of nickel oxide or cobalt oxide. Hence, the light region represents Ni and Co while the dark region represents Al_2O_3 and TiO_2. Cr Ta and Y (and possibly their respective oxides) occupy both the light and dark regions (Fig. 2-27).

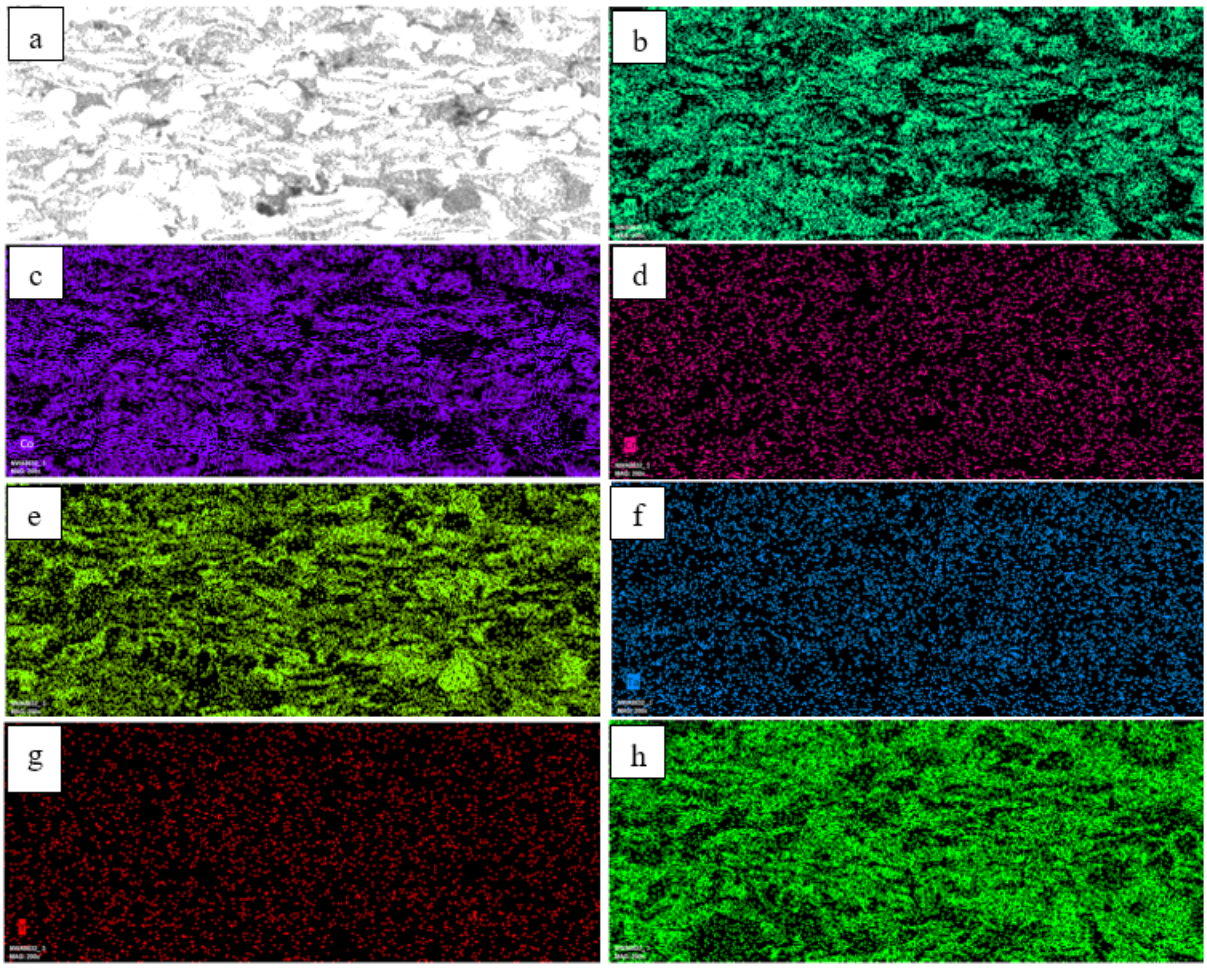

Figure 2-26 Representative (a) SEM images in backscattered electron mode and EDS mapping images of (b) nickel, (c) cobalt, (d) chromium, (e) aluminum, (f) tantalum, (g) yttrium, and (h) oxygen for the NiCoCrAlTaY layer

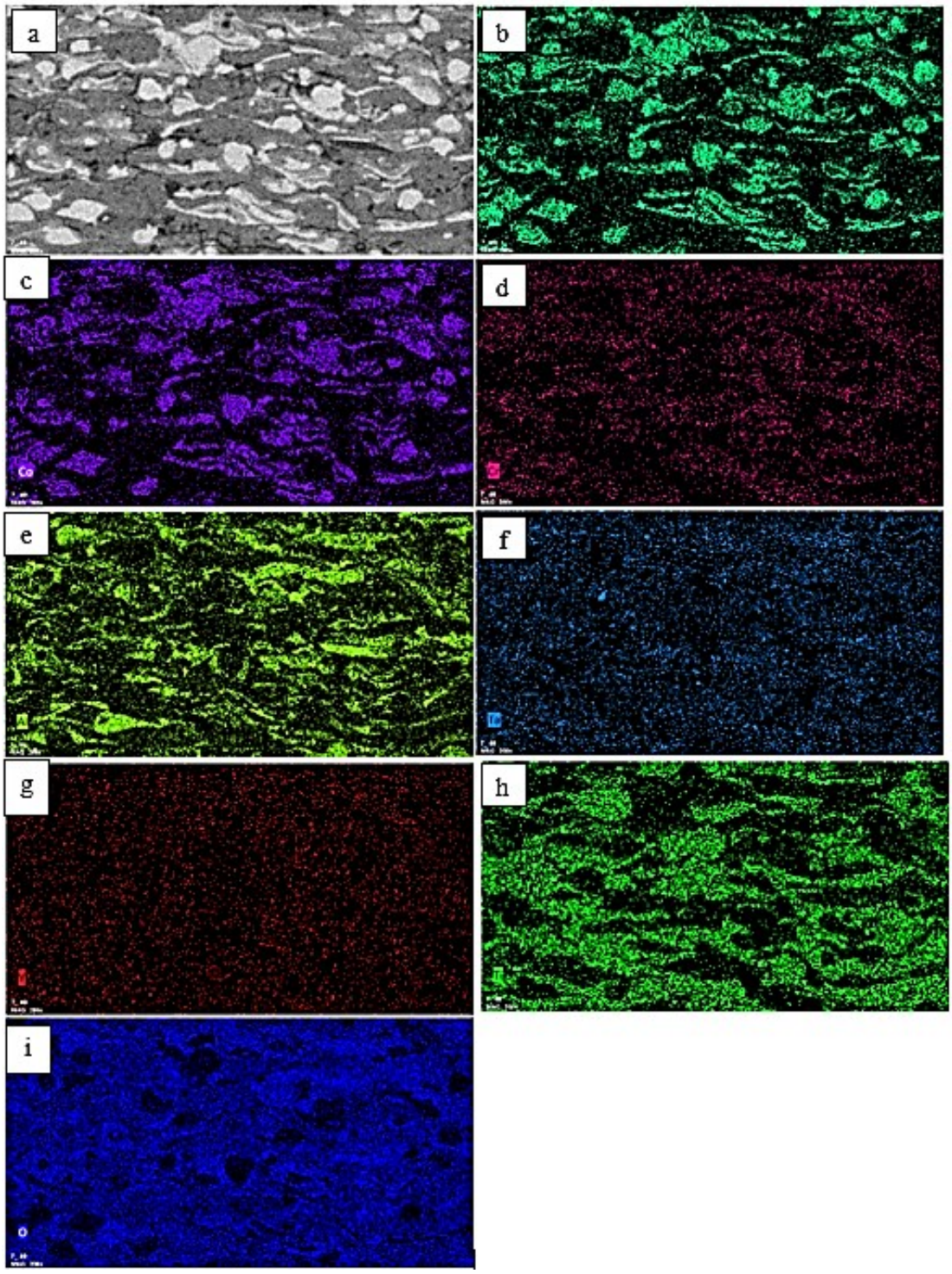

Figure 2-27 Representative (a) SEM images in backscattered electron mode and EDS mapping images of (b) nickel, (c) cobalt, (d) chromium, (e) aluminum, and (f) tantalum (g) yttrium, (h) titanium, and (i) oxygen for the NiCoCrAlTaY- TiO_2 layer

Scanning electron microscopy on coated carbon fiber reinforced polymer substrate

NiCoCrAlTaY was also deposited on carbon fiber reinforced polymer (CFRP) with quasi-isotropic construction lay-up (Fig. 2-28). Since the CFRP is electrically conducting because of the slightly exposed carbon fibers, alumina was also deposited on the CFRP as the insulating layer. The coating thickness obtained was relatively much thinner than for the steel substrate because the CFRP could not be exposed to the oxy-acetylene flame for too long. The porosity is also much less in this case since the thickness is one order of magnitude lower than that of steel. There is also pronounced interlocking within the coating-substrate system. This is shown in the SEM image of Fig. 2-29.

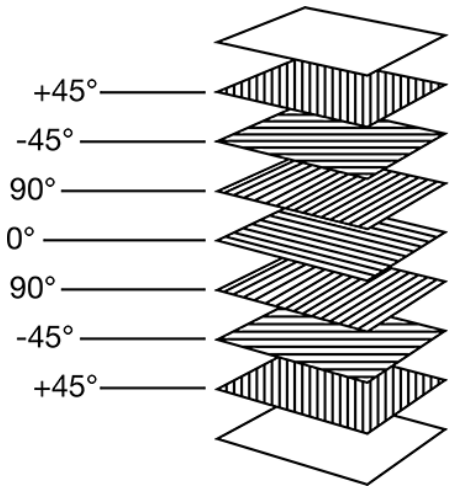

Figure 2-28 Carbon fiber reinforced polymer (CFRP) with quasi-isotropic construction lay-up [85]

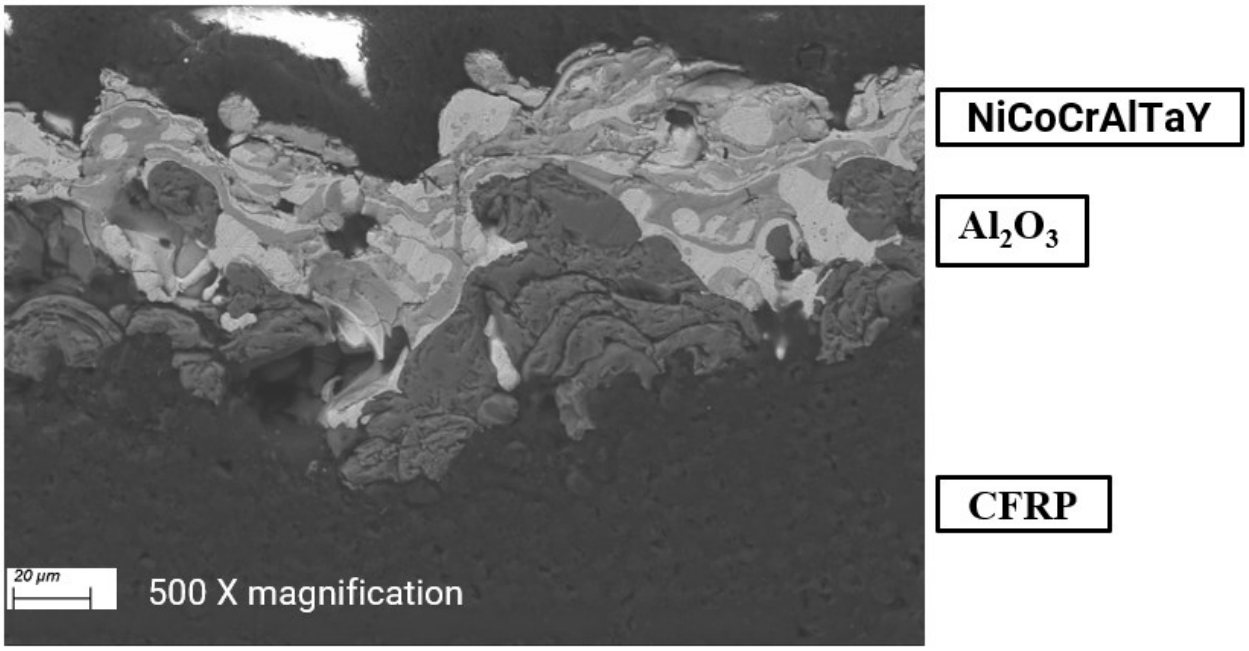

Figure 2-29 SEM image of the unloaded bi-layered coating-substrate system with NiCoCrAlTaY as the conductive layer (top layer) and carbon fiber reinforced polymer (CFRP) as the substrate

X-ray diffraction

The crystalline materials accompanying the deposition of the NiCoCrAlTaY and NiCoCrAlTaY-TiO_2 powders were shown in Fig. 2-30. In both cases, there is evidence of formation of new symmetric cubic structures such as the non-stoichiometric forms of NiAl and CoNi. The degrees of crystallinity for both NiCoCrAlTaY and NiCoCrAlTaY-TiO_2 were calculated to be 77.09 % and 100 %, respectively. The symmetry and degree of crystallinity helps in achieving more sensitivity of the coating to strain measurements [86].

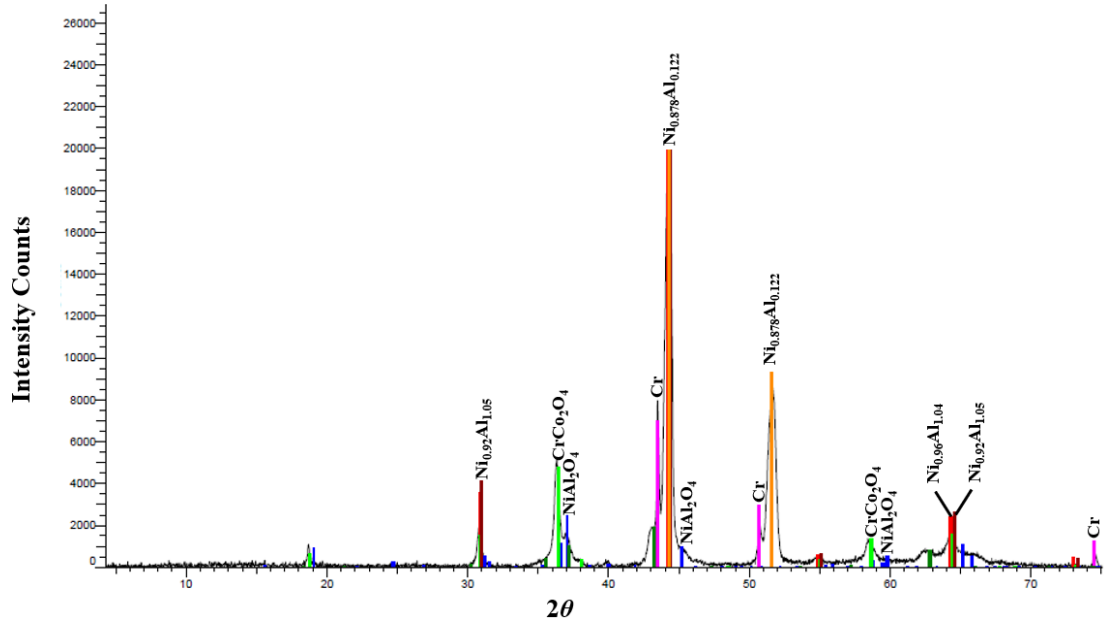

(a)

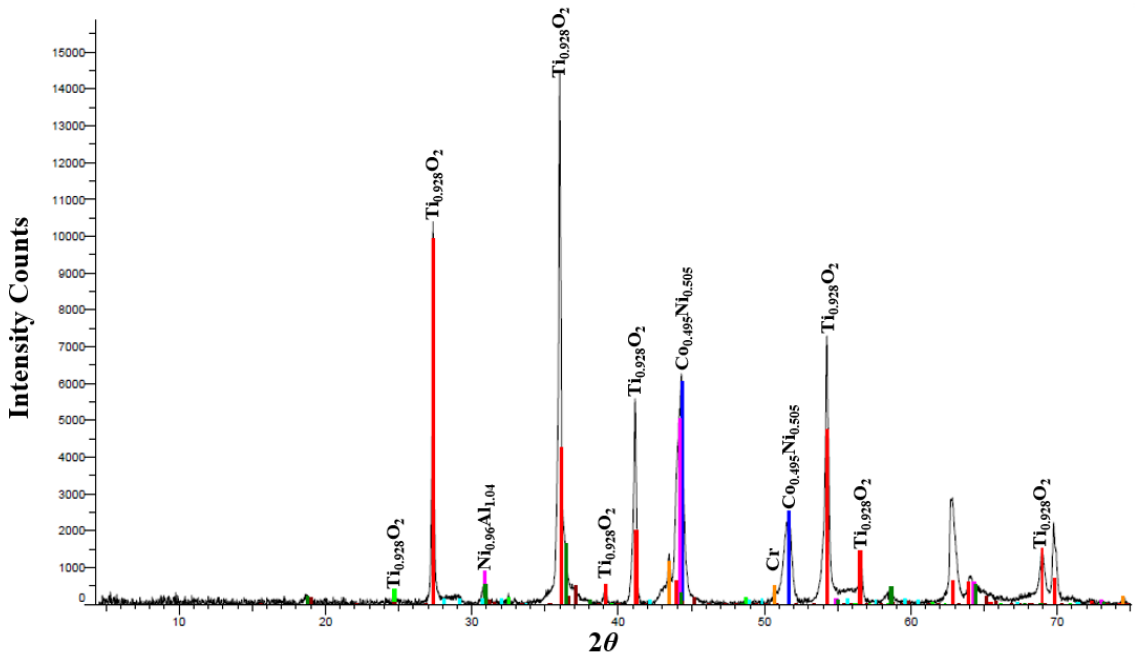

(b)

Figure 2-30 XRD profile of the (a) as-sprayed NiCoCrAlTaY, and (b) NiCoCrAlTaY-TiO_2 coating layers

2.2.2 Temperature coefficient of resistance (TCR)

While the porosity and the addition of TiO_2 in the conductive layer could desirably influence the electrical resistance in the context of this research, an unwanted factor that also influences electrical resistance and needed to be accounted for, or minimized is temperature. In this regard, the temperature coefficient of resistance (TCR) of the coating was investigated.

For the TCR test, the average surface temperature against electrical resistance plot is shown in Fig. 2-31. The temperature increased to almost 90 ^{o}C for the test duration. From the plot, TCR of the NiCoCrAlTaY coating was calculated to be 0.0011842/K according to Eq. 2-3. The positive TCR value showed that resistance of the conductive layer would increase as temperature increased and, based on the result obtained here, the supply voltage and current for subsequent electromechanical tests, were limited to maximum values of 7 V and 1 A, respectively, to limit the temperature contribution to electrical resistance change.

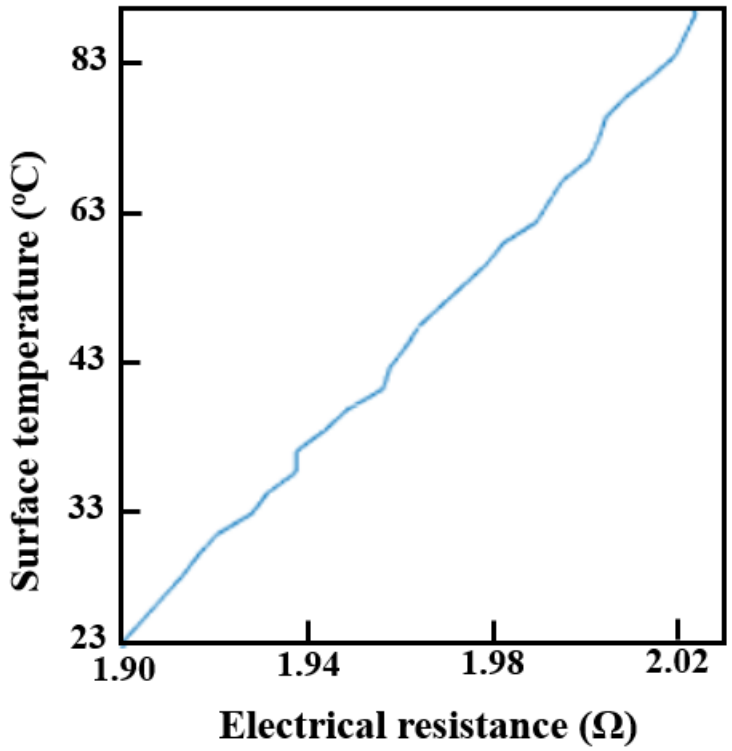

Figure 2-31 Average surface temperature versus electrical resistance plot for the NiCoCrAlTaY coating

2.2.3 Nanoindentation test

Table 2-3 presents the elastic properties obtained from the indentation measurements. It was observed that the insulating layer exhibited a higher degree of compliance compared to the other layer. This characteristic proves highly beneficial for facilitating the transfer of mechanical loads, as the deformation of the substrate is effectively transmitted entirely through the insulating layer. The compliance of the insulating layer enhances the load transfer mechanism, ensuring efficient stress distribution and minimizing the potential for localized stress concentrations. This finding underscores the significance of the insulating layer in maintaining structural integrity and optimizing the overall performance of the coating system.

Table 2-3 Elastic properties from nano-indentation

Material	Hardness (GPa)	Elastic modulus (GPa)
Conductive layer (NiCoCrAlTaY)	9.71 ± 4.31	218.72 ± 81.96
Insulating layer (Al_2O_3)	2.35 ± 2.03	43.81 ± 9.70

2.2.4 Electromechanical Test

As a confirmation of the measurement error, a static test was performed. In this static test, 300 s worth of data for both the electrical and strain data were recorded of a specimen with no applied load. These are presented in Fig. 2-32 and Fig. 2-33. It was found that the measurement noise from both data were negligible.

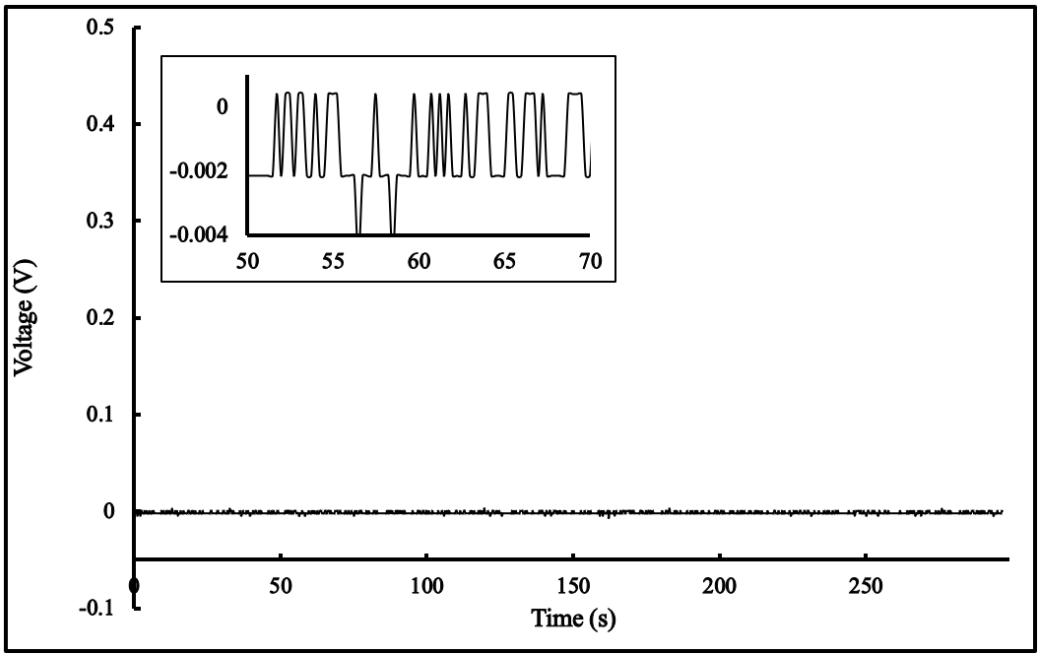

Figure 2-32 Static observation of the bridge voltage, and (b) the strain data with no mechanical loading. Insert is zoomed in to show fluctuations at magnified values

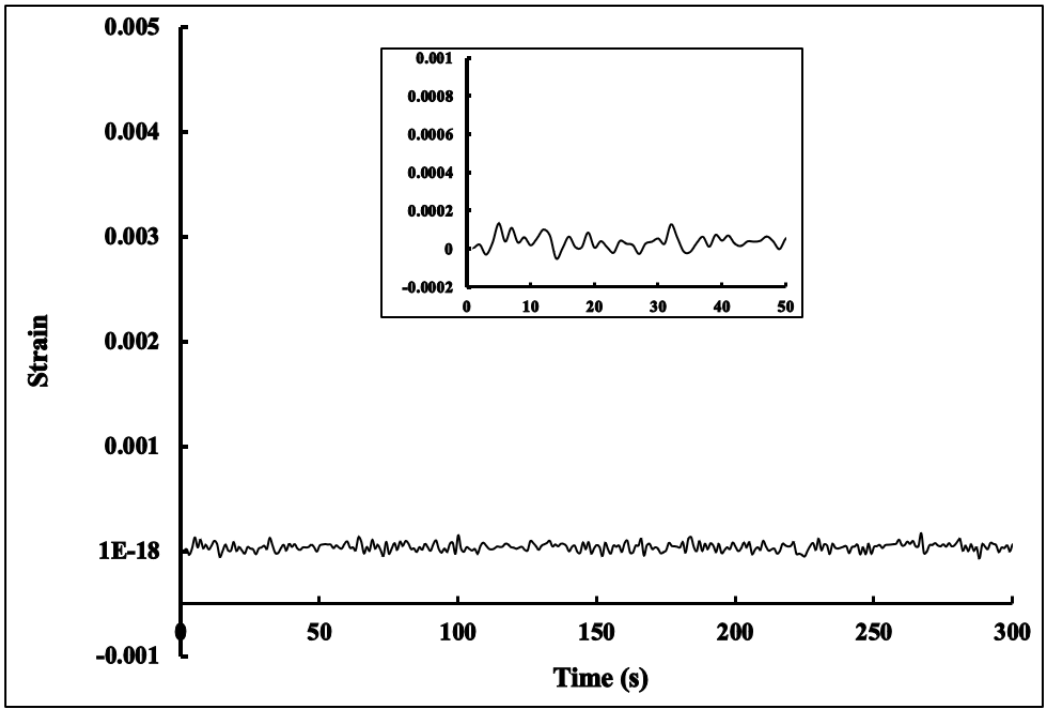

Figure 2-33 Static observation of the strain data with no mechanical loading. Insert is zoomed in to show fluctuations at magnified values

Tests on flat steel sample

By subjecting the NiCoCrAlTaY bi-layered coating-substrate system to the extension and compression cycles, strain cycles between -1000 μm and +1700 μm were generated with an approximately 5% difference between peaks and troughs of the relative electrical resistance change plot. The loading cycles and the resulting electromechanical responses are presented in Fig. 2-34. The proportionality of the relative electrical resistance change, $\Delta R/R$ to the longitudinal strain, ε is indicated by the correspondence in the periodicity of both the relative electrical resistance change and strain plots (right inset in Fig. 2-34). As complemented by the SEM images for the deformed coating-substrate system, the stability and generally lower relative resistance change in the relative electrical resistance change plot after about 250 cycles indicated that densification of the coating

was achieved through collapse of some pores. Between 250 and 1000 cycles, there was no drastic change in the relative electrical resistance, which indicates that the coating did not undergo major damage.

The strain plot in Fig. 2-34 further buttressed this by showing that the strain cycle has good consistency for the duration of the loading cycles which could mean that there was no significant damage to the coating. A concern that usually arises during tensile loading of coating-substrate system is the inherent competition between delamination of the interface(s) and cracking in the coating [20, 87 - 89]. This could affect the DIC reading due to the apparent movement of the partly detached coating layer which could give off a wrong strain reading. This concern was addressed by the intact Al_2O_3-NiCoCrAlTaY and Al_2O_3 – substrate interfaces at the end of the cyclic test as revealed by the SEM images in Figs. 2-16 to 2-25.

For the NiCoCrAlTaY-20 wt.% TiO_2, the bi-layered coating-substrate system was also subjected to extension and compression cycles and the corresponding strain cycles generated was between -1000 μm and +2000 μm. This resulted in approximately 30 % difference between peaks and troughs of the relative electrical resistance change plot. In this case, the coating showed more sensitivity than the system with NiCoCrAlTaY as the substrate. The loading cycles and the resulting electromechanical responses are presented in Fig. 2-35 (a). Since resistivity closely relies on the microstructure, which includes phase composition, pore shape and size the TiO_2 introduced into the nickel alloy coating might have contributed to the increase in the sensitivity and the general increase in electrical resistance because TiO_2 is electrically more resistive than the nickel alloy. It was noted that at around 860 loading cycles, the relative electrical resistance change changed abruptly. Though the strain cycle remains consistent, the abrupt change might be due to abrupt changes in the pores' dimensions in the conductive layer [90 - 96].

The NiCoCrAlTaY-40 wt.% TiO_2 showed similar electrical resistance changes like the NiCoCrAlTaY-20 wt.% TiO_2 (Fig. 2-35 (b)). The resulting strain cycles in this case is between -500 µm and +2000 µm. It is obvious that introducing the TiO_2 has influence on the piezoresistive response of the conductive layer. Also, the introduction of the TiO_2 seemed to increase the compliance of the nickel alloy as the range of strain values experienced with each composition of the nickel alloy increased with TiO_2 content. In this cyclic case, there was consistent lateral compression of the coating layer which would give a denser and thus a coating property close to the bulk material than for the uniaxial tensile case [91, 92, 94, 95].

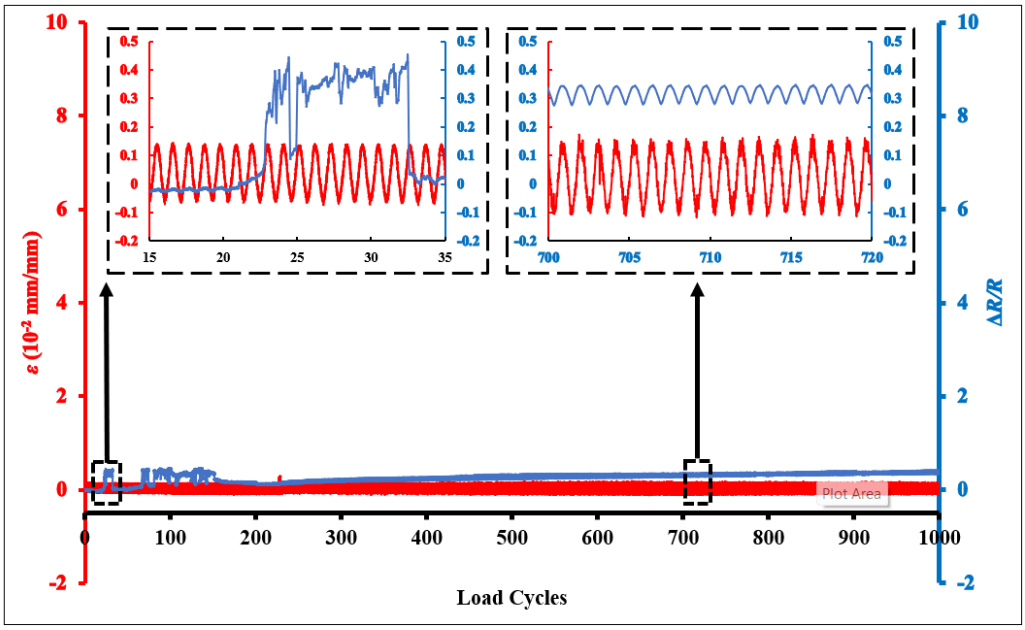

Figure 2-34 Electromechanical plots of the bi-layered coating-substrate system with NiCoCrAlTaY as the conductive layer

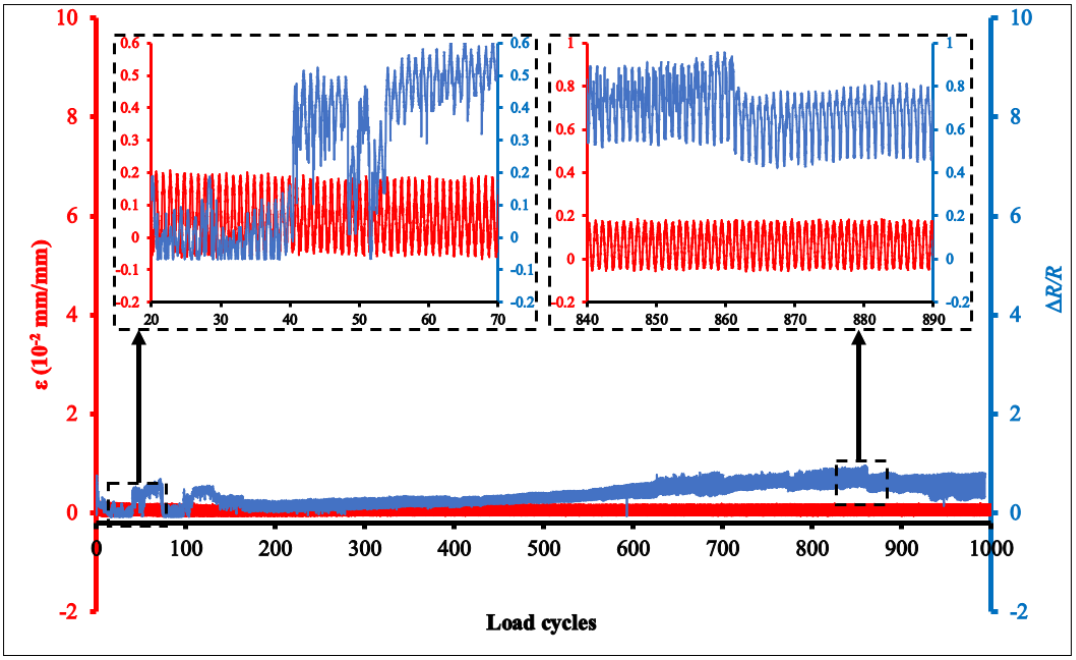

(a)

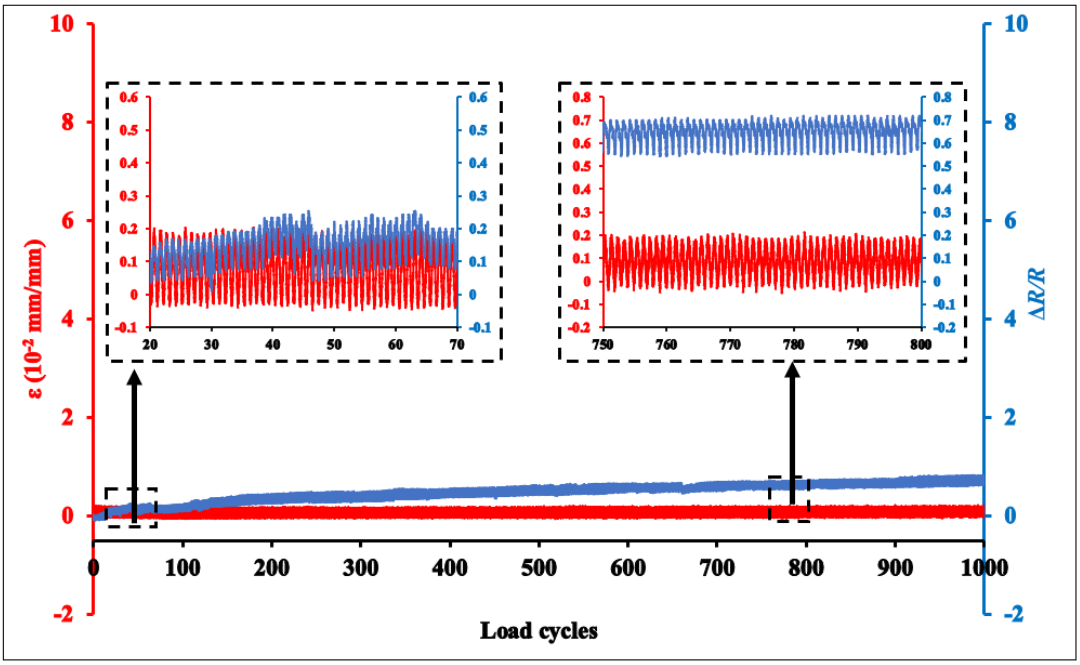

(b)

Figure 2-35 Electromechanical plots of the bi-layered coating-substrate system with (a) NiCoCrAlTaY-20 wt.% TiO_2 as the conductive layer, and (b) NiCoCrAlTaY- 40wt.% TiO_2 as the conductive layer

Under uniaxial tensile loading, the coating showed approximately bi-linear behavior in the $\Delta R/R$ of the NiCoCrAlTaY against strain (Fig. 2-36). This means the coating showed two sensitivities before its final failure at around 5 x 10^{-3} mm/mm. Using linear regression model, the gauge factors, *GF* of the linear parts of the graph (enclosed in a dotted box in Fig. 2-36) before coating failure are 64.57 at low strain values (below 8 x 10^{-4}) and 146.86 between 8 x 10^{-4} and 5 x 10^{-3}. The gauge factor is given as:

$$GF = \frac{\left(\frac{\Delta R}{R}\right)}{\varepsilon} . \qquad (2\text{-}7)$$

The coefficients of determination, r^2, for each linear part are 0.97 and 0.98, respectively. The high r^2 values imply that most of the variability in $\Delta R/R$ due to ε is explained by the regression model. The high *GF* values and bi-linearity are uncharacteristic of metallic alloys therefore, as revealed by the XRD in Fig 2-30 (a), the formation of the several species after the deposition of the coating might be responsible for this bi-linearity [97 - 98].

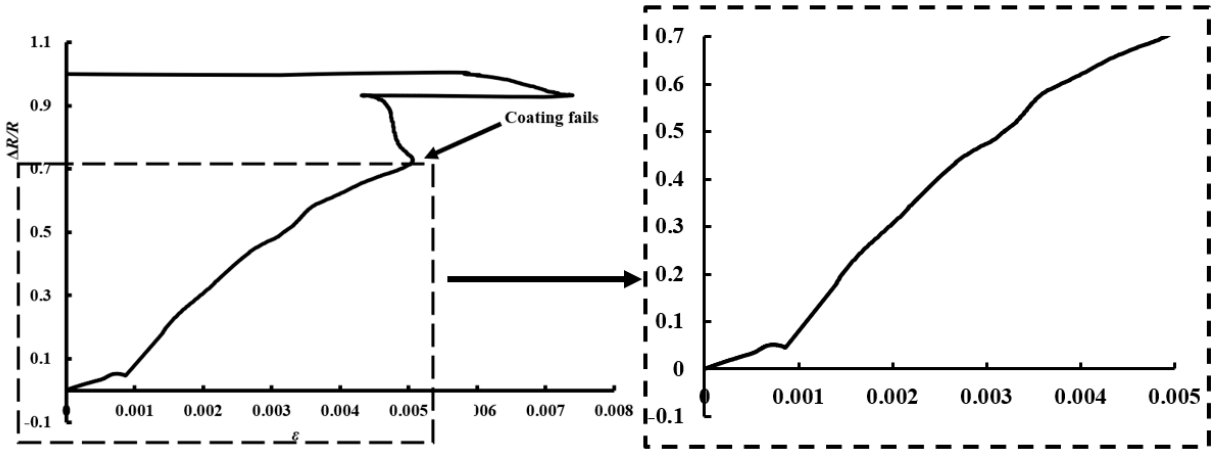

Figure 2-36 Relative electrical resistance change against strain plot for NiCoCrAlTaY with the part before the coating failed zoomed in

Tests on cylindrical steel sample

In this case, the conductive layer is NiCoCrAlTaY. The results of the coating subjected to different internal pressures of 31 MPa (4500 psi), 41.4 MPa (6000 psi) and 55.2 (8000 psi) are shown in Fig. 2-39 (a), (b), and (c), respectively. Figure 2-37 shows the plots of strain and relative electrical resistance change against load cycles. The plot for the 55.2 MPa (8000 psi) showed more consistency regarding the electrical resistance change from the beginning of the test. This could mean that the higher pressure densified the coating faster than the coating faster. It is interesting to note that though the strains stay approximately the same with the internal pressure, the relative electrical resistance change generally slightly reduced with the pressure. This could also be because of the pore dimension change pointed out earlier in the sense that the higher pressure collapsed the pore sizes faster [90 - 96].

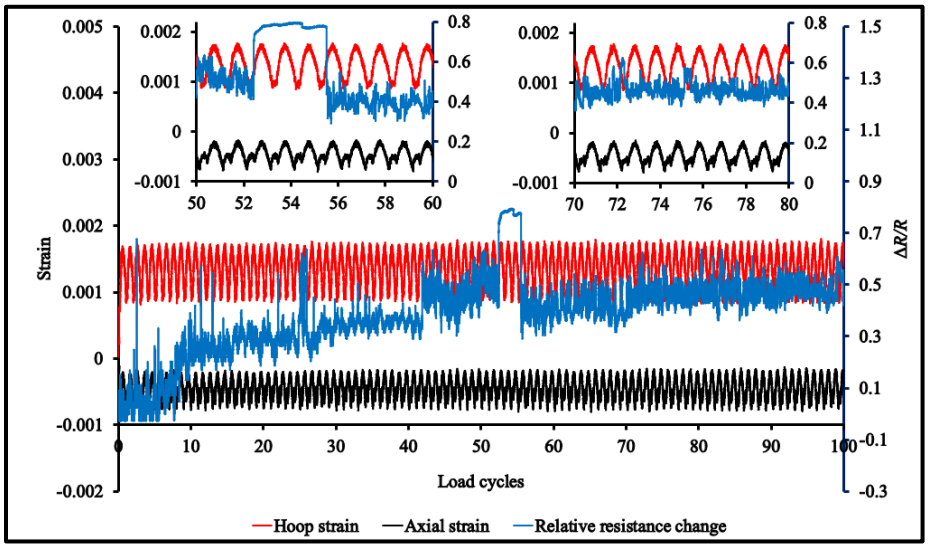

(a)

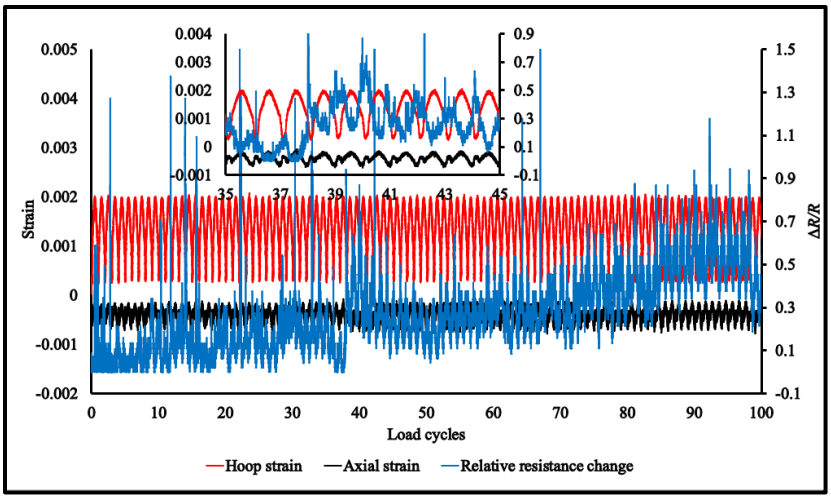

(b)

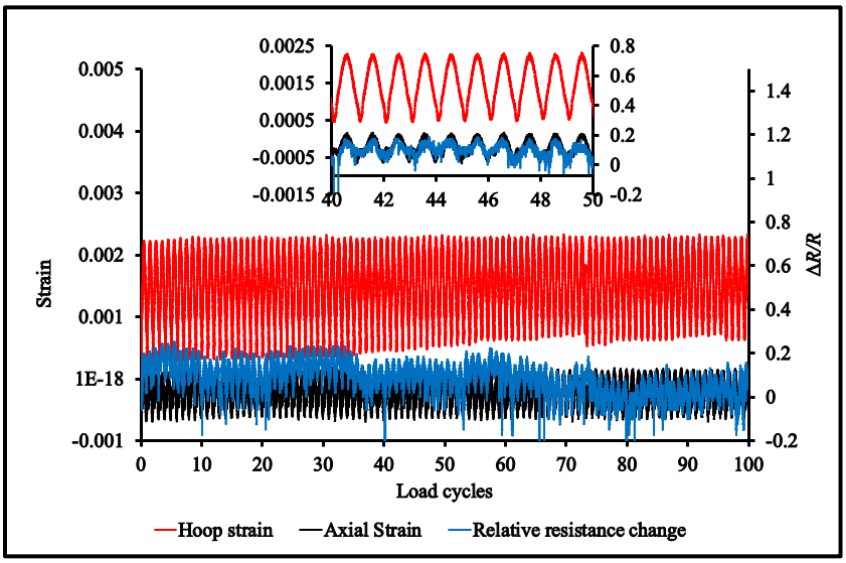

(c)

Figure 2-37 Plots of hoop strain, axial strain and relative electrical resistance change against strain plot for NiCoCrAlTaY at different internal pressures of (a) 31 MPa (4500 psi), (b) 41.4 MPa (6000 psi), and (c) 55.2 MPa (8000 psi)

With the present symmetric loading conditions and consequently symmetric strain, the stresses generated in the cylinder will only depend on the radius, r of the cylinder and not the angle, θ shown in Fig. 2-38. This is also contingent on the assumption that the material is

homogenous, isotropic, and that the loading conditions do not exceed the cylinder's elastic limit [58].

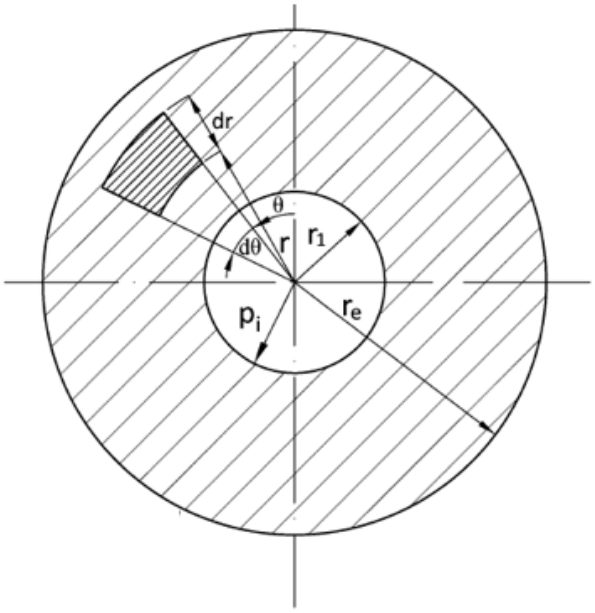

Figure 2-38 Cross section of a thick-walled circular cylinder [37, 58]

Since the cylinder is only internally pressurized, there is zero external pressure on it and the stress distribution within the cylinder can be simplified as follows [58]:

$$\sigma_r = \frac{p_i r_i^2}{r_e^2 - r_i^2}\left(1 - \frac{r_e^2}{r}\right) = \frac{p_i}{\delta^2 - 1}\left(1 - \frac{r_e^2}{r}\right) = K'\left(1 - \frac{r_e^2}{r}\right), \tag{2-8}$$

$$\sigma_t = \frac{p_i r_i^2}{r_e^2 - r_i^2}\left(1 + \frac{r_e^2}{r}\right) = \frac{p_i}{\delta^2 - 1}\left(1 + \frac{r_e^2}{r}\right) = K'\left(1 + \frac{r_e^2}{r}\right), \tag{2-9}$$

and because the cylinder is closed but, unrestricted with no thermal stresses, the axial stress is

$$\sigma_z = \frac{p_i r_i^2}{r_e^2 - r_i^2} = \frac{p_i}{\delta^2 - 1} = K', \tag{2-10}$$

where

$$\delta = \frac{r_e}{r_i}, \tag{2-11}$$

where σ_r, σ_t, σ_z, p_i, r_i. and r_e are the radial stress, tangential (hoop) stress, axial stress, internal pressure, inner radius and out radius, respectively.

Based on Eqns. (2-8) to (2-11), the plots of the axial stress, hoop stress and internal pressure are shown in Fig. 2-39. It is obvious from the figure that the hoop stress is the maximum stress within the cylinder. That is why a crack is most likely to appear along the length of the cylinder. According to the equations, the radial stress varies inversely with the radius and thus, maximum at the inner radius and becomes zero at the outer surface. In this regard, radial stress is positive, and its absolute maximum value is also reached at the inner radius, while it is zero at the outer radius.

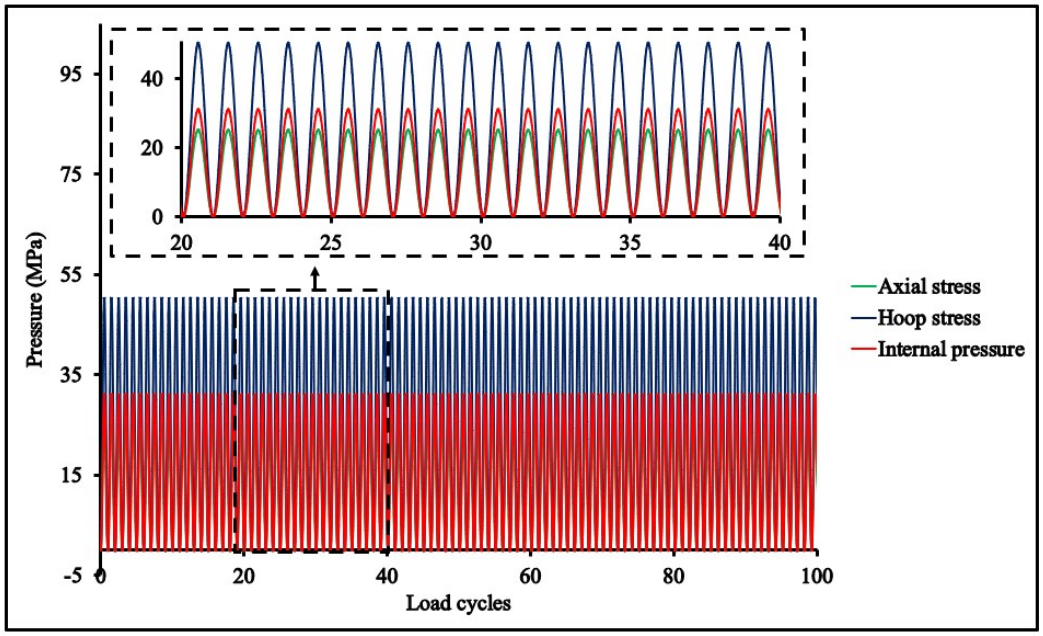

(a)

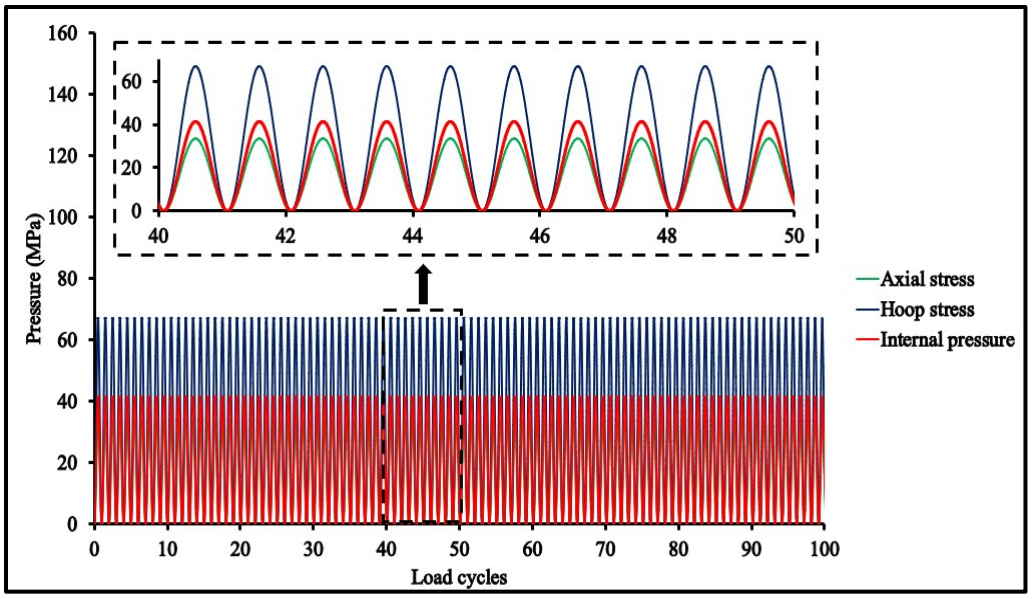

(b)

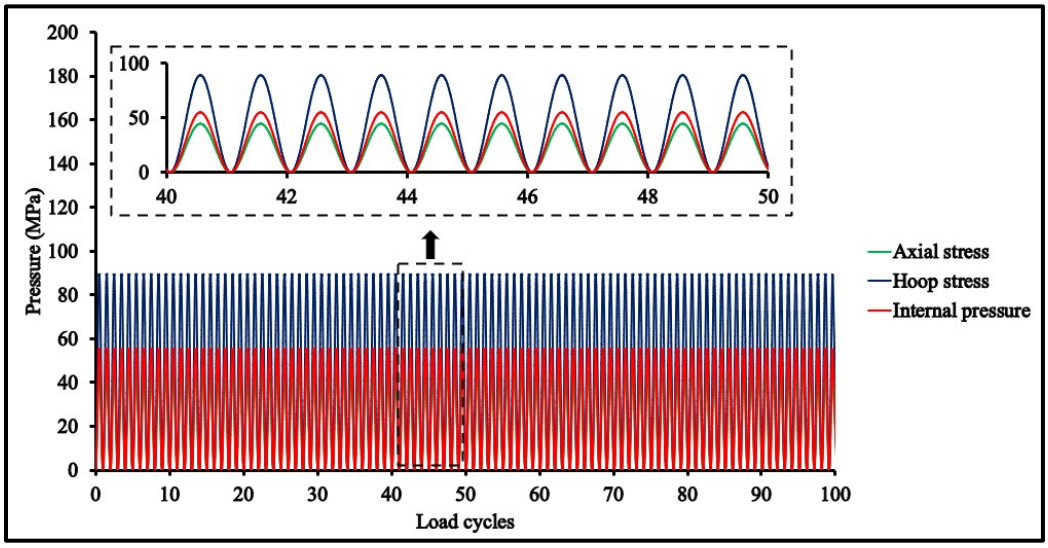

(c)

Figure 2-39 Plots of axial stress, hoop stress, and internal pressure at the outer radius at different internal pressures of (a) 31 MPa (4500 psi), (b) 41.4 MPa (6000 psi), and (c) 55.2 (8000 psi)

Also, given that the outer radius is always greater than the inner radius, the radial stress is always negative. Consequently, the radial stress at the inner radius is equal to the internal pressure but opposite in direction.

Tests on carbon fiber reinforced polymer (CFRP) sample

Comparatively, the coating layer achieved more extension on the CFRP (Fig. 2-40) than on steel for the uniaxial tensile test. However, much less sensitivity was achieved. In this case, the coating and the substrate failed at about the same time.

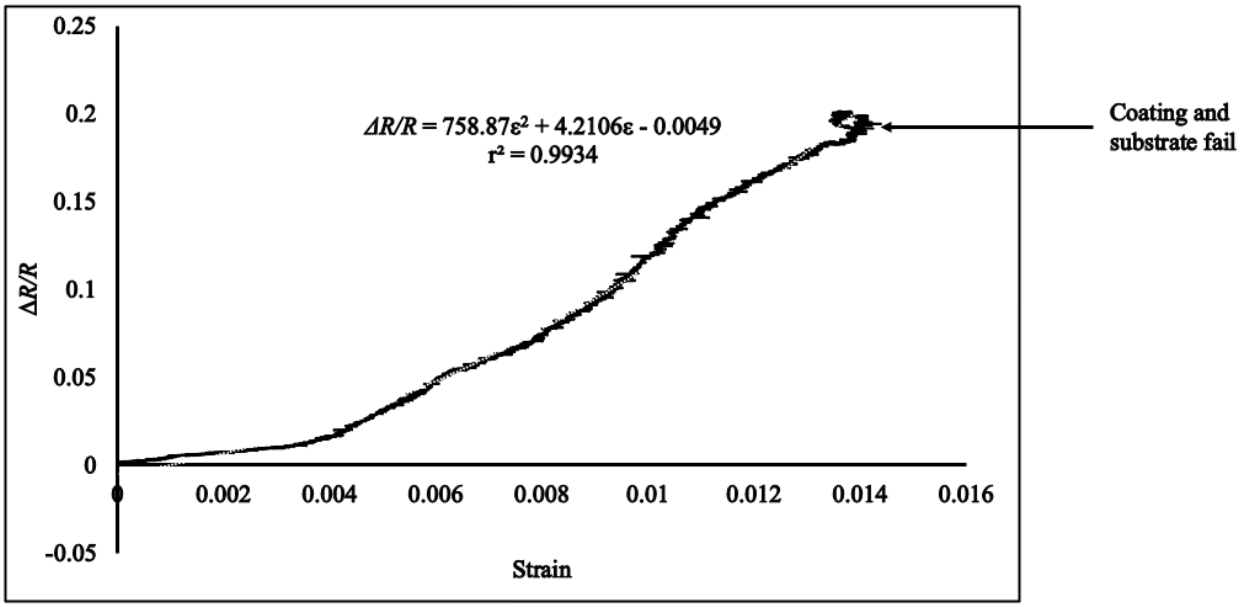

Figure 2-40 Electrical resistance against strain plot for uniaxially loaded NiCoCrAlTaY coating with carbon fiber reinforced polymer as the substrate

Considering that the curve is non-linear, Eq. (3-6) [77, 99] can be used to determine gauge factor, *GF* of the coating in this case. Approximately, based on the equation of the curve in Fig. 2-40, the gauge factor, *GF* is 4.2. Though this is significantly lower than that on steel, more stretchability was achieved on the polymer than on the steel.

$$\left(\frac{\Delta R}{R}\right) = GF\varepsilon + C\varepsilon^2 \tag{2-12}$$

2.3 Conclusions

The study focused on examining the sensitivity of a piezoresistive coating to temperature, electrical resistance changes, mechanical load, and strain variations. It aimed to minimize sensitivity to temperature while desiring increased sensitivity to electrical resistance and strain changes with minimal mechanical load. Additionally, the coating's elastic properties should not be significantly compromised due to the presence of porosities. These properties serve as crucial benchmarks for evaluating the functionality of a piezoresistive coating.

To meet these requirements, flame spraying process was utilized to create a bi-layered coating-substrate system on flat steel, flat carbon fiber reinforced polymer (CFRP), and cylindrical steel substrates, with the aim of developing the strain sensor. The conductive coating consisted of a mechanical blend of NiCoCrAlTaY and TiO_2, while Al_2O_3 was employed as the insulating layer. Thereafter, the fabricated coatings were characterized through scanning electron microscopy (SEM), energy-dispersive X-ray spectroscopy (EDX), and X-ray diffraction (XRD) techniques. The electromechanical performance of the coating-substrate system was evaluated through quasi-static tensile and quasi-static cyclic tests, accompanied by in *situ* electrical measurements at room temperature. Additionally, the microstructure of some of the coating-substrate systems was examined using SEM after the electromechanical tests to correlate the observed changes with the test results and assess any potential damage to the coating.

From the tests conducted, the following conclusions were drawn:

- From the SEM images, the TiO_2 was well-dispersed in the nickel alloy phase after deposition. Also, there was evidence of mechanical interlocking at the conductive layer-insulating layer interface and insulating layer- substrate interfaces. The images thus

confirmed that the bi-layered system was well-integrated because the conductive layer – insulating layer and insulating layer – substrate interfaces seemed intact even after several loading cycles and uniaxial tensile loading. There was also the right amount of porosity that would not significantly compromise the mechanical integrity of the coating. However, porosity stabilization is needed for efficient resistant changes. This could be achieved by using other thermal spray techniques that would give a less porous and denser coating or carrying out post-deposition processes on the deposited coating. The insulating layer, which was the more compliant of the two coating layers, obviously transferred the load from the substrate efficiently given that it did not fail during the cyclic loading and failed only at high machinal loads during tensile test

- The surface temperature increased to about 90 ^{o}C with a voltage supply of 7 V and current of 5 A. It was concluded that the surface temperature could be drastically reduced by reducing by limiting the current to 1 A and the total power supply to about 7 Watts and it was found that the measurement noise from both the electrical data and strain data were negligible compared to the magnitudes of the electrical voltage and strain values measured.
- It was found that the selected materials, namely alumina, as an electrically insulating layer, the blended nickel alloy, as the sensor, and the silver-filled epoxy were satisfactory for strain sensing objective.
- The deposition of flame spray alumina coating directly on carbon fiber reinforced polymer (CFRP) can be achieved without first depositing a low temperature heat sink on the CFRP.

Chapter 3

Development of Mathematical Models to Predict the Piezoresistive Performance of the Bi-layered Coating-Substrate System

The theoretical study of electromechanical behavior of a coating-substrate system subjected to in-plane electromechanical loading is presented in this chapter. The coating layers represent a piezoresistive layer and a dielectric or insulating layer, both coated on an elastic substrate, forming a bi-layered coating-substrate system with the elastic substrate modelled as an elastic half-plane. Cases for both perfect and imperfect bonding at the coating-substrate interfaces were studied. The imperfect bonding conditions were modelled as edge and central delamination of the insulating layer. The electromechanical behavior of the system was characterized by a piezoresistive-stress constitutive relation and the theoretical postulations for the three bonding conditions – perfect bonding, edge delamination, and central delamination – were formulated in terms of interfacial shear stress. The resulting singular integro-differential equations were solved by using Chebyshev polynomial expansions. Numerical simulation was also conducted to study the effects of aspect ratio of the insulating layer on the coating-substrate system. The analytical models predicted the strain distributions in each coating layer and substrate and define the relationship between them. Likewise, the analytical models predicted the localized shear stress distribution within the coating layers when delamination was present. The results are important for applicability of integrated coating-substrate system to structural health monitoring.

Nomenclature

d	Number of Chebyshev polynomials terms	GF	gauge factor of the piezoresistive layer
d_l	point at the left edge of central delamination (m)	$h^{(i)}$	thickness of the insulating layer (m)
d_r	point at the right edge of central delamination (m)	$h^{(pi)}$	thickness of the piezoresistive layer (m)
$E^{(i)}$	elastic modulus of the insulating layer (Pa)	K_{II}	Mode II stress intensity factor (MPa.m$^{1/2}$)
$E^{(pi)}$	elastic modulus of the piezoresistive layer (Pa)	K_{II}^{L}	mode II stress intensity factor at the left edge of the coating (MPa.m1/2)
$E^{(s)}$	elastic modulus of the substrate (Pa)	K_{II}^{R}	mode II stress intensity factor at the right edge of the coating (MPa.m$^{1/2}$)
e	geometric property of the piezoresistive layer, $e = h^{(pi)} / l$	k	k = 0, 1, 2, ..., N
e_l	geometric property of the delaminated piezoresistive layer, $e_l = h^{(pi)} / l_l$	$\boldsymbol{l}$	half-length of the coating layer (m)
e_r	geometric property of the delaminated piezoresistive layer, $e_r = h^{(pi)} / l_r$	l_l	half-length of the left side of the centrally delaminated coating
f_n	coefficients in Chebyshev polynomial expansions	l_{eff}	effective half-length of the coating after delamination
f_n^l	Coefficients in Chebyshev polynomial expansions for the delaminated coating	l_r	half-length of the coating at the right side of central delamination

f_n^r	Coefficients in Chebyshev polynomial expansions for the delaminated coating	n	Number of Chebyshev polynomials terms
N	number of Chebyshev polynomials terms	R_1	electrical resistance of a precision resistor in the bridge circuit (Ω)
p	property of the piezoresistive layer, $p = \frac{h^{(pi)}(1+2\nu^{(pi)}-GF)}{\alpha l}$ (Pa)	R_2	electrical resistance of a precision resistor in the bridge circuit (Ω)
$\lvert p\rvert$	absolute value of p, $\lvert p\rvert = \left\lvert \frac{h^{(pi)}(1+2\nu^{(pi)}-GF)}{\alpha l} \right\rvert$ (Pa)	R_4	electrical resistance of a precision resistor in the bridge circuit (Ω)
p_l	property of the piezoresistive layer, $p_l = p\frac{e_l}{e}$ (Pa)	Sign	Signum function
p_r	property of the piezoresistive layer, $p_r = p\frac{e_r}{e}$ (Pa)	T_n	Chebyshev polynomials of the first kind
q	property of the insulating layer, $q = \frac{h^{(i)}}{\mu^{(i)} l}$ (/Pa)	t_l	point along (x,0) at the left edge of the coating layer (m)
q_l	property of the piezoresistive layer, $q_l = q\frac{e_l}{e}$ (/Pa)	t_r	point along (x,0) at the right edge of the coating layer (m)
q_r	property of the piezoresistive layer, $q_r = q\frac{e_r}{e}$ (/Pa)	U_n	Chebyshev polynomials of the second kind
R_i	instantaneous electrical resistance of the piezoresistive layer (Ω)	$u_x^{(p)}$	longitudinal displacement within the piezoresistive layer (m)

R_o	electrical resistance of the piezoresistive layer with zero mechanical load (Ω)
u^+	longitudinal displacement at the upper surface of the insulating layer (m)
u^-	longitudinal displacement at the upper surface of the insulating layer (m)
V_g	bridge voltage (V)
V_s	supply voltage (V)
W	characterises the external load applied to the elastic substrate, $W = \varepsilon_x^{(s)}(\pm\infty) / E^{(pi)}$ (/Pa)
x	horizontal coordinate
x_l	horizontal coordinate at the left side of central delamination
x_r	horizontal coordinate at the left side of central delamination
y	vertical coordinate
$u_x^{(s)}$	longitudinal displacement along (m)

Greek symbols

α	piezoresistive coefficient matrix (/Pa)
ε_x	linear strain along *x*-axis
$\varepsilon_x^{(pi)}$	linear strain along *x*-axis in the piezoresistive layer
$\varepsilon_x^{(s)}$	linear strain along x-axis at the surface of the substrate
ε^+	longitudinal strain at the upper surface of the insulating layer
ε^-	longitudinal strain at lower surface of the insulating layer
θ_k	$\theta_k = \frac{k}{N+1}\pi$
λ	normalized point along *x*-axis, $\lambda = x / l$

z Physical property of the substrate, $z = \pi E^{(s)} / 2\left(1 - v^{(s)2}\right)$

λ_k collocation points along *x*-axis, $\lambda_k = \cos\theta_k$

λ_{lk} collocation points along *x*-axis of the left part of the centrally delaminated coating layer, $\lambda_{lk} = \lambda_k$

σ_y axial stress along y-axis (Pa)

λ_{rk} collocation points along *x*-axis of the right part of the centrally delaminated coating layer, $\lambda_{rk} = \lambda_k$

σ^o normalized axial stress within the centrally delaminated part of the coating, $\sigma^o = \dfrac{\sigma_d}{E^{(pi)}}$

λ'_{lk} $\lambda'_{lk} = \dfrac{2e_l}{e} - 1 - \dfrac{e_l}{e_r} + \dfrac{e_l}{e_r}\cos\theta_k$

σ^∞ axial stress along x-axis at both ends of the substrate (Pa)

λ'_{rk} $\lambda'_{rk} = -\dfrac{2e_r}{e} + 1 + \dfrac{e_r}{e_l} + \dfrac{e_r}{e_l}\cos\theta_k$

τ interfacial shear stress (Pa)

λ_l^* $\lambda_l^* = 2e_l\dfrac{e_r - e}{ee_r} - 1$

τ_{xy} interfacial shear stress at *x*-*y* plane (Pa)

λ_r^* $\lambda_r^* = -2e_r\dfrac{e_l - e}{ee_l} + 1$

τ^l interfacial shear stress at the left part of the centrally delaminated coating layer (Pa)

$\mu^{(i)}$ shear modulus of the insulating layer (Pa)

τ^r interfacial shear stress at the right part of the centrally delaminated coating layer (Pa)

$\nu^{(pi)}$	Poisson ratio of the piezoresistive layer	$\bar{\tau}$	normalized interfacial shear stress, $\bar{\tau}(\lambda) = \frac{\tau(l\lambda)}{E^{(pi)}}$
$\nu^{(s)}$	Poisson ratio of the substrate	ϕ	normalized dummy variable, $\phi = \frac{\psi}{l}$
σ_d	axial stress within the centrally delaminated part of the coating (Pa)	ψ	dummy variable

Subscripts

eff	effective	r	left edge of the coating layer
d	delamination length		**Superscript**
II	Mode II	(i)	insulating layer
k	$k = 0, 1, 2, \ldots, N$	L	left edge of the coating layer
l	left edge of the coating layer	(pi)	piezoresistive layer
ψ	dummy variable	R	right edge of the coating layer
N	number of terms for the Chebyshev polynomials	(s)	substrate
n	$n = 0, 1, 2, ..., N$	∞	remote

l	left edge of the coating layer	'	arbitrary designation
ψ	dummy variable	*	arbitrary designation

3.1 Mathematical Formulation

The piezoresistive response of a bi-layered coating-substrate system is strongly influenced by the adhesive shear bonding between the coating and the substrate. The state of the bonding contributes largely to the strain transfer mechanism within the system. In this regard, the analytical model of the coating-substrate system was developed to understand this mechanism. Descriptive examples were presented to show the effect of the interfacial delamination, geometric and material properties on the piezoresistive response of the coating-substrate system.

3.1.1 Perfect bonding in the coating-substrate system

A uniaxial analysis of a bi-layered coating bonded to an isotropic and homogenous elastic substrate modelled as a half-plane was conducted. The half-plane model of the substrate represents the case where the thicknesses of the coating layers are significantly lower than that of the substrate [82, 100 - 102]. The Cartesian coordinate system (*x, y*) was utilized with the origin at the center of the insulating layer-substrate interface and the length of the bi-layered coating was 2*l*. In this model, without affecting the validity of the proof in general, the structure is assumed to have unit width. A mechanical stress, σ^{∞} is applied to the substrate at the surfaces ($\pm\infty$, *y*) shown in Fig. 3-1. The application of the axial stress generates a shear stress, τ as shown in Fig. 3-2. The superscripts '(pi)', '(i)', and '(s)' were used to represent the physical properties of the piezoresistive layer, the insulating layer and the substrate, respectively.

As a result of the structural descriptions of the piezoresistive layer, the following assumptions can be made:

(i) Because of the relatively small thickness of the piezoresistive layer, the axial stress, $\sigma_x^{(pi)}$ and axial displacement, $u_x^{(pi)}$ within it were assumed to be uniformly distributed across the thickness, thus implicitly, approximating their analysis to a 1D problem .

(ii) The interfacial shear stress, τ and interfacial normal stress, σ transferred along the piezoresistive layer – insulating layer will act as distributed body forces for the piezoresistive layer.

(iii) Besides acting as a dielectric/insulating layer, the insulating layer is assumed to have a relatively lower axial elastic modulus compared to its shear modulus and thus, acts as a set of shear springs.

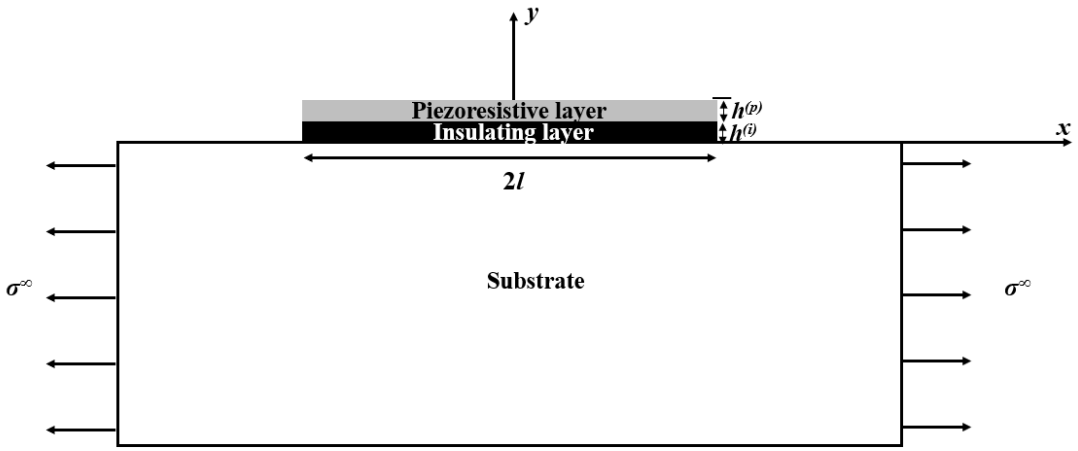

Figure 3-1 Schematic of the loaded coating-substrate system

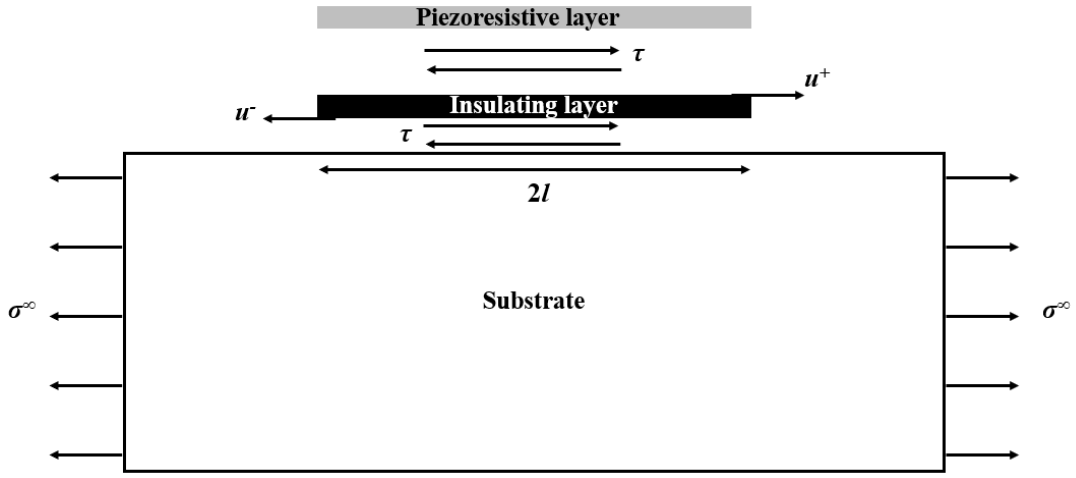

Figure 3-2 Schematic of the free-body diagram showing the shear stresses acting on the layers of the coating-substrate system

Equation(s) of constraints and loads for the piezoresistive layer

Based on the assumptions listed above, the following governing equilibrium equation for the piezoresistive layer can be represented by:

$$\frac{d\sigma_x^{(pi)}(x)}{dx} + \frac{\tau(x)}{h^{(pi)}} = 0 \quad . \tag{3-1}$$

The two ends of the piezoresistive layer are traction free. Hence, the traction free boundary condition is written as:

$$\sigma_x^{(pi)} = 0 \qquad |x| = l \quad . \tag{3-2}$$

From Eq. (3-1), the axial stress can be expressed as the average shear stress within the piezoresistive layer as:

$$\sigma_x^{(pi)}(x) = -\int_{-l}^{x} \frac{\tau(\psi)}{h^{(pi)}} d\psi \quad , \tag{3-3}$$

and applying the traction free boundary condition of Eq. (3-2) to Eq. (3-3) yields:

$$\int_{-l}^{l} \tau(\psi) d\psi = 0 \,. \tag{3-4}$$

A small deformation would therefore result in a relative change in the resistance in this layer according to the following piezoresistive constitutive relation governing the piezoresistive response of the layer is [103-106]:

$$\left(\frac{R_i - R_o}{R_o} \right)^{(pi)} (x) = \varepsilon_x^{(pi)}(x)\left(1 + 2\nu^{(pi)}\right) + \alpha \sigma_x^{(pi)}(x) \,, \tag{3-5}$$

where $\left(\frac{R_i - R_o}{R_o} \right)^{(pi)}$ is the relative electrical resistance change.

Equation (3-5) is predicated on the theory that the relative change in the electrical resistance combines the geometrical influence (first term on the right-hand side) and an influence from the material's intrinsic property (second term on the right-hand side). The intrinsic property is directly related to the material's piezoresistivity.

Substituting Eq. (3-3) into Eq. (3-5) and re-arranging gives the strain field in the piezoresistive layer:

$$\varepsilon_x^{(pi)}(x) = \frac{\alpha}{h^{(pi)}(1 + 2\nu^{(pi)} - GF)} \int_{-l}^{x} \tau(\psi) d\psi \qquad |x| < l \,, \tag{3-6}$$

where the displacement field is given by:

$$u_x^{(pi)}(x) = \frac{\alpha}{h^{(pi)}(1+2\nu^{(pi)} - GF)} \int_{-l}^{x} (x-\psi)\tau(\psi)d\psi \qquad |x| < l\,, \tag{3-7}$$

and

$$GF = \left(\frac{\left(\frac{R_i - R_o}{R_o} \right)^{(pi)}(x)}{\varepsilon_x^{(pi)}(x)} \right). \tag{3-8}$$

Equations (3-6) and (3-7) describe the relationship between the strain and displacement fields in the piezoresistive layer and the interfacial shear stress, τ, respectively. They include the coupled electromechanical and geometric properties of the piezoresistive layer with the only unknown function being τ. The gauge factor (GF) is a measure of sensitivity of the coating layer to changes in strain.

Equation(s) of constraints and loads for the insulating layer

For the insulating layer, its deformation is described by the following constitutive relation:

$$-\tau(x) = \mu^{(i)} \left(\frac{u^{+}(x) - u^{-}(x)}{h^{(i)}} \right), \tag{3-9}$$

where $u^{+}(x)$ and $u^{-}(x)$ represent the longitudinal displacements. Since perfect bonding is assumed within the layers, continuity conditions of the displacements mean they will be continuous across the piezoresistive layer - insulating layer and insulating layer - substrate interfaces [83,107-109]

Hence, $u^{+}(x)$ and $u^{-}(x)$ also represent the longitudinal displacements of the lower surface of the piezoresistive layer and the upper surface of the substrate, respectively. The continuity conditions

are equally applicable to the longitudinal strains, $\varepsilon^{+}(x)$ and $\varepsilon^{-}(x)$ for the lower surface of the piezoresistive layer and the upper surface of the substrate, respectively.

Taking the derivative of Eq. (3-9) with respect to x and re-arranging gives:

$$-\frac{h^{(i)}}{\mu^{(i)}}\frac{d\tau(x)}{dx}=\varepsilon_x^{+}(x)-\varepsilon_x^{-}(x)\,. \tag{3-10}$$

Equation(s) of constraints and loads for the substrate

The boundary conditions for the substrate are:

$$\tau_{xy}^{(s)}(x,0)=\begin{cases}-\tau(x) & (|x|<l)\\ 0 & (|x|>l)\end{cases} \qquad \sigma_y(x,0)=0, \tag{3-11}$$

and

$$\sigma_x^{(s)}(\pm\infty)=\sigma^{\infty}\,. \tag{3-12}$$

The exact solution of a half elastic plane subjected to a concentrated horizontal force [109] was utilized to formulate the strain field , ε_x at the surface (x, 0) of the substrate which gives:

$$\varepsilon_x^{(s)}(x,0)=\varepsilon_x^{(s)}(\pm\infty)-\frac{2\left(1-\nu^{(s)^2}\right)}{\pi E^{(s)}}\int_{-l}^{l}\frac{\tau(\psi)}{x-\psi}d\psi \qquad |x|<l\,, \tag{3-13}$$

with

$$u_x^{(s)}(x,0) = (x+l)\varepsilon_x^{(s)}(\pm\infty) - \frac{2\left(1-\nu^{(s)^2}\right)}{\pi E^{(s)}}\int_{-l}^{x}\int_{-l}^{l}\frac{\tau(\psi)}{x-\psi}d\psi dx \qquad |x| < l\,. \tag{3-14}$$

The strain and displacement fields at the surface of the substrate bonded to the coating layer are described by Eqs. (3-13) and (3-14), respectively. Substituting Eqs. (3-6) and (3-13), which represent strain field in the piezoresistive layer and surface strain field of the substrate, respectively, into Eq. (3-10) gives:

$$\begin{aligned}&\frac{2(1-\nu^{(s)2})}{\pi E^{(s)}E^{(pi)}}\int_{-l}^{l}\frac{\tau(\psi)}{x-\psi}d\psi + \frac{\alpha}{h^{(pi)}E^{(pi)}(1+2\nu^{(pi)}-GF)}\int_{-l}^{x}\tau(\psi)d\psi + \frac{h^{(i)}}{E^{(pi)}\mu^{(i)}}\frac{d\tau(x)}{dx}\\ &= \frac{\varepsilon_x^{(s)}(\pm\infty)}{E^{(pi)}}\end{aligned}\,. \tag{3-15}$$

Equations (3-4) and (3-15) are used to solve for τ. Normalizing τ and x with $E^{(pi)}$ and l as the normalizing constants, respectively and making the equations unitless gives:

$$\left.\begin{aligned}&\int_{-1}^{1}\overline{\tau}(\phi)d\phi = 0\\ &\frac{1}{W}\left(\frac{1}{z}\int_{-1}^{1}\frac{\overline{\tau}(\phi)d\phi}{\lambda-\phi} + \frac{1}{p}\int_{-1}^{\lambda}\overline{\tau}(\phi)d\phi - q\frac{d\overline{\tau}(\lambda)}{d\lambda}\right) = -1 \qquad |\lambda| < 1\end{aligned}\right\}, \tag{3-16}$$

where

$$\left.\begin{aligned}z &= \frac{\pi E^{(s)}}{2(1-\nu^{(s)2})}\\ p &= \frac{h^{(pi)}(1+2\nu^{(pi)}-GF)}{\alpha l}\\ q &= \frac{h^{(i)}}{\mu^{(i)}l}\\ W &= \frac{\varepsilon_x^{(s)}(\pm\infty)}{E^{(pi)}}\\ \lambda &= \frac{x}{l}, \frac{\tau(l\lambda)}{E^{(pi)}} = \overline{\tau}(\lambda)\end{aligned}\right\}. \tag{3-17}$$

For the case where the thickness of the insulating layer approaches zero, Eq. (3-16) reduces to

$$\left.\begin{aligned} &\int_{-1}^{1}\bar{\tau}(\phi)d\phi = 0 \\ &\frac{1}{W}\left(\frac{1}{z}\int_{-1}^{1}\frac{\bar{\tau}(\phi)d\phi}{\lambda-\phi}+\frac{1}{p}\int_{-1}^{\lambda}\bar{\tau}(\phi)d\phi\right) = -1 \qquad |\lambda|<1 \end{aligned}\right\}. \tag{3-18}$$

Thus, Eq. (3-18) represents the equation for a single layer coating-substrate system. The general solution to Eq. (3-16), which is a Volterra-Fredholm singular integro-differential equation, can be expressed in terms of Chebyshev polynomial expansions [82, 101]:

$$\bar{\tau}(\lambda) = \frac{1}{\sqrt{1-\lambda^2}}\sum_{n=0}^{\infty} f_n T_n(\lambda), \tag{3-19}$$

where $T_n(\lambda)$ are Chebyshev polynomials of the first kind. They can be expressed in terms of cosine functions as:

$$T_n(\lambda) = \cos(n\theta), \tag{3-20}$$

and

$$\lambda_k = \cos\theta_k \qquad k = 1, 2, ...\infty. \tag{3-21}$$

If the polynomial expansion converges at $k = N$, then:

$$\lambda_k = \cos\left(\frac{k}{N+1}\right)\pi \qquad k = 1, 2, ...N. \tag{3-22}$$

Based on the properties of Chebyshev polynomials shown in Eq. (A-7) to Eq. (A-9), Eq. (3-16) can be further simplified to:

$$\sum_{n=1}^{N} f_n \frac{\sin(n\theta_k)}{\sin\theta_k}\left(\frac{1}{Wz}\pi + \frac{1}{Wp}\frac{\sin\theta_k}{n} - \frac{q}{W}\left(\frac{n+\cot\theta_k\cot(n\theta_k)}{\sin(\theta_k)}\right)\right) = -1. \quad (3\text{-}23)$$

The coefficients, f_n can be determined from Equation (3-23).

3.1.2 Effects of interfacial delamination on the piezoresistive response of the coating-substrate system

Thermal residual stresses, mechanical stresses, and low bonding strength between the coating and the substrate can all lead to partial or complete delamination of the coating from the substrate. For example, residual stresses can generate high stresses which could be larger than the adhesive strength between the coating and the substrate, thus causing edge delamination of the coating [110]. Also, application of mechanical stress to the system could initiate delamination at the interfaces of the coating layers, subsequently leading to failure of the system. Delamination is a significant threat to an integrated coating-substrate system, hence the analysis on how it affects the piezoresistive response of the system is necessary. This imperfect interfacial condition was represented by two modes of delamination in this work: edge delamination and central delamination of the insulating layer.

A plane strain analysis of the bi-layered coating-substrate system is also done here with the substrate modelled as a half-plane assumed to be isotropic, homogenous, elastic. The loading conditions and the cartesian coordinate system were maintained as used in Section 3.1.1.

Edge delamination of the insulating Layer

When delamination occurs at the edge of the coating, the delaminated region has zero boundary stresses according to this analysis [82]. With this present analytical model, the

delaminated region of the coating will experience no stress and, thus, reduce the effective length of the coating to the bonded part only as shown in Fig. 3-3 [109, 111]. The effective length of the coating layer relative to the perfectly bonded system is $2l_{eff} = 2l - d$, where d is the delamination length. With this formulation, similar analysis conducted for the perfectly bonded system can be employed with the only difference being the respective effective lengths of their coating layers.

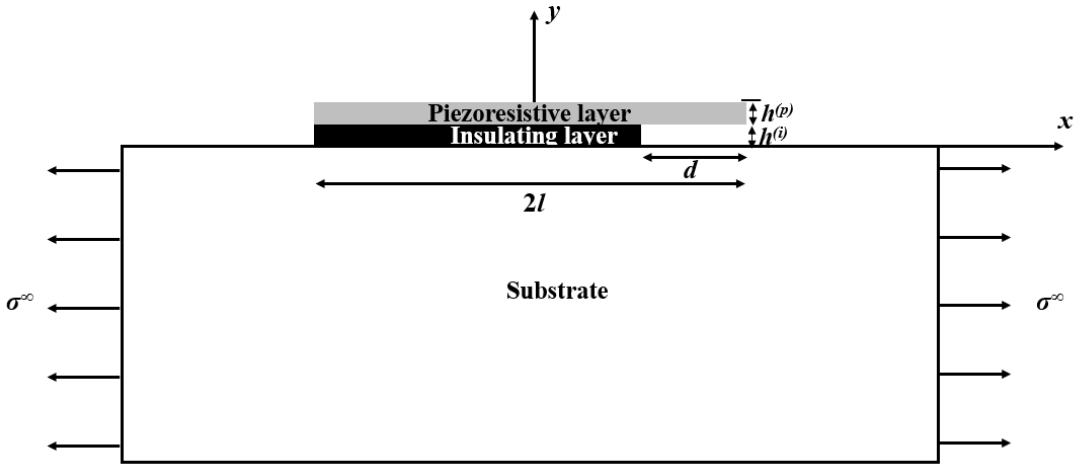

Figure 3-3 Schematic of edge delamination

Central delamination of the insulating layer

Delamination may also occur away from the edges, within the coating as shown in Fig. 3-4. Here, a more rigorous analysis is required for the model describing the piezoresistive response of the coating-substrate system. Consider the piezoresistive layer of length, $2l$, occupying the distance between $t_l < x < t_r$ with the dielectric or insulating layer delaminated from the substrate between $d_l < x < d_r$. The delaminated part of the piezoresistive layer can be regarded as a one-dimensional element subjected to an axial stress, σ_d. In this case, the piezoresistive layer can be viewed as two

"piezoresistive layers" subjected to the axial stress, σ_d at their interior edges as shown in Fig. 3-5 [54, 82]. Therefore, the axial stress, $\sigma_x^{(pi)}(x)$ in the piezoresistive layer can be expressed in terms of the equilibrium equation of Eq. (3-3) and the traction free boundary conditions at the two ends of the coating layer as:

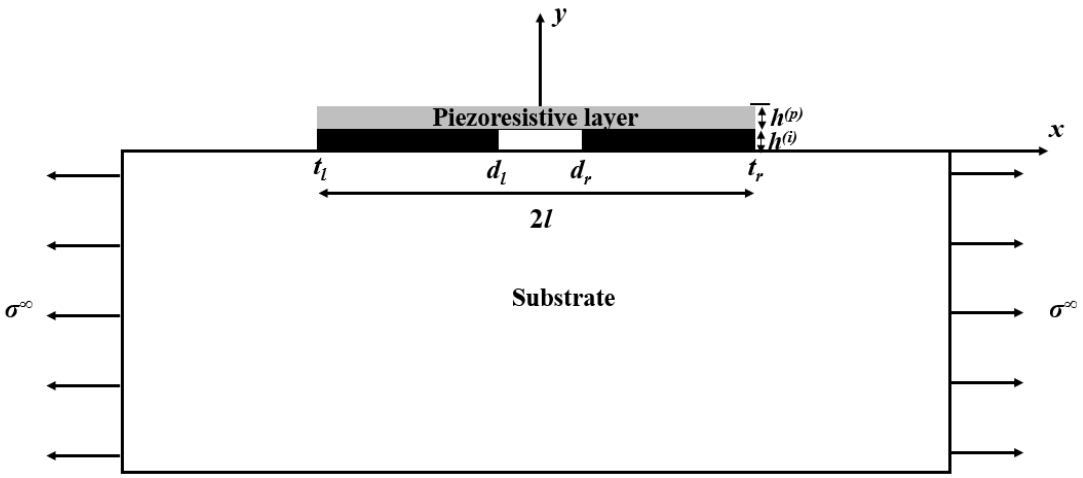

Figure 3-4 Schematic of the coating-substrate system showing the interior delamination.

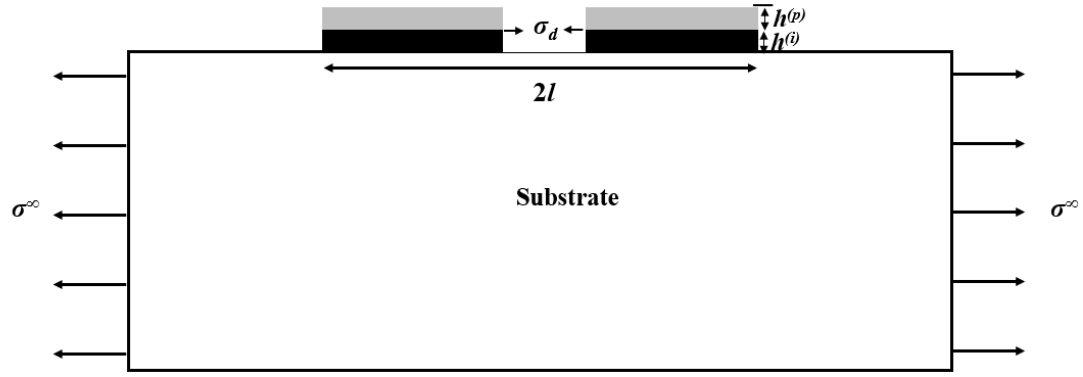

Figure 3-5 Schematic of the coating-substrate system showing the axial stress at the delaminated region represented as a one-dimensional element

$$\sigma_x^{(pi)} = \begin{cases} -\int_{t_l}^{x} \frac{\tau(\psi)}{h^{(pi)}} d\psi & t_l < x < d_l \\ \sigma_d & d_l < x < d_r \\ \sigma_d - \int_{d_r}^{x} \frac{\tau(\psi)}{h^{(pi)}} d\psi & d_r < x < t_r \end{cases}, \tag{3-24}$$

where

$$\sigma_d = -\int_{t_l}^{d_l} \frac{\tau(\psi)}{h^{(pi)}} d\psi = \int_{d_r}^{t_r} \frac{\tau(\psi)}{h^{(pi)}} d\psi \,. \tag{3-25}$$

By substituting Eq. (3-24) into Eq. (3-5), the longitudinal strain can be expressed in terms of the interfacial shear stress, τ as:

$$\varepsilon_x^{(pi)} = \begin{cases} \frac{\alpha}{h^{(pi)}(1+2v^{(pi)} - GF)} \int_{t_l}^{x} \tau(\psi) d\psi & t_l < x < d_l \\ \frac{\alpha\sigma_d}{GF - (1+2v^{(pi)})} & d_l < x < d_r \\ \frac{\alpha}{GF - (1+2v^{(pi)})} \left(\sigma_d - \int_{d_r}^{x} \frac{\tau(\psi)}{h^{(pi)}} d\psi \right) & d_r < x < t_r \end{cases}. \tag{3-26}$$

The coated surface of the substrate is subjected to the following boundary conditions:

$$\tau_{xy}(x,0) = \begin{cases} -\tau(x) & t_l < x < d_l \quad \text{and} \quad d_r < x < t_r \\ 0 & \text{otherwise} \end{cases}. \tag{3-27}$$

By making use of the fundamental solution of a horizontally concentrated force acting on an elastic half-plane [82, 83, 99, 111] the strain on the surface of the substrate can be expressed as:

$$\varepsilon_x^{(s)}(x,0) = \varepsilon_x^{(s)}(\pm\infty) - \frac{2(1-v^{(s)2})}{\pi E^{(s)}} \left[\int_{t_l}^{d_l} \frac{\tau(\psi)}{x-\psi} d\psi + \int_{d_r}^{t_r} \frac{\tau(\psi)}{x-\psi} d\psi \right]. \tag{3-28}$$

Also, by considering the constitutive relation of the dielectric or insulating layer in Eq. (3-10), the relationship between the strain in the piezoresistive and the insulating layers can be expressed as:

$$\varepsilon_x^{(pi)} - \varepsilon_x^{(s)} = -\frac{h^{(i)}}{\mu^{(i)}}\frac{d\tau(x)}{dx} \qquad t_l < x < d_l \quad , \quad d_r < x < t_r \quad , \quad y = 0 \quad . \tag{3-29}$$

By substituting Eqs. (3-26) and (3-28) in (3-29) and re-arranging:

$$\frac{2(1-v^{(s)2})}{\pi E^{(s)}}\int_{t_l}^{d_l}\frac{\tau(\psi)}{h^{(pi)}}d\psi + \frac{2(1-v^{(s)2})}{\pi E^{(s)}}\int_{d_r}^{t_r}\frac{\tau(\psi)}{h^{(pi)}}d\psi + \frac{h^{(i)}}{\mu^{(i)}}\frac{d\tau(x)}{dx}$$
$$+\begin{cases}\dfrac{\alpha}{h^{(pi)}(1+2v^{(pi)}-GF)}\displaystyle\int_{t_l}^{x}\tau(\psi)d\psi = \varepsilon_x^{(s)}(\pm\infty) & t_l < x < d_l \quad , \\ \dfrac{\alpha}{h^{(pi)}(1+2v^{(pi)}-GF)}\displaystyle\int_{d_r}^{x}\tau(\psi)d\psi = \varepsilon_x^{(s)}(\pm\infty) + \dfrac{\alpha\sigma_d}{h^{(pi)}(1+2v^{(pi)}-GF)} & d_r < x < t_r \end{cases} . \tag{3-30}$$

By considering deformation of the delaminated region, the axial stress, σ_d in Eq. (3-31) can be determined from Eq. (3-9) thus,

$$u_x^{(pi)}(d_r) - u_x^{(pi)}(d_l) = u_x^{(s)}(d_r) - u_x^{(s)}(d_l) - \frac{h^{(i)}}{\mu^{(i)}}\left(\tau(d_r) - \tau(d_l)\right). \tag{3-31}$$

Integrating Eqs. (3-26) and (3-28), we have

$$u_x^{(pi)}(d_r) - u_x^{(pi)}(d_l) = \frac{\sigma_d\alpha}{GF - (1+2v^{(pi)})}\left(d_r - d_l\right), \tag{3-32}$$

and

$$u_x^{(s)}(d_r) - u_x^{(s)}(d_l) = \varepsilon_x^{(s)}(\pm\infty)\left(d_r - d_l\right) - \frac{2(1-v^{(s)2})}{\pi E^{(s)}}\int_{d_l}^{d_r}\left[\int_{t_l}^{d_l}\frac{\tau(\psi)}{x-\psi} + \int_{d_r}^{t_r}\frac{\tau(\psi)}{x-\psi}\right]dx \, . \tag{3-33}$$

Substituting Eqs (3-32) and (3-33) in (3-31) gives:

$$\frac{2(1-v^{(s)2})}{\pi E^{(s)}}\int_{d_l}^{d_r}\left[\int_{t_l}^{d_l}\frac{\tau(\psi)}{x-\psi} + \int_{d_r}^{t_r}\frac{\tau(\psi)}{x-\psi}\right]dx - \frac{h^{(i)}}{\mu^{(i)}}\left(\tau(d_l) - \tau(d_r)\right)$$
$$= \left(\varepsilon_x^{(s)}(\pm\infty) + \frac{\sigma_d\alpha}{(1+2v^{(p)}) - GF}\right)\left(d_r - d_l\right) \tag{3-34}$$

If both interfacial shear stress, τ and the axial stress at the delaminated part, σ_d are both normalized with $E^{(pi)}$, then Eqs. (3-25), (3-30), and (3-34) become unitless and will give Eqs. (3-35) to (3-38):

$$\int_{-1}^{1} \tau^{l}(\phi) d\phi = -\sigma^{o} e_{l}, \tag{3-35}$$

$$\int_{-1}^{1} \tau^{r}(\phi) d\phi = \sigma^{o} e_{r}, \tag{3-36}$$

$$\frac{1}{W}\left[\frac{1}{z}\int_{-1}^{1}\frac{\tau^{l}(\phi)}{\lambda_{l}-\phi}d\phi+\frac{1}{z}\int_{-1}^{1}\frac{\tau^{r}(\phi)}{\lambda_{r}-\phi}d\phi\right]+\begin{cases}\dfrac{1}{W}\left[q_{l}\dfrac{d\tau^{l}(\lambda_{l})}{d\lambda_{l}}+\dfrac{1}{p_{l}}\int_{-1}^{\lambda_{l}}\tau(\psi)d\psi\right]=-1 & \left|\lambda_{l}\right|<1\\ \dfrac{1}{W}\left[q_{r}\dfrac{d\tau^{r}(\lambda_{r})}{d\lambda_{r}}-\dfrac{1}{p_{r}}\int_{\lambda_{r}}^{1}\tau(\psi)d\psi\right]=-1 & \left|\lambda_{r}\right|<1\end{cases}, \text{ and} \tag{3-37}$$

$$\begin{aligned}&\frac{1}{ze_{l}}\int_{1}^{\lambda_{l}^{*}}\int_{-1}^{1}\frac{\tau^{l}(\phi)d\phi}{\lambda_{l}-\phi}d\lambda_{l}+\frac{1}{ze_{r}}\int_{\lambda_{r}^{*}}^{-1}\int_{-1}^{1}\frac{\tau^{r}(\phi)d\phi}{\lambda_{r}-\phi}d\lambda_{r}-\frac{q_{l}}{e_{l}}\tau^{l}(1)-\frac{q_{r}}{e_{r}}\tau^{r}(-1)\\ &=\left(W+\sigma^{o}pe\right)\left(\frac{2}{e}-\frac{2}{e_{r}}-\frac{2}{e_{l}}\right)\end{aligned}, \tag{3-38}$$

where

$$\tau^{l}(\lambda_{l})=\frac{\tau(l_{l}\lambda_{l}+x_{l})}{E^{(pi)}},\quad \tau^{l}(\lambda_{r})=\frac{\tau(l_{r}\lambda_{r}+x_{r})}{E^{(pi)}},\quad \sigma^{o}=\frac{\sigma_{d}}{E^{(pi)}}, \tag{3-39}$$

with

$$\left.\begin{aligned}
&\lambda_l = \frac{x - x_l}{l_l}, \qquad \lambda_r = \frac{x - x_r}{l_r} \\
&e = \frac{h^{(pi)}}{l}, \qquad e_l = \frac{h^{(pi)}}{l_l}, \qquad e_r = \frac{h^{(pi)}}{l_r} \\
&p_l = p\frac{e_r}{e}, \qquad p_r = \frac{e_l}{e} \\
&q_l = q\frac{e_l}{e}, \qquad q_r = q\frac{e_r}{e} \\
&l = \frac{1}{2}(t_r - t_l), \qquad l_l = \frac{1}{2}(d_l - t_l), \qquad l_r = \frac{1}{2}(t_r - d_r) \\
&x_l = \frac{1}{2}(d_l + t_l), \qquad x_r = \frac{1}{2}(t_r + d_r) \\
&\lambda_l^* = 2e_l\frac{e_r - e}{ee_r} - 1, \qquad \lambda_r^* = -2e_r\frac{e_l - e}{ee_l} + 1
\end{aligned}\right\}. \tag{3-40}$$

The general solutions of τ^l and τ^r in Eqs. (3-39) – (3-42) can then be expressed in terms of Chebyshev polynomial expansions:

$$\tau^l(\lambda_l) = \frac{1}{\sqrt{1-\lambda_l^2}}\sum_{n=0}^{\infty} f_n^l T_n(\lambda_l), \qquad \tau^r(\lambda_r) = \frac{1}{\sqrt{1-\lambda_r^2}}\sum_{n=0}^{\infty} f_n^r T_n(\lambda_r) \tag{3-41}$$

If the polynomial converges at $k = N$, then:

$$\lambda_{lk} = \lambda_{rk} = \lambda_k = \cos\theta_k = \cos\left(\frac{k}{N+1}\pi\right), \qquad k = 1, 2, .., N \tag{3-42}$$

By making use of the properties of Chebyshev polynomials in Eq. (A-7) to (A-9) in the Appendix, Eqs. (3-43) and (3-44) can be further simplified as:

$$\sum_{n=1}^{N} f_n^l \frac{\sin(n\theta_k)}{W\sin\theta_k}\left[\frac{1}{z}\pi+\frac{1}{p_l}\frac{\sin\theta_k}{n}-q_l\left(\frac{n+\cot\theta_k+\cot(n\theta_k)}{\sin(\theta_k)}\right)\right]$$
$$-\sum_{n=1}^{N} f_n^r \frac{\pi\left(\lambda_{rk}^{'}-\mathrm{sign}(\lambda_{rk}^{'})\sqrt{(\lambda_{rk}^{'})^2-1}\right)^n}{Wz\left(\mathrm{sign}(\lambda_{rk}^{'})\sqrt{(\lambda_{rk}^{'})^2-1}\right)} \quad , \tag{3-43}$$
$$\frac{-\sigma^o}{W}\left[\frac{e_r}{z\left(\mathrm{sign}(\lambda_{rk}^{'})\sqrt{(\lambda_{rk}^{'})^2-1}\right)}-\frac{e_l}{p_l\pi}(\pi-\theta_k)-\frac{q_l e_l}{\pi}\left(\frac{\cot\theta_k}{\sin^2\theta_k}\right)\right]=-1$$

$$\sum_{n=1}^{N} f_n^r \frac{\sin(n\theta_k)}{W\sin\theta_k}\left[\frac{1}{z}\pi+\frac{1}{p_r}\frac{\sin\theta_k}{n}-q_r\left(\frac{n+\cot\theta_k+\cot(n\theta_k)}{\sin(\theta_k)}\right)\right]$$
$$-\sum_{n=1}^{N} f_n^l \frac{\pi\left(\lambda_{lk}^{'}-\mathrm{sign}(\lambda_{lk}^{'})\sqrt{(\lambda_{lk}^{'})^2-1}\right)^n}{Wz\left(\mathrm{sign}(\lambda_{lk}^{'})\sqrt{(\lambda_{lk}^{'})^2-1}\right)} \quad , \tag{3-44}$$
$$+\frac{\sigma^o}{W}\left[\frac{e_l}{z\left(\mathrm{sign}(\lambda_{lk}^{'})\sqrt{(\lambda_{lk}^{'})^2-1}\right)}+\frac{e_r}{p_r\pi}\theta_k-\frac{q_r e_r}{\pi}\left(\frac{\cot\theta_k}{\sin^2\theta_k}\right)\right]=-1$$

$$-\sigma^{o}\left[\frac{1}{z}\ln\left|\lambda_l^{*}+\sqrt{(\lambda_l^{*})^2-1}\right|-\frac{1}{z}\ln\left|-\lambda_r^{*}-\sqrt{(\lambda_r^{*})^2-1}\right|+\frac{q_r-q_l}{\pi\sin\left(\frac{\theta_k}{k}\right)}+2pe\left(\frac{1}{e}-\frac{1}{e_r}-\frac{1}{e_l}\right)\right]$$

$$+\sum_{n=1}^{N}f_n^{l}\left(\frac{\pi}{ze_l}\int_1^{\lambda_l^{*}}\frac{\left(\lambda_{lk}^{'}-\mathrm{sign}(\lambda_{lk}^{'})\sqrt{(\lambda_{lk}^{'})^2-1}\right)^{n}}{\left(\mathrm{sign}(\lambda_{lk}^{'})\sqrt{(\lambda_{lk}^{'})^2-1}\right)}d\lambda_{lk}^{'}-\frac{q_l}{e_l}\frac{\cos\left(n\frac{\theta_k}{k}\right)}{\sin\left(\frac{\theta_k}{k}\right)}\right) \qquad . \qquad (3\text{-}45)$$

$$+\sum_{n=1}^{N}f_n^{r}\left(\frac{\pi}{ze_r}\int_1^{\lambda_r^{*}}\frac{\left(\lambda_{rk}^{'}-\mathrm{sign}(\lambda_{rk}^{'})\sqrt{(\lambda_{rk}^{'})^2-1}\right)^{n}}{\left(\mathrm{sign}(\lambda_{rk}^{'})\sqrt{(\lambda_{rk}^{'})^2-1}\right)}d\lambda_{rk}^{'}-\frac{q_r}{e_r}\frac{(-1)^{n}\cos\left(n\frac{\theta_k}{k}\right)}{\sin\left(\frac{\theta_k}{k}\right)}\right)$$

$$=\frac{2}{w}\left(\frac{1}{e}-\frac{1}{e_r}-\frac{1}{e_l}\right) \quad ,$$

where

$$\lambda_{lk}^{'}=\frac{2e_l}{e}-1-\frac{e_l}{e_r}+\frac{e_l}{e_r}\cos\theta_k, \qquad (3\text{-}46)$$

and

$$\lambda_{rk}^{'}=-\frac{2e_r}{e}+1+\frac{e_r}{e_l}+\frac{e_r}{e_l}\cos\theta_k. \qquad (3\text{-}47)$$

3.2 Results and Discussion

3.2.1 Perfect bonding in the coating-substrate system

Numerical simulation

The numerical simulation was conducted with ANSYS APDL software, which has the capability to solve electromechanical analysis problems. In the ANSYS APDL software, the structural and electrical fields are coupled by means of the piezoresistive coefficients. Since this analysis is static, the piezoresistive coating was characterized by structural elasticity, piezoresistive coupling, and electrical resistivity. A dynamic analysis will involve different properties of the piezoresistive layer.

Plane 223 element type was assigned to the piezoresistive layer. It is a 2-D, 8-node coupled-field solid with 4-degrees of freedom: temperature, voltage, and vertical and horizontal displacements. Its capability includes piezoresistive, electroelastic and piezoelectric functionalities. Plane 183 element type, which was assigned to both the insulating layer and the substrate, is a 2-D, 8-node structural solid with 2 degrees of freedom: vertical and horizontal displacements. The electrical resistors were modelled with Circu124. The circuit bridge was modelled so that with zero mechanical load on the substrate, the bridge voltage was zero. After assigning these element types, a mesh quality assessment was conducted through optimization based on the geometry under consideration, the element types used, the type of mesh created, and the dimension of the meshing command. The meshes were refined at the interfaces and for the coating layers for more accuracy. The finite element representation of the electromechanical set-up is shown in Fig. 3-6.

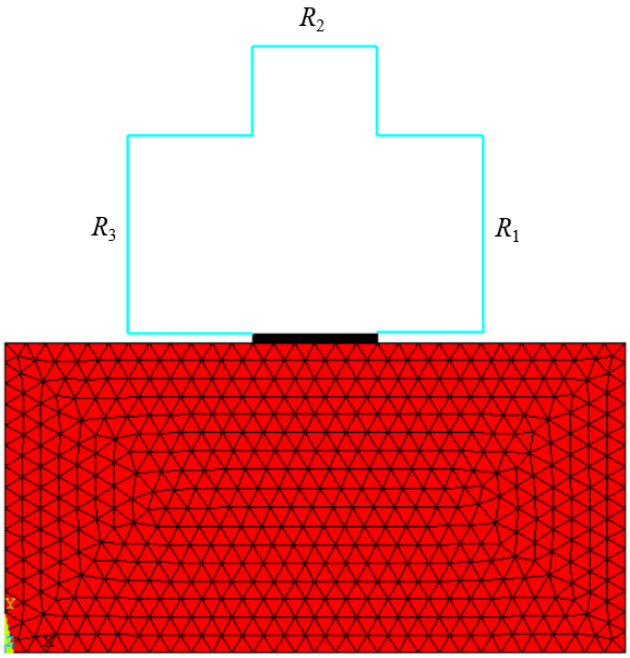

Figure 3-6 The meshed finite-element model

The influence of physical properties, *p, q,* and *z*, of the bi-layered coating-substrate system on the piezoresistive behavior of the integrated system is presented in this section. As shown in Eq. (3-17), $|p|$ is inversely proportional to the aspect ratio of the piezoresistive layer, $\left(l / h^{(pi)}\right)$. Similarly, for a constant $\mu^{(i)}$, q is inversely proportional to the aspect ratio of the insulating layer, $\left(l / h^{(i)}\right)$. Since both coating layers were modelled as the same length in this study, only the thicknesses of the layers were varied to influence the aspect ratio. Finally, for a constant $v^{(s)}$, z is directly proportional to elastic modulus of the substrate, $E^{(s)}$. These three physical properties: *p, q,* and *z* are the responses to $W = \varepsilon_x^{(s)}\left(\pm\infty\right) / E^{(pi)}$ applied to the substrate. The convergence solution for all the cases studied was conducted after generating 28 Chebyshev polynomial terms,

which corresponds to an asymptotic value of 1% difference between each value of stress determined after successive computations.

Also, a careful examination of Eq. (3-17) shows that *p, q,* and *z* represent the combination of geometric and material properties for the piezoresistive layer, insulating layer and the substrate, respectively. Therefore, discussions are centered around how these physical properties affect the interfacial shear stress field which have been shown in Eq. (3-16) to influence the piezoresistive response of the system.

Figure 3-7 shows the typical local shear stress distributions of a bi-layered coating-substrate system for the following physical properties: $|p| = 6.13 \times 10^{9}$ Pa, $z = 3.37 \times 10^{11}$ Pa, $q = 4.96 \times 10^{-13}$ /Pa and $W = 2.76 \times 10^{-14}$ /Pa for both the analytical model and numerical simulation. The normalized interfacial shear stress, $\overline{\tau}$ also represents load transfer from the substrate to the piezoresistive layer. The values of these physical properties (p, z and q) in the foregoing are representative of a piezoresistive layer having a thickness of 0.2 mm, the substrate having an elastic modulus of 200,000 MPa and the insulating layer having a thickness of 0.1 mm, respectively. The other parameters in their respective mathematical descriptions in Eq. (3-17) are kept constant (Table 1). The materials used for the simulation are nickel alloy coating, Al_2O_3 and steel as the piezoresistive layer, dielectric/insulating layer and substrate, respectively. The effective material properties shown in Table 3-1 [110, 112, 113] were used in the simulation of the mechanically loaded coating-substrate system.

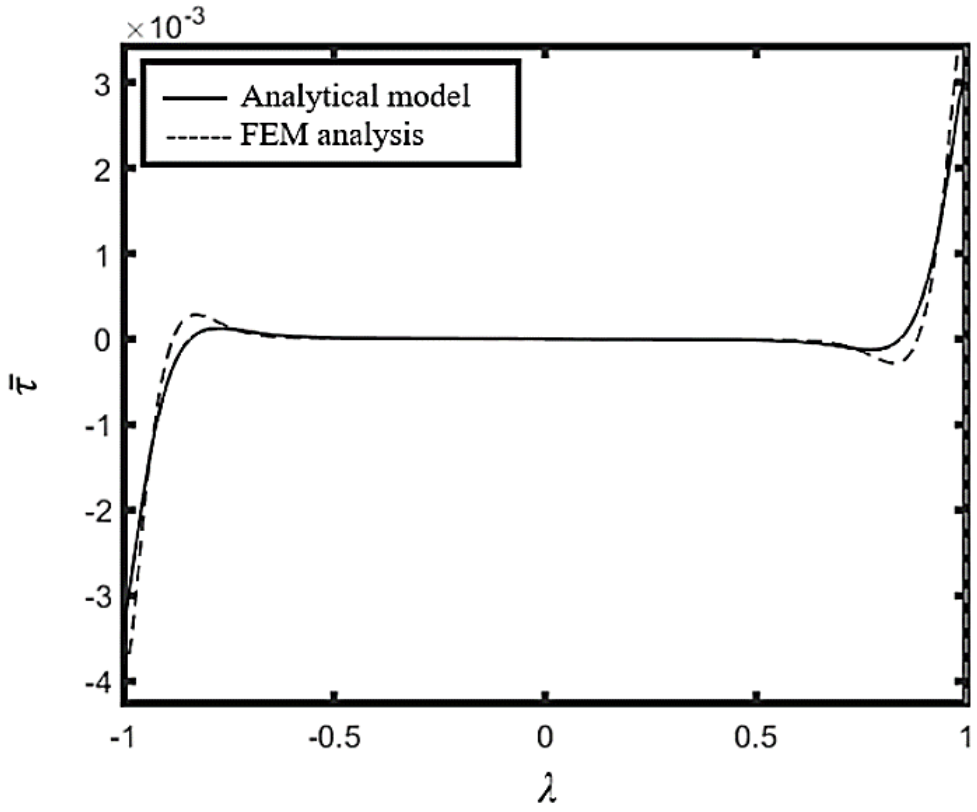

Figure 3-7 Comparison of the normalized interfacial shear stress versus normalized location obtained from the analytical model and numerical simulation.

Table 3-1 Material properties of components in the integrated system

Piezoresistive layer	
Young's modulus, $E^{(pi)}$ (Pa)	1.80×10^{11}
Poisson ratio, $v^{(pi)}$	0.26
Gauge factor, GF	10
Insulating layer	
Young's modulus, $E^{(i)}$ (Pa)	5.0×10^{10}
Poisson ratio, $v^{(i)}$	0.24
Substrate	
Young's modulus, $E^{(s)}$ (Pa)	2.0×10^{11}
Poisson ratio, $v^{(s)}$	0.3

This slight deviation of the analytical model results and the numerical simulation shown in Fig. 3-7 is due to the approach in the stress calculation for both studies; while a 1-D model stress distribution is assumed by the analytical model, a 2-D one was used in the ANSYS APDL analysis.

Figure 3-8 shows the effect of varying $|p|$ for q = 3.31 x 10^{-13} /Pa, z = 3.37 x 10^{11} Pa and W = 2.76 x 10^{-14} /Pa on the normalized shear stress, $\bar{\tau}$. Since the shear distribution is anti-symmetrical about $x = 0$, the shear stress distributions along only half of the piezoresistive layer are presented in this study. The shear stress distribution for the cases seems to have a tension nature between $0.6 < \lambda < 0.85$. This is more obvious at higher values of $|p|$ (inset of Fig. 3-8). For $\lambda > 0.85$, the coating shear stresses is compressive in nature for all cases and increases with $|p|$ (upper right inset in Fig. 3-8). These stresses become concentrated as λ tends to 1 for all the cases. The stress concentration is indicated by the approach of the slopes to infinity for $\lambda > 0.85$. This means increasing the thickness of the piezoresistive layer based on the loading conditions increases the vulnerability of the coating to edge delamination. This is similar to the study by Jin and Wang [82] on electromechanical behaviour of surface-bonded piezoelectric actuators.

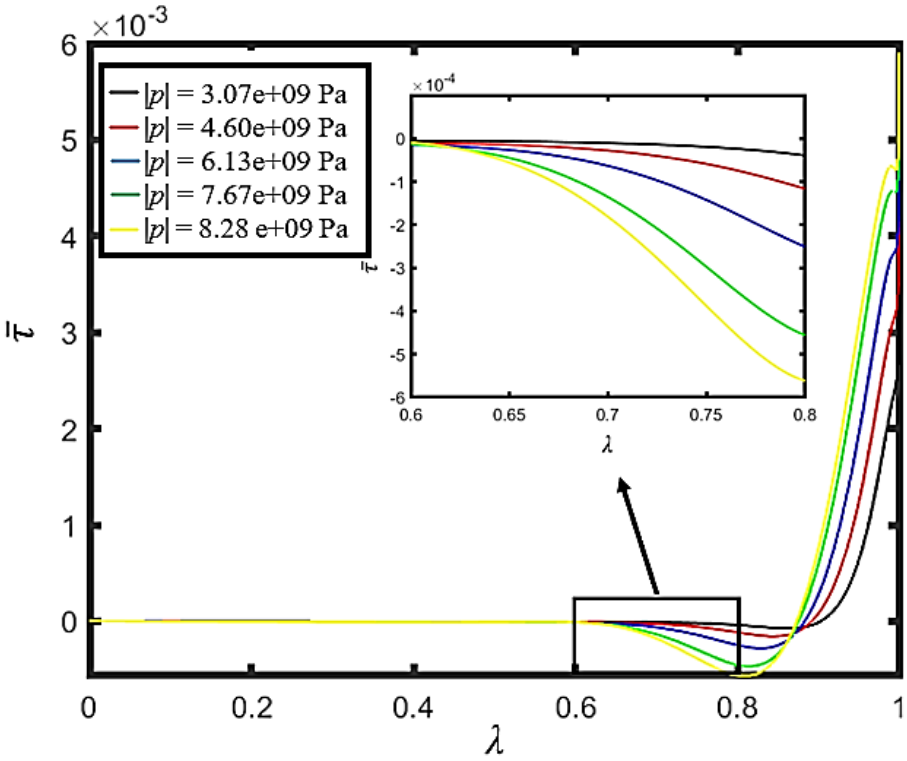

Figure 3-8 Interfacial stress distribution plot for the varying property, $|p|$ of the piezoresistive layer

Figure 3-9 shows the influence of varying q for $|p| = 6133$, $z = 336940$ and $W = 2.76 \times 10^{-14}$ /Pa on the normalized shear stress, $\bar{\tau}$ .The stresses away from the edges of the coating layer become increasingly tensile as q decreases as indicated by the portion of the graph at $0 < \lambda < 0.85$ (inset in Fig. 3-9). After this, the stresses become more compressive and concentrated as q decreases. Close to the edges ($\lambda > 0.85$), the stresses continue to be more concentrated with decreasing q as indicated by the decreasing slope of the curve after $\lambda > 0.85$. This indicates that based on these loading conditions, an insulating layer with low aspect ratio reduces the risk of delamination at the edges.

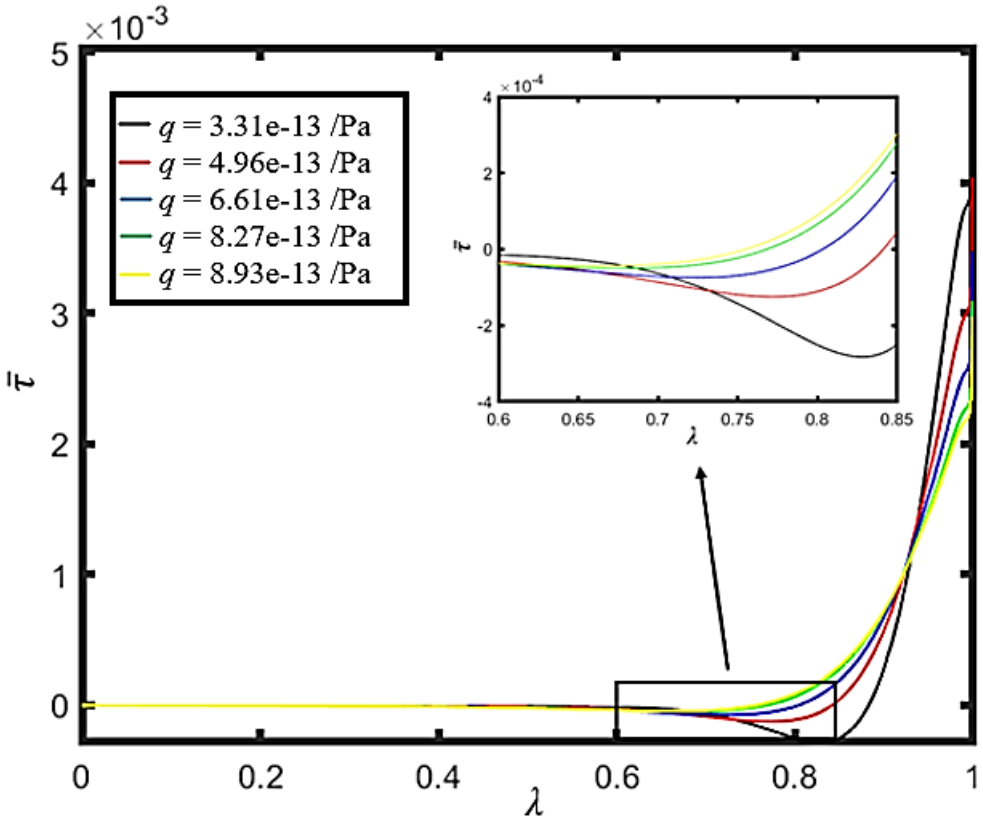

Figure 3-9 Interfacial stress distribution plot for the varying property, q of the insulating layer

The physical property of the substrate, represented by z was also studied to observe its effect on the piezoresistive response through the interfacial shear stress for $|p|= 6.13 \times 10^{9}$ Pa, $q = 3.31 \times 10^{-13}$ /Pa and $W = 2.76 \times 10^{-14}$ /Pa. It was found that the more elastic the substrate is, the lower the stress at the edges of the coating as shown in the top right inset of Fig. 3-10. Therefore, the more elastic substrate has a similar effect as introducing an insulating layer to the integrated structure but the changes to the shear stress are limited for the range of z studied.

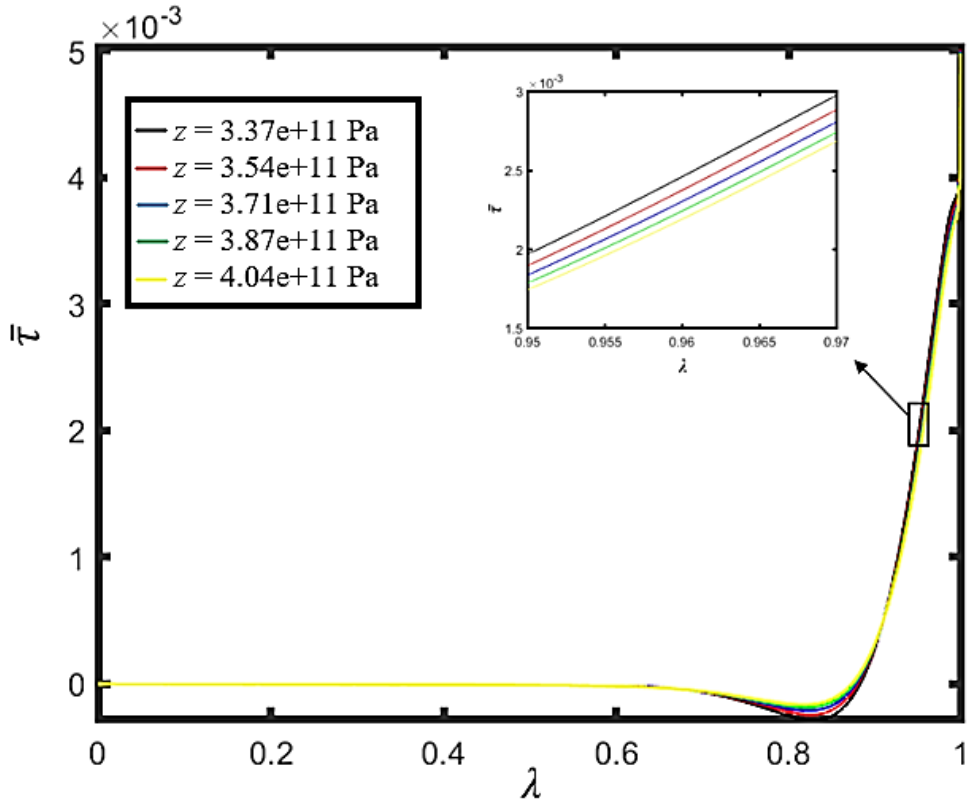

Figure 3-10 Interfacial stress distribution plot for the varying property, z of the substrate

3.2.2 Effects of interfacial delamination on the coating-substrate System

Edge delamination

As discussed previously, a large part of the stress transfers from the substrate happens through the coating edges, thus foreshadowing one of the reasons for edge delamination. The effective length of the delaminated piezoresistive layer at the edge is $2l_{eff} = 2l\text{-}d$. Fig. 3-11 describes the influence of physical property, q of the insulating layer on the normalized shear stress, $\bar{\tau}$ at the edge point $\lambda_e = x/l = -1$ as function of d/l for $|p| = 6.13 \times 10^9$ Pa, $z = 3.37 \times 10^{11}$ Pa and $W = 2.76 \times 10^{-14}$ /Pa. For all the cases of q studied, the figure shows that the edge stresses decrease as

the delamination length increases thus reducing the piezoresistive response. When edge stresses decrease to values below the interfacial bonding, delamination stops developing and this is referred to as the self-arresting mechanism [99]. It can be observed in Fig. 3-11 that increasing the thickness of the insulating layer (as q increases) has more influence on the self-arresting mechanism because q decreases the edge stresses.

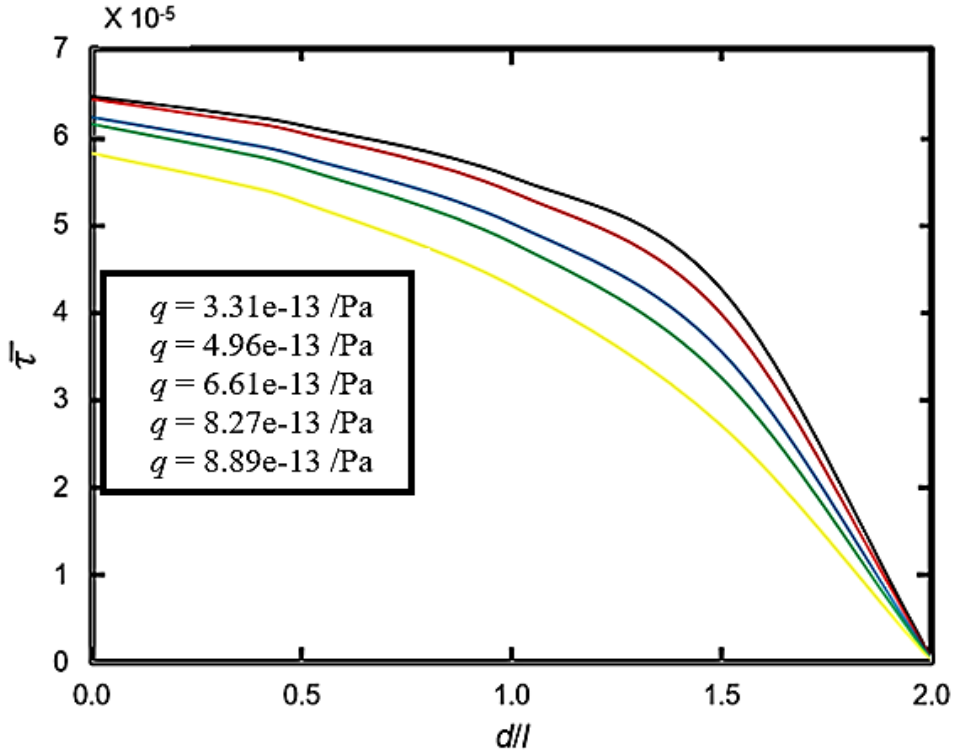

Figure 3-11 Interfacial stress distribution plot at edge $\lambda = -1$ as a function of d/l

Central delamination

For this problem formulation, the piezoresistive layer was assumed to be symmetrically delaminated in $|x| < d$ which means $t_r = -t_l$ and $d_r = -d_l = d$. In this case, the effective length of the piezoresistive layer, $2l_{eff}$ is reduced to 2(l-d). Figure 3-12 shows the shear stress distribution along the piezoresistive layer against the central delamination with the normalized delamination lengths varied from d/l = 0 to 0.9. There is stress concentration around the delaminated edges for the centrally delaminated cases considered. However, it is interesting to observe that the shear stress distribution within the coating layer does not increase significantly until the delamination length is close to 80% of l. This can be observed in Fig. 3-12 as the variation in the minimum points for all the cases. The minimum point increases with delamination length.

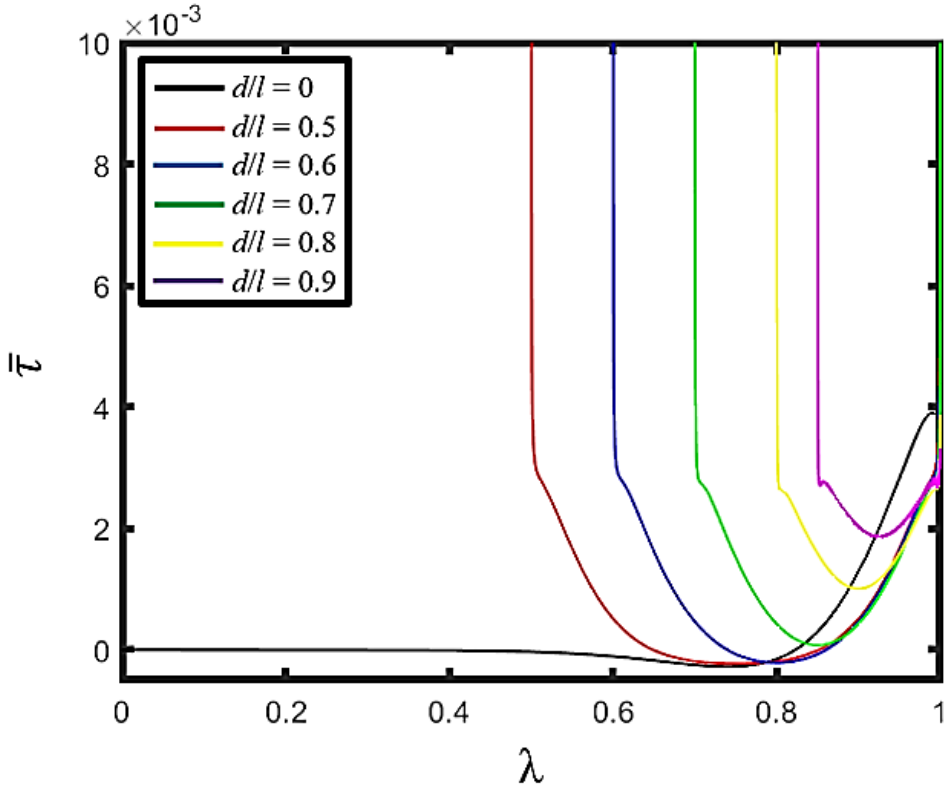

Figure 3-12 Interfacial stress distribution plot at varying interior delamination lengths

The influence of the insulating thickness on the stress distribution at a particular delamination length was also studied. Figure 11 shows the result for the shear stress distribution at $d/l = 0.6$ for different q of the insulating layer at $|p| = 6.13 \times 10^9$ Pa, $z = 3.37 \times 10^{11}$ Pa and $W = 2.76 \times 10^{-14}$ /Pa. It can be seen in the inset of Fig. 3-13 that the stresses at the edges are redistributed (slopes become less steep) as the thickness of the insulating layer increases; the stress concentration reduces with aspect ratio of the insulating layer. This supports the theory stated earlier that introducing the insulating layer lowers the stress concentration at the edges of the coating.

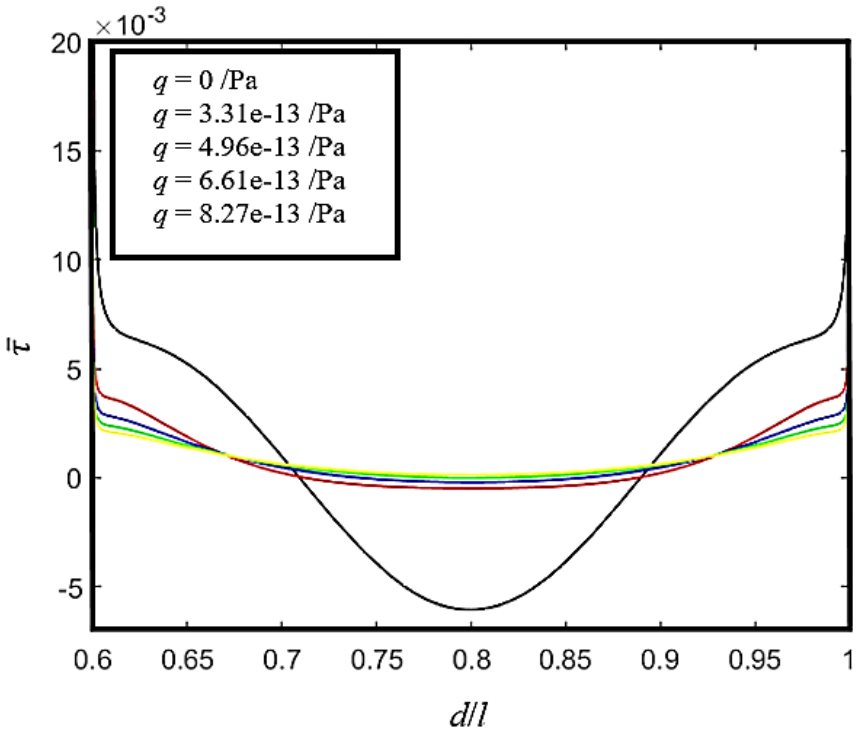

Figure 3-13 Interfacial stress distribution plot for $d/l = 0.6$ at varying q

The study was also done on how the normalized axial stress, σ^o for the delaminated part of the piezoresistive layer was influenced by different lengths of the central delamination at different q of the insulating layer for $|p| = 6.13 \times 10^9$ Pa, $z = 3.37 \times 10^{11}$ Pa and $W = 2.76 \times 10^{-14}$ /Pa (Fig. 3-

14). In all cases, the axial stress reduces with the delamination length. It is interesting to observe that the thickness of the insulating layer has little effect on axial stress within the delaminated length when the length is above 20% of the total coating length ($d/l > 0.2$).

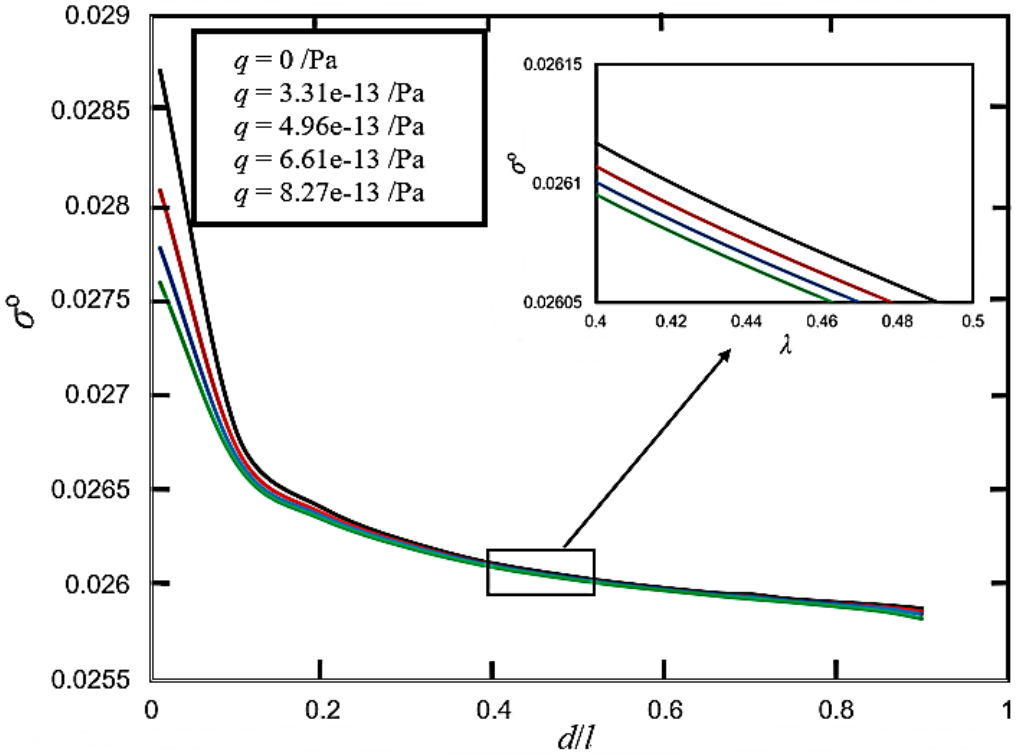

Figure 3-14 Axial stress plot against d/l for different q

3.3 Conclusions

The functionality of a bi-layered coating-substrate system as a damage detection sensor strongly relies on the bonding condition within the system. This bonding condition, in the form of adhesive shear stresses strongly controls the strain transfer mechanisms within the bi-layered system. In this regard, this Chapter focused on modelling this shear stresses to predict the piezoresistive response of a coating-substrate system. Without loss of generality, the system was assumed to be a unit width for a simpler analysis and the coating layers assumed to be several orders of magnitude thinner than the substrate, hence, the substrate was modelled as an elastic, isotropic and homogenous half-plane. The analysis was also extended to imperfect bonding conditions within the system in the form of edge and central delamination. At the end of the analysis, it was found that material and geometric properties of the coating layers and the substrate largely influence the strain transfer from the substrate to the piezoresistive layer. The introduction of an insulating layer reduces the stress concentration at the edges of the coating and the axial stress distribution at the centrally delaminated part of the piezoresistive layer. It also influences the self-arrest mechanism (it reduces the tendency for edge delamination to continue growing). It has little effect on axial stress within the delaminated length when the length is above 20% of the total coating length but significant when the delaminated length is otherwise. Overall, the model can predict the piezoresistive behaviour of an integrated coating-substrate system under perfect and imperfect bonding conditions. Further analysis could be done to include the effect of bending on this behaviour. The study could also be improved to predict piezoresistive performance of the integrated system in mechanically dynamic environment.

Chapter 4

Development of Mathematical Models to Predict the Piezoresistive Performance of the Bi-layered Coating-substrate System with Bending Effects

The theoretical study of electromechanical behavior of a coating-substrate system subjected to in-plane electromechanical loading with bending effects in the coating layers is presented in this chapter. The coating layers represent a piezoresistive layer and a dielectric or insulating layer, both coated on an elastic substrate, forming a bi-layered coating-substrate system with the elastic substrate modelled as an elastic half-plane. Cases for both perfect and imperfect bonding at the coating-substrate interfaces were studied. The imperfect bonding condition was modelled as a central delamination of the insulating layer with the electromechanical behavior of the system characterized by a piezoresistive-stress constitutive relation. The theoretical postulation for the problem was formulated in terms of interfacial shear and interfacial normal stresses. The resulting singular integro-differential equations were solved by using Chebyshev polynomial expansions. The analytical models predicted the strain distributions in each coating layer and substrate and define the relationship between them. Likewise, the analytical models predicted the localized shear and normal stress distribution within the coating layers when delamination was present. The results are important for applicability of an integrated coating-substrate system in damage detection.

Nomenclature

A	$A = E^{(pi)}\left(1-2v^{(s)}\right)\left(1+v^{(s)}\right)/E^{(s)}$	e	geometric property of the piezoresistive layer, $e = h^{(pi)}/l$
C	$C = -l^3/I$	e_l	geometric property of the delaminated piezoresistive layer, $e_l = h^{(pi)}/l_l$
d	half-length of delamination	e_r	geometric property of the delaminated piezoresistive layer, $e_r = h^{(pi)}/l_r$
d_l	point at the left edge of central delamination (m)	F_n	coefficients in Chebyshev polynomial expansions for the interfacial shear stress, τ^*
d_r	point at the right edge of central delamination (m)	F_n^r	coefficients in Chebyshev polynomial expansions for the delaminated coating for the interfacial shear stress, τ^{*r}
$E^{(i)}$	elastic modulus of the insulating layer (Pa)	G	$G = \left(2\left(1-v^{(s)^2}\right)E^{(pi)}\right)/\pi E^{(s)}$
$E^{(pi)}$	elastic modulus of the piezoresistive layer (Pa)	GF	gauge factor of the piezoresistive layer
$E^{(s)}$	elastic modulus of the substrate (Pa)	H_n	coefficients in Chebyshev polynomial expansions for the axial stress, σ^*
$E^{(s)}$	elastic modulus of the substrate (Pa)	H_n^r	coefficients in Chebyshev polynomial expansions for the delaminated coating for the interfacial axial stress, σ^{*r}

$h^{(i)}$	thickness of the insulating layer (m)	M_d^*	normalized bending moment at the delaminated edge, $M_d^* = M_d / E^{(pi)}$
$h^{(pi)}$	thickness of the piezoresistive layer (m)	n	$n = 0,1,2,.....N$
I	moment of inertia	Q	Shear force (N)
K_1	$K_1 = E^{(i)} l / \left(2E^{(pi)} h^{(i)} \left(1+v^{(i)}\right)\right)$	R_i	instantaneous electrical resistance of the piezoresistive layer (**Ω**)
K_2	$K_2 = \left(E^{(i)}\left(1-v^{(i)}\right)l\right) / \left(E^{(pi)} h^{(i)}\left(1+v^{(i)}\right)\left(1-2v^{(i)}\right)\right)$	R_o	electrical resistance of the piezoresistive layer with zero mechanical load (**Ω**)
k	$k = 0, 1, 2, ..., N$	sign	Signum function
l	half-length of the coating layer (m)	T_n	displacement within the insulating layer along *x*-axis (m)
l_l	half-length of the left side of the centrally delaminated coating	T_c	compressive axial force at the delaminated edge (N)
l_{eff}	effective half-length of the coating after delamination	T_c^*	$T_c^* = T_c / E^{(pi)}$
l_r	half-length of the coating at the right side of central delamination	t_l	point along (x,0) at the left edge of the coating layer (m)
M	bending moment	t_r	point along (x,0) at the right edge of the coating layer (m)

N	number of Chebyshev polynomials terms
$u_y^{(i)}$	displacement field within the insulating layer along *y*-axis (m)
$u_x^{(pi)}$	displacement field within the piezoresistive layer along *x*-axis (m)
$u_y^{(pi)}$	displacement field within the piezoresistive layer along *y*-axis (m)
$u_x^{(s)}$	displacement field at the surface the substrate (m)
W	characterises the external load applied to the elastic substrate, $w = \frac{\varepsilon_x^{(s)}(\pm\infty)}{E^{(pi)}}$ (/Pa)
X	$X = \frac{E^{(pi)}\alpha_{11} l}{h^{(pi)}\left(GF - \left(1 + 2v^{(pi)}\right)\right)}$
x	horizontal coordinate
x_l	horizontal coordinate at the left side of central delamination
x_r	horizontal coordinate at the left side of central delamination
$u_x^{(i)}$	displacement field within the insulating layer along *x*-axis (m)
y	vertical coordinate
z	physical property of the substrate, $z = \pi E^{(s)} / \left(2\left(1 - v^{(s)2}\right)\right)$

Greek Symbols

α_{11}	Piezoresistive coefficient matrix component
α_{12}	Piezoresistive coefficient matrix component
ε_x	strain field along *x*-axis
$\varepsilon_x^{(pi)}$	strain field within the piezoresistive layer along x-axis
$\varepsilon_x^{(s)}$	strain field at the surface the substrate
λ	normalized point along *x*-axis, $\lambda = x / l$

Y $Y = E^{(pi)}\alpha_{12} / \left(\left(GF - \left(1 + 2v^{(pi)}\right)\right)\right)$

λ_{lk} collocation points along *x*-axis of the left part of the centrally delaminated coating layer, $\lambda_{lk} = \lambda_k$

λ_{rk} collocation points along *x*-axis of the right part of the centrally delaminated coating layer, $\lambda_{rk} = \lambda_k$

$\lambda_{lk}^{'}$ $\lambda_{lk}^{'} = \frac{2e_l}{e} - 1 - \frac{e_l}{e_r} + \frac{e_l}{e_r}\cos\theta_k$

$\lambda_{rk}^{'}$ $\lambda_{rk}^{'} = -\frac{2e_r}{e} + 1 + \frac{e_r}{e_l} + \frac{e_r}{e_l}\cos\theta_k$

λ_l^* $\lambda_l^* = 2e_l\frac{e_r - e}{ee_r} - 1$

λ_r^* $\lambda_r^* = -2e_r\frac{e_l - e}{ee_l} + 1$

$v^{(i)}$ Poisson ratio of the insulating layer

$v^{(pi)}$ Poisson ratio of the piezoresistive layer

λ_k collocation points along *x*-axis of the coating layer,

θ_k $\theta_k = \left(k / N + 1\right)\pi$

σ_o^{*r} normalized bending stress, $\sigma_o^{*r} = \sigma_o / E^{(pi)}$

σ_y axial stress along *y*-axis (Pa)

σ^{∞} axial stress along x-axis at both ends of the substrate (Pa)

τ interfacial shear stress (Pa)

τ_{xy} interfacial shear stress at *x*-*y* plane (Pa)

τ^{*l} normalized interfacial shear stress at the left part of the centrally delaminated coating layer, $\tau^{*l} = -\tau / E^{(pi)}$

τ^{*r} normalized interfacial shear stress at the right part of the centrally delaminated coating layer (Pa), $\tau^{*r} = \tau / E^{(pi)}$

$\nu^{(s)}$	Poisson ratio of the substrate

Subscripts

d	delamination length
k	$k = 0, 1, 2, \ldots, N$
l	left edge of the delaminated coating layer
n	left edge of the coating layer
o	arbitrary designation
r	right edge of the delaminated coating layer

Superscript

i	instantaneous
(i)	insulating layer
(pi)	piezoresistive layer
(s)	substrate
∞	remote
*	normalized value

4.1 Mathematical Formulation

Due to the material mismatch or residual stresses or application of mechanical or thermal load on a bi-layered coating-substrate system, it could result in the bending of the coating layer. The presence of bending, together with the interfacial conditions will strongly affect the piezoresistive response of the bi-layered system. For this reason, the analytical model of the coating-substrate system was developed to understand this mechanism in the presence of bending and delamination. Descriptive examples were presented to show the effect of the interfacial delamination, geometric and material properties on the piezoresistive response of the coating-substrate system.

4.1.1 Perfect bonding in the coating-substrate system with bending effects

A plane strain analysis of a bi-layered coating bonded to an isotropic and homogenous elastic substrate modelled as a half-plane was conducted. The half-plane model of the substrate represents the case where the thicknesses of the coating layers are significantly lower than that of the substrate [82, 100 - 102]. The Cartesian coordinate system (*x, y*) was utilized with the origin at the center of the insulating layer-substrate interface and the length of the bi-layered coating was 2*l*. In this model, the structure is assumed to have unit width. A mechanical stress, σ^{∞} is applied to the substrate at the surfaces $(\pm\infty, y)$ shown in Fig. 4-1. The application of the axial stress generates a shear stress, τ and axial stress, σ_o as shown in Fig. 4-1. The superscripts '(pi)', '(i)' and '(s)' were used to represent the physical properties of the piezoresistive layer, the insulating layer and the substrate, respectively.

As a result of the structural descriptions of the piezoresistive layer, the following assumptions can be made:

(i) Because of the relatively small thickness of the piezoresistive layer, the axial stress, $\sigma_x^{(pi)}$ and axial displacement, $u_x^{(pi)}$ are assumed to be uniformly distributed across its thickness.

(ii) The interfacial shear stress, τ and interfacial normal stress, σ transferred along the piezoresistive layer – insulating layer will act as distributed body forces for the piezoresistive layer.

(iii) The insulating layer is assumed to transfer shear and normal loads from the substrate to the piezoresistive layer. Also, its elastic modulus is assumed to be much lower than its shear modulus so as to behave in a pure shear manner for the loading conditions considered.

A plane strain analysis of the bi-layered coating-substrate system is also done here with the substrate modelled as a half-plane assumed to be isotropic, homogenous, elastic.

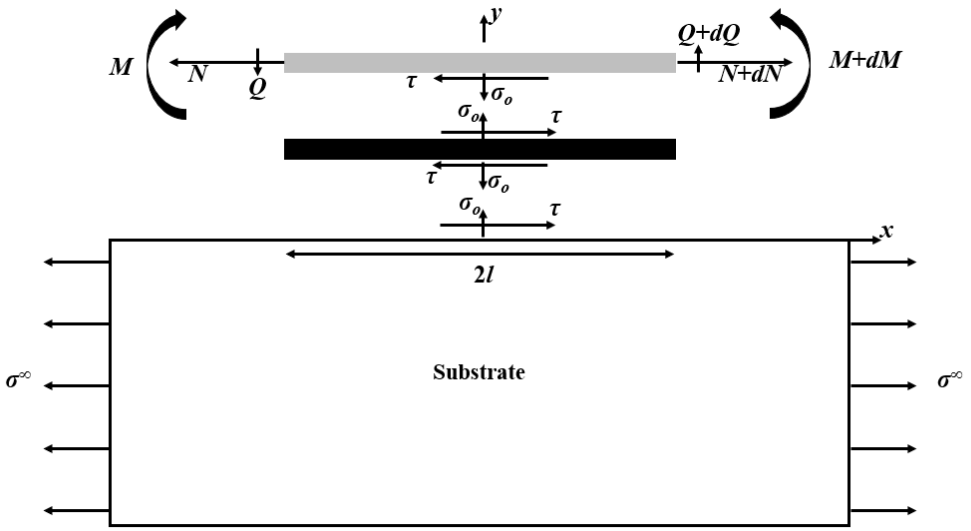

Figure 4-1 Free body diagram of the bi-layered coating-substrate system

Equation(s) of constraints and loads for the piezoresistive layer

$$\frac{d\sigma_x^{(pi)}}{dx} - \frac{\tau(x)}{h^{(pi)}} = 0, \tag{4-1}$$

$$\frac{d^2M}{dx^2} + \sigma_o = 0, \tag{4-2}$$

where the average axial stress, $\sigma_x^{(pi)}$ can be expressed in terms of the interfacial shear stress as:

$$\sigma_x^{(pi)} = \int_{-l}^{x} \frac{\tau(\xi)}{h^{(pi)}} d\xi. \tag{4-3}$$

Also, the bending moment can be expressed as:

$$M = E^{(pi)} I \frac{d^2 u_y^{(pi)}}{dx^2}. \tag{4-4}$$

where

$$\frac{d^4 u_y^{(pi)}}{dx^4} = -\frac{\sigma_o(x)}{E^{(pi)} I} \tag{4-5}$$

$E^{(pi)}$ and I are the effective Young's modulus and the moment of inertia of the piezoresistive layer, respectively.

Since the ends of the piezoresistive layer is a traction-free, the axial stress, bending moments and the transverse shear force will be zero as and can be expresses as:

$$\sigma_x^{(pi)} = 0, \quad M = 0, \quad Q = 0, \quad \int_{-l}^{l} \tau(\xi) d\xi = 0, \quad |x| = l. \tag{4-6}$$

The constitutive relation of the piezoresistive layer, in terms of the axial stress $\sigma_x^{(pi)}$, and the normal stress, σ_o can be expressed as:

$$\frac{R_i - R_o}{R_o}(x) = \left(1 + 2v^{(pi)}\right)\varepsilon_x^{(pi)}(x) + \alpha_{11}\sigma_x^{(pi)}(x) - \alpha_{12}\sigma_o(x), \tag{4-7}$$

and re-arranging Eq. 4-6 and substituting Eq. 4-3 gives the strain distribution in the piezoresistive layer:

$$\varepsilon_x^{(pi)}(x) = \frac{1}{GF - \left(1 + 2v^{(pi)}\right)}\left(\alpha_{11}\int_{-l}^{x}\frac{\tau(\xi)}{h^{(pi)}}d\xi - \alpha_{12}\sigma_o(x)\right), \tag{4-8}$$

and the longitudinal displacement field being:

$$u_x^{(pi)}(x) = \frac{1}{GF - \left(1 + 2v^{(pi)}\right)}\left(\alpha_{11}\int_{-l}^{x}\int_{-l}^{\xi}\frac{\tau(\xi)}{h^{(pi)}}d\xi - \alpha_{12}\int_{-l}^{x}\sigma_o(\xi)d\xi\right). \tag{4-9}$$

Equation(s) of constraints and loads for the insulating layer

To analyse the loading conditions on the insulating layer, it was modelled as a continuous spring with shear and normal stiffnesses. And it was assumed that the shear stress, τ and normal stress, σ_o in the insulating layer are uniformly distributed across its thickness since it is a relatively thin layer. Since the piezoresistive layer and the substrate are bonded through this layer, the displacements at the upper and lower surfaces of the insulating layer based on continuity conditions [83, 107 – 109, 114, 115] will satisfy the following relations:

$$u_x^{(i)}\left(x, h^{(i)}\right) - u_x^{(i)}\left(x, 0\right) = \frac{2h^{(i)}\left(1 + v^{(i)}\right)\tau}{E^{(i)}}, \tag{4-10}$$

$$u_y^{(i)}\left(x,h^{(i)}\right)-u_y^{(i)}\left(x,0\right)=\frac{h^{(i)}\left(1+v^{(i)}\right)\left(1-2v^{(i)}\right)\sigma_o}{E^{(i)}\left(1-v^{(i)}\right)}. \tag{4-11}$$

Equation(s) of constraints and loads for the substrate

The boundary conditions for the substrate are given as:

$$\sigma_{xy}^{(s)}\left(x,0\right)=\begin{cases}\tau(x), & |x|<l\\ 0, & |x|>l\end{cases}, \tag{4-12}$$

$$\sigma_{y}^{(s)}\left(x,0\right)=\begin{cases}\sigma_o(x), & |x|<l\\ 0, & |x|>l\end{cases}, \tag{4-13}$$

$$\sigma_x^{(s)}\left(\pm\infty,y\right)=\sigma^{\infty}=E^{(s)}\varepsilon^{(\infty)}. \tag{4-14}$$

In order to express the mechanical fields of the substrate in terms of the interface strains, $\frac{du_x^{(s)}}{dx}$ and $\frac{du_y^{(s)}}{dx}$, the exact solutions of the half-plane subjected to concentrated forces on the surface were applied [82, 114, 116]. Based on the fundamental solutions of a half elastic plane subjected to a concentrated longitudinal force and a vertical concentrated force and making use of the superposition principle, the strain fields can be expressed as:

$$\frac{du_x^{(s)}\left(x,0\right)}{dx}=\left(1-2v^{(s)}\right)\frac{1+v^{(s)}}{E^{(s)}}\sigma_o\left(x\right)+\varepsilon_x^{(s)}\left(\pm\infty\right)-\frac{2\left(1-v^{(s)^2}\right)}{\pi E^{(s)}}\left(\int_{-l}^{-l}\frac{\tau\left(\xi\right)}{x-\xi}d\xi\right), \tag{4-15}$$

$$\frac{du_y^{(s)}(x,0)}{dx} = -\left(1-2v^{(s)}\right)\frac{1+v^{(s)}}{E^{(s)}}\tau(x) - \frac{2\left(1-v^{(s)^2}\right)}{\pi E^{(s)}}\int_{-l}^{l}\frac{\sigma_o(\xi)}{x-\xi}d\xi\,. \tag{4-16}$$

Taking the advantage of the continuity condition and the interfaces, substituting Eqs. 4-8 and 4-15 into the derivative of Eq. 4-10 gives:

$$\begin{aligned}&\frac{1}{GF-\left(1+2v^{(pi)}\right)}\left(\alpha_{11}\int_{-l}^{x}\frac{\tau(\xi)}{h^{(pi)}}d\xi-\alpha_{12}\sigma_o(x)\right)-\left(1-2v^{(s)}\right)\frac{1+v^{(s)}}{E^{(s)}}\sigma_o(x)-\varepsilon_x^{(s)}(\pm\infty)\\&+\frac{2\left(1-v^{(s)^2}\right)}{\pi E^{(s)}}\left(\int_{-l}^{-l}\frac{\tau(\xi)}{x-\xi}d\xi\right)=\frac{2h^{(i)}\left(1+v^{(i)}\right)}{E^{(i)}}\frac{d\tau(x)}{dx}\end{aligned}\,. \tag{4-17}$$

Similarly, substituting Eqs. 4-5 and 4-16 gives into the derivative of Eq. 4-11 gives:

$$\begin{aligned}&-\frac{1}{E^{(pi)}I}\int_{-l}^{x}(x-\xi)^2\sigma_o(\xi)d\xi+\left(1-2v^{(s)}\right)\frac{1+v^{(s)}}{E^{(s)}}\tau(x)+\frac{2\left(1-v^{(s)^2}\right)}{\pi E^{(s)}}\left(\int_{-l}^{l}\frac{\sigma_o(\xi)}{x-\xi}d\xi\right)\\&=\frac{h^{(i)}\left(1+v^{(i)}\right)\left(1-2v^{(i)}\right)}{E^{(i)}\left(1-v^{(i)}\right)}\frac{d\sigma_o(x)}{dx}\end{aligned}\,. \tag{4-18}$$

Normalizing the Eqs. 4-6, 4-17 and 4-18 to make them unitless for simplification gives:

$$\int_{-1}^{1}\tau^*(\phi)d\phi=0\,, \tag{4-19}$$

$$X\int_{-1}^{1}\tau^*(\phi)d\phi-(Y+A)\sigma_o^*(\lambda)+G\int_{-1}^{1}\frac{\tau^*(\phi)}{\lambda-\phi}d\phi-\frac{1}{K_1}\frac{d\tau^*(\lambda)}{d\lambda}=\varepsilon_x^{(s)}(\pm\infty)\,, \tag{4-20}$$

$$C\int_{-1}^{1}(\lambda-\phi)^2\sigma_o^*(\phi)d\phi+A\tau^*(\lambda)+G\int_{-l}^{l}\frac{\sigma_o^*(\phi)}{\lambda-\phi}d\phi-\frac{1}{K_2}\frac{d\sigma_o^*(\lambda)}{d\lambda}=0\,, \tag{4-21}$$

where

$$\tau^* = \frac{\tau}{E^{(pi)}}, \quad \sigma_o^* = \frac{\sigma_o}{E^{(pi)}}$$

$$X = \frac{E^{(pi)}\alpha_{11} l}{h^{(pi)}\left(GF - \left(1+2v^{(pi)}\right)\right)}, \quad Y = \frac{E^{(pi)}\alpha_{12}}{\left(GF - \left(1+2v^{(pi)}\right)\right)}, \quad A = E^{(pi)}\left(1-2v^{(s)}\right)\frac{1+v^{(s)}}{E^{(s)}}, \quad . \quad (4\text{-}22)$$

$$G = \frac{2\left(1-v^{(s)^2}\right)E^{(pi)}}{\pi E^{(s)}}, \quad K_1 = \frac{E^{(i)} l}{2E^{(pi)} h^{(i)}\left(1+v^{(i)}\right)}, \quad C = -\frac{l^3}{I}, \quad K_2 = \frac{E^{(i)}\left(1-v^{(i)}\right) l}{E^{(pi)} h^{(i)}\left(1+v^{(i)}\right)\left(1-2v^{(i)}\right)}$$

Solution to the integral equation

Since the resulting integral equations are singular, the solutions involve a square-root singularity at the ends of the coating layers [84, 116] [82, 116]. In this regard, the general solutions for the interfacial shear and normal stresses can be expressed in the form of Chebyshev polynomials of the first kind as:

$$\tau^* = \frac{1}{\sqrt{1-\lambda^2}}\sum_{n=1}^{N} F_n T_n(\lambda), \quad \sigma_o^* = \frac{1}{\sqrt{1-\lambda^2}}\sum_{n=1}^{N} H_n T_n(\lambda), \quad (4\text{-}23)$$

where T_n is the Chebyshev polynomial of the first kind and it is defined by:

$$T_n = \cos\left(n\theta_k\right), \quad (4\text{-}24)$$

and

$$\lambda_k = \cos\theta_k . \quad (4\text{-}25)$$

F_n and H_n are the Chebyshev polynomial coefficients for the shear stress and normal stress, respectively.

If the polynomial expansion converges at $k = N$, then:

$$\theta_k = \frac{k}{N+1}\pi \qquad k = 1,2,...N \quad . \tag{4-26}$$

Therefore, Eqs. 4-20 and 4-21 become:

$$\begin{aligned} &\sum_{n=1}^{N} F_n \left(X \frac{\sin(n\theta_k)}{n} - G\pi \frac{\sin(n\theta_k)}{\sin\theta_k} - \frac{\cos(n\theta_k)\cot(n\theta_k) + n\sin(n\theta_k)}{K_1(\sin\theta_k)^2} \right) \\ &-(Y+A)\sum_{n=1}^{N} H_n \left(\frac{\cos(n\theta_k)}{\sin\theta_k} \right) = \varepsilon_x^{(s)}(\pm\infty) \qquad k = 1,2,...N \end{aligned} \quad , \tag{4-27}$$

$$\begin{aligned} &\sum_{n=1}^{N} H_n \left(C\int_{-1}^{\lambda_k} (\lambda_k - \phi)^2 \frac{\cos(n\theta_k)}{\sin\theta_k} d\phi - G\pi \frac{\sin(n\theta_k)}{\sin\theta_k} - \frac{\cos(n\theta_k)\cot(n\theta_k) + n\sin(n\theta_k)}{K_2(\sin\theta_k)^2} \right) \\ &+A\sum_{n=1}^{N} F_n \frac{\cos(n\theta_k)}{\sin\theta_k} = 0 \qquad k = 1,2,...N \end{aligned} \quad . \tag{4-28}$$

4.1.2 Central delamination in the coating-substrate system with bending effects

Property mismatch between the substrate and the coating or high localized stress or poor bonding condition may consequently and significantly affect the piezoresistive response of the coating-substrate system [114]. This delamination may result in a bending state of the piezoresistive layer. In this regard, it is crucial to the piezoresistive performance of the conductive layer to analytically study and understand the effects this bending condition have on the system. In this section, the study is done on the combined effects of delamination and bending.

Figure 4-2 shows the case of the bi-layered coating substrate system with central debonding in $|x| < d$, where d represents half-length of the delaminated part. Thus, the effective length of the piezoresistive layer becomes $2(l-d)$. In the bending state, the ends of the delaminated part of the piezoresistive layer at $|x| = d$ are subjected to an axial compressive force, T_c , and a moment, *M*. as shown in Fig. 4-2 (b).

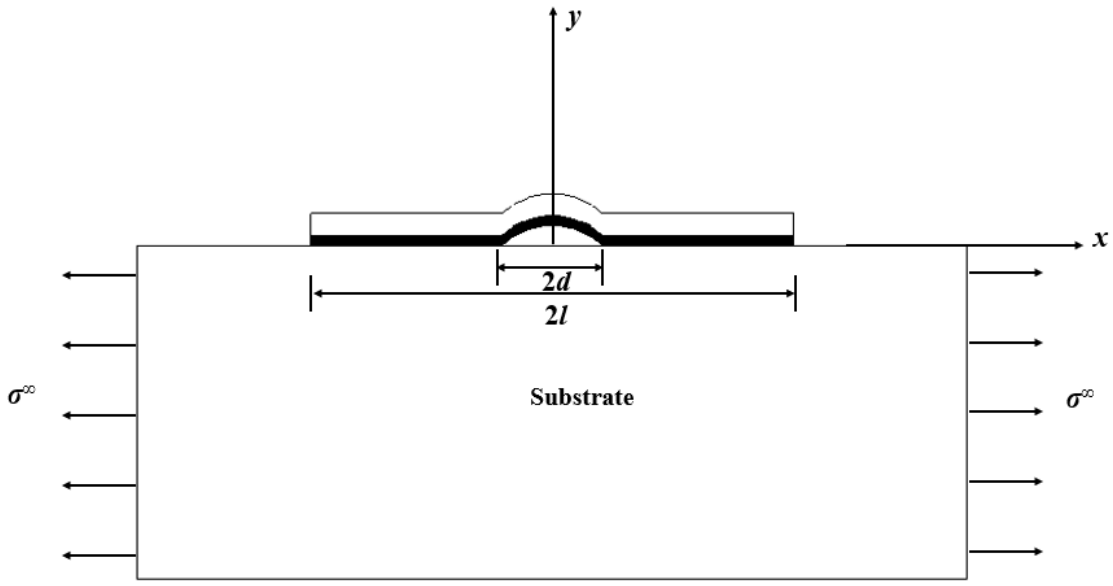

(a)

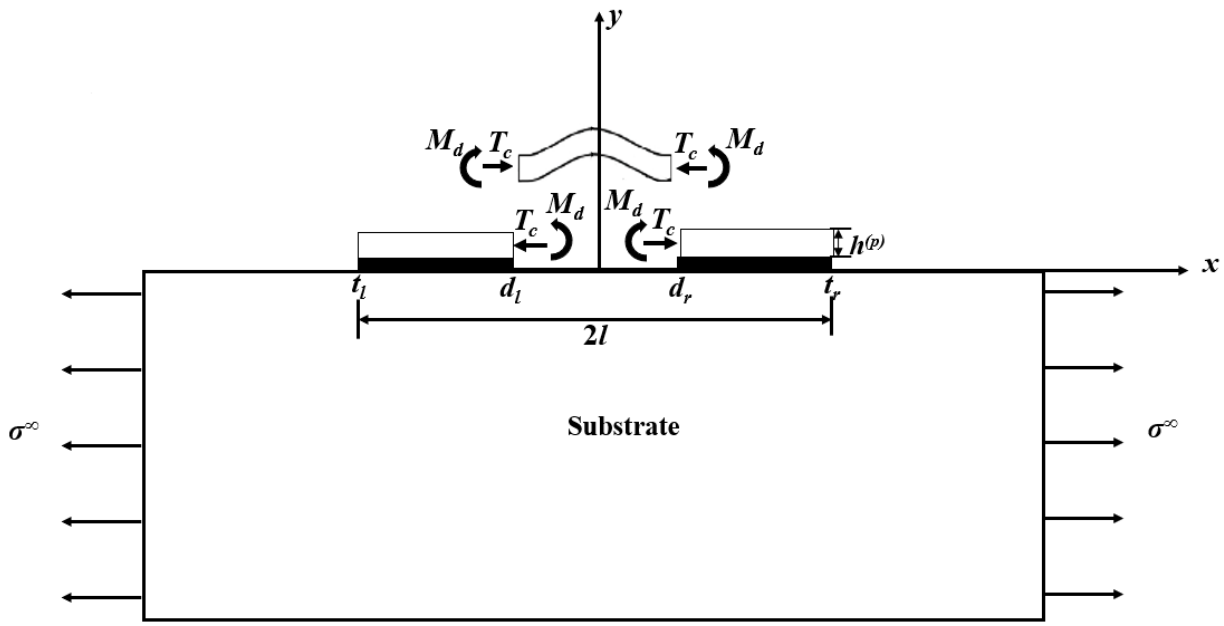

(b)

Figure 4.2 Schematic of the bi-layered coating-substrate system with (a) central delamination and (b) its free body diagram

Equation(s) of constraints and loads for the piezoresistive layer

The piezoresistive constitutive relation of the piezoresistive layer is given as:

$$\frac{R_i - R_o}{R_o}(x) = \left(1 + 2v^{(pi)}\right)\varepsilon_x^{(pi)}(x) + \alpha_{11}\sigma_x^{(pi)}(x) - \alpha_{12}\sigma_o(x)\cdot \tag{4-29}$$

At the two ends, the following boundary conditions are obtainable:

$$\sigma_x^{(pi)} = 0, \qquad M = 0, \qquad Q = 0 \quad |x| = l\,, \tag{4-30}$$

while at the ends of the delaminated part, the boundary conditions are:

$$\sigma_x^{(pi)} = -\frac{T_c}{h^{(pi)}}, \qquad M = M_d\,, \qquad Q = 0 \quad |x| = d\,\cdot \tag{4-31}$$

M_d represents the bending moment at the ends of the delaminated part. Based on this model, there is no stress transfer between the substrate and the piezoresistive layer in the delaminated part, therefore, τ and σ_o are zero. At the center of the delaminated part, the following boundary conditions are obtainable due to the symmetry of the system:

$$\frac{du_y^{(pi)}}{dx}=0, \qquad \frac{d^3u_y^{(pi)}}{dx^3}=0, \qquad x=0\,. \tag{4-32}$$

According to the coating-substrate model, the axial displacement, and the slope of the piezoresistive layer at $x = d$ can be obtained by substituting the axial stress $\sigma_x^{(pi)}$ and moment M in Eq. (4-31) into Eqs. (4-9) and (4-4), respectively as:

$$u_x^{(pi)}(x)=\frac{\alpha_{12}\sigma_o h^{(pi)}-T_c\alpha_{11}}{h^{(pi)}\left(GF-\left(1+2\nu^{(pi)}\right)\right)}d \qquad x=d\ , \tag{4-33}$$

$$\frac{du_y^{(pi)}}{dx}=\frac{M_d d}{E^{(pi)}I}\,. \tag{4-34}$$

Based on the boundary conditions in Eqs. (4-33) and (4-34), the axial strain, $\varepsilon_x^{(pi)}$, and the slope of the piezoresistive layer in the bonded parts can be determined from Eqs. (4-1), (4-4) and (4-7) in terms of τ and σ_o, as

$$\frac{du_x^{(pi)}}{dx}=\varepsilon_x^s\left(\pm\infty\right)-\frac{1}{\left(GF-\left(1+2\nu^{(pi)}\right)\right)}\left(\alpha_{11}\int_d^x\frac{\tau\left(\xi\right)}{h^{(pi)}}d\xi+\alpha_{12}\sigma_o\left(\xi\right)-\frac{T_c}{h^{(pi)}}\right) \qquad d<x<l\,,` \tag{4-35}$$

$$\frac{du_y^{(pi)}}{dx}=-\frac{1}{E^{(pi)}I}\int_d^x\int_d^\eta\int_d^\zeta\sigma_o\left(\zeta\right)d\zeta d\eta d\xi+\frac{M_d x}{E^{(pi)}I} \qquad d<x<l\,. \tag{4-36}$$

Equation(s) of constraints and loads for the insulating layer

For the insulating layer, the displacements at its upper and lower surfaces based on continuity conditions [83, 107 – 109, 114, 115] will satisfy the following relations:

$$u_x^{(i)}\left(x,h^{(i)}\right)-u_x^{(i)}\left(x,0\right)=\frac{2h^{(i)}\left(1+\nu^{(i)}\right)\tau}{E^{(i)}}, \tag{4-37}$$

$$u_y^{(i)}\left(x,h^{(i)}\right)-u_y^{(i)}\left(x,0\right)=\frac{h^{(i)}\left(1+\nu^{(i)}\right)\left(1-2\nu^{(i)}\right)\sigma_o}{E^{(i)}\left(1-\nu^{(i)}\right)}. \tag{4-38}$$

Equation(s) of constraints and loads for the substrate

The boundary conditions for the substrate are given as:

$$\sigma_{xy}^{(s)}\left(x,0\right)=\begin{cases}\tau(x), & d<|x|<l\\ 0, & |x|>l,\quad |x|<d\end{cases}, \tag{4-39}$$

$$\sigma_{y}^{(s)}\left(x,0\right)=\begin{cases}\sigma_o(x), & d<|x|<l\\ 0, & |x|>l,\quad |x|<d\end{cases}, \tag{4-40}$$

$$\sigma_x^{(s)}\left(\pm\infty,y\right)=\sigma^{\infty}=E\varepsilon^{(\infty)}. \tag{4-41}$$

Based on the fundamental solutions of a half elastic plane subjected to a concentrated force and making use of the superposition principle, the strains resulting from the applied distributed τ and σ_o can be obtained for $x > 0$ as [82, 114, 116]:

$$\frac{du_x^{(s)}(x,0)}{dx}=\left(1-2v^{(s)}\right)\frac{\left(1+v^{(s)}\right)}{E^{(s)}}\sigma_o-\varepsilon_x^{(s)}(\pm\infty)-\frac{2\left(1-v^{(s)^2}\right)}{\pi E^{(s)}}\left(\int_{-l}^{-d}\frac{\tau(\xi)}{x-\xi}d\xi+\int_d^l\frac{\tau(\xi)}{x-\xi}d\xi\right), \tag{4-42}$$

$$\frac{du_y^{(s)}(x,0)}{dx}=-\left(1-2v^{(s)}\right)\frac{\left(1+v^{(s)}\right)}{E^{(s)}}\tau-\frac{2\left(1-v^{(s)^2}\right)}{\pi E^{(s)}}\left(\int_{-l}^{-d}\frac{\sigma_o(\xi)}{x-\xi}d\xi+\int_d^l\frac{\sigma_o(\xi)}{x-\xi}d\xi\right). \tag{4-43}$$

The horizontal displacement along the bonded part of the host surface can be obtained by integrating Eq. (4-42) as:

$$\begin{aligned}u_x^{(s)}(x,0)=&\left(1-2v^{(s)}\right)\frac{\left(1+v^{(s)}\right)}{E^{(s)}}\int_d^x\sigma_o(\zeta)d\zeta-\varepsilon_x^{(s)}(\pm\infty)(x-d)\\&-\frac{2\left(1-v^{(s)^2}\right)}{\pi E^{(s)}}\left(\int_{-l}^{-d}\ln|x-\zeta|\tau(\zeta)d\zeta+\int_d^l\ln|x-\zeta|\tau(\zeta)d\zeta\right)\end{aligned}. \tag{4-44}$$

Based on the continuity conditions in Eqs. (4-37) and (4-38) for the bonded interface ($d < x < l$), the following equations can be obtained, in terms of the interfacial shear stress, τ and interfacial normal stress, σ_o:

$$\begin{aligned}&\frac{1}{\left(GF-\left(1+2v^{(pi)}\right)\right)}\left(\alpha_{11}\int_d^x\frac{\tau(\xi)}{h^{(pi)}}d\xi+\alpha_{12}\sigma_o-\frac{T_c}{h^{(pi)}}\right)-\left(1-2v^{(s)}\right)\frac{\left(1+v^{(s)}\right)}{E^{(s)}}\sigma_o+\varepsilon_x^{(s)}(\pm\infty)\\&+\frac{2\left(1-v^{(s)^2}\right)}{\pi E^{(s)}}\left(\int_{-l}^{-d}\frac{\tau(\xi)}{x-\xi}d\xi+\int_d^l\frac{\tau(\xi)}{x-\xi}d\xi\right)=\frac{2h^{(i)}\left(1+v^{(i)}\right)}{E^{(i)}}\frac{d\tau}{dx}\end{aligned}, \tag{4-45}$$

$$\frac{2\left(1-v^{(s)^2}\right)}{\pi E^{(s)}}\left(\int_{-l}^{-d}\frac{\sigma_o(\xi)}{x-\xi}d\xi+\int_{d}^{l}\frac{\sigma_o(\xi)}{x-\xi}d\xi\right)+\left(1-2v^{(s)}\right)\frac{\left(1+v^{(s)}\right)}{E^{(s)}}\tau(x)-\frac{1}{E^{(pi)}I}\int_d^x\int_d^\eta\int_d^\zeta\sigma(\zeta)d\zeta d\eta d\xi$$
$$+\frac{M_d x}{E^{(pi)}I}=\frac{h^{(i)}\left(1+v^{(i)}\right)\left(1-2v^{(i)}\right)}{E^{(i)}\left(1-v^{(i)}\right)}\frac{d\sigma_o}{dx} \quad . \quad (4\text{-}46)$$

By substituting Eqs. (4-33) and (4-44) into Eq. (4-37), the following equation based on the axial displacement of the piezoresistive layer at $x = d$ can be expressed in terms of the axial force T_c as:

$$\frac{\alpha_{12}\sigma_o h^{(pi)}-T_c\alpha_{11}}{h^{(pi)}\left(GF-\left(1+2v^{(pi)}\right)\right)}d-\varepsilon_x^{(s)}(\pm\infty)d$$
$$+\frac{2\left(1-v^{(s)^2}\right)}{\pi E^{(s)}}\left(\int_{-l}^{-d}\ln|x-\zeta|\tau(\zeta)d\zeta+\int_{d}^{l}\ln|x-\zeta|\tau(\zeta)d\zeta\right)=\frac{2h^{(i)}\left(1+v^{(i)}\right)\tau(d)}{E^{(i)}} \quad . \quad (4\text{-}47)$$

The interfacial stresses σ_o and τ should also satisfy the following conditions based on the boundary conditions at the free ends of the piezoresistive layer:

$$\int_d^l\tau(\xi)d\xi=T_c, \quad (4\text{-}48)$$

$$\int_d^l\int_d^x\sigma_o(\xi)d\xi=M_d, \quad (4\text{-}49)$$

$$\int_d^l\sigma_o(\xi)d\xi=0. \quad (4\text{-}50)$$

Equations (4-45) to (4-50) offer a system of integral equations to determine σ_o and τ.

Solution of the singular integral equations

Just like the case for the coating-substrate system without delamination, the singular integrals were solved mainly through two steps. The first step involves normalizing the governing equations for convenience of analysis and the second step involves solving the normalized equations through Chebyshev polynomials expansion of the interfacial shear and normal stresses. Thus, according to Eqs. (4-22) and (4-51) , Eqns. (4-45) to (4-50) become Eqns. (4-52) to (4-57):

$$\left.\begin{aligned}
&\tau^{*r}=\frac{\tau}{E^{(pi)}},\quad \sigma_o^{*r}=\frac{\sigma_o}{E^{(pi)}}\\
&\lambda_l=\frac{x-x_l}{l_l},\quad \lambda_r=\frac{x-x_r}{l_r}\\
&e=\frac{h^{(pi)}}{l},\quad e_l=\frac{h^{(pi)}}{l_l},\quad e_r=\frac{h^{(pi)}}{l_r}\\
&l=\frac{1}{2}(t_r-t_l),\quad l_l=\frac{1}{2}(d_l-t_l),\quad l_r=\frac{1}{2}(t_r-d_r)\\
&X_r=\frac{E^{(pi)}\alpha_{11}l_r}{h^{(pi)}\left(GF-\left(1+2v^{(pi)}\right)\right)},\quad K_{1r}=\frac{E^{(i)}l_r}{2E^{(pi)}h^{(i)}\left(1+v^{(i)}\right)},\\
&T_c^*=\frac{T_c}{E^{(pi)}},\quad M_d^*=\frac{M_d}{E^{(pi)}}\\
&C=-\frac{l_r^3}{I},\quad K_{2r}=\frac{E^{(i)}\left(1-v^{(i)}\right)l_r}{E^{(pi)}h^{(i)}\left(1+v^{(i)}\right)\left(1-2v^{(i)}\right)}\\
&x_l=\frac{1}{2}(d_l+t_l),\quad x_r=\frac{1}{2}(t_r+d_r)\\
&\lambda_l^*=2e_l\frac{e_r-e}{ee_r}-1,\quad \lambda_r^*=-2e_r\frac{e_l-e}{ee_l}+1
\end{aligned}\right\},\qquad (4\text{-}51)$$

$$G\left(\int_{-1}^{1}\frac{\tau^{*l}(\zeta)}{\lambda_l-\zeta}d\xi+\int_{-1}^{1}\frac{\tau^{*r}(\zeta)}{\lambda_r-\zeta}d\zeta\right)-(A+Y)\sigma_o^{*r}+X\int_{\lambda_r}^{1}\tau^{*r}d\lambda_r-\frac{1}{K_1}\frac{d\tau^{*r}}{d\lambda_r}=\varepsilon_x^{(s)}(\pm\infty),\qquad (4\text{-}52)$$

$$G\left(\int_{-1}^{1}\frac{\sigma_o^{*l}(\zeta)}{\lambda_l-\zeta}d\zeta+\int_{-1}^{1}\frac{\sigma_o^{*r}(\zeta)}{\lambda_r-\zeta}d\zeta\right)+A\tau^{*r}-C\int_{-1}^{\lambda_r}(\lambda_r-\zeta)^2\sigma^{*r}(\zeta)d\zeta$$
$$+\frac{M_d^* l_r}{I}\lambda_r-\frac{1}{K_2}\frac{d\sigma_o^{*r}}{d\lambda_r}=0 \quad , \tag{4-53}$$

$$G\left(\int_{1}^{\lambda_l^*}\int_{-1}^{1}\frac{\tau^{*l}(\zeta)d\zeta}{\lambda_l-\zeta}d\lambda_l+\int_{\lambda_r^*}^{-1}\int_{-1}^{1}\frac{\tau^{*r}(\zeta)d\zeta}{\lambda_r-\zeta}d\lambda_r\right)-wd-\frac{XT_c^*}{l_r}d-Yd\sigma_o^{*r}(\lambda_r)=\frac{l_r}{K_1}\tau^r(-1) \quad , \tag{4-54}$$

$$\int_{-1}^{1}\tau^{*r}(\zeta)d\zeta=\frac{T_c^*}{l_r}, \tag{4-55}$$

$$\int_{-1}^{1}\sigma_o^{*r}(\zeta)d\zeta=0, \tag{4-56}$$

$$\int_{-1}^{1}(l_r-\zeta)\sigma_o^*(\zeta)d\zeta=M_d^*. \tag{4-57}$$

The general solution of the normalized interfacial shear and normal stresses can be expressed in terms of Chebyshev polynomials as:

$$\tau^*(\lambda_r)=\frac{1}{\sqrt{1-\lambda_r^{\,2}}}\sum_{n=0}^{\infty}F_n^r T_n, \tag{4-58}$$

$$\sigma^*(\lambda_r)=\frac{1}{\sqrt{1-\lambda_r^{\,2}}}\sum_{n=0}^{\infty}H_n^r T_n, \tag{4-59}$$

with

$$\lambda_r=\lambda_{rk}=\cos\left(\frac{k}{N+1}\pi\right)\qquad k=1,2,..N. \tag{4-60}$$

Owing to the symmetrical nature of the model, only the local coordinate system $\lambda_r = \lambda$ will be utilized. Thus, the general solution of the normalized interfacial shear and normal stresses can then be expressed by expanding the Chebyshev polynomials as:

$$
\begin{aligned}
&-\sum_{n=0}^{N} F_n^r \left[\pi G \left(\frac{\left(\lambda_{rk}^{'} - \operatorname{sgn}\left(\lambda_{rk}^{'}\right)\sqrt{\left(\lambda_{rk}^{'}\right)^2 - 1} \right)^n}{\operatorname{sgn}\left(\lambda_{rk}^{'}\right)\sqrt{\left(\lambda_{rk}^{'}\right)^2 - 1}} \right) + \pi G \left(\frac{\sin\left(n\frac{k}{N+1}\pi \right)}{\sin\left(\frac{k}{N+1}\pi \right)} \right) \right] \\
&-\sum_{n=0}^{N} F_n^r \frac{1}{K_1} \left\{ \frac{\cos\left(n\frac{k}{N+1}\pi \right)\cot\left(\frac{k}{N+1}\pi \right) + n\sin\left(n\frac{k}{N+1}\pi \right)}{\left(\sin\left(\frac{k}{N+1}\pi \right) \right)^2} \right\} \\
&-(A+Y)\sum_{n=1}^{N} H_n^r \left\{ \frac{\cos\left(n\frac{k}{N+1}\pi \right)}{\sin\left(\frac{k}{N+1}\pi \right)} \right\} - \pi X l_r \sum_{n=1}^{N-2} F_n^r \left(\frac{\sin\left(n\frac{k}{N+1}\pi \right)}{n\pi} \right) + X l_r F_0^r \frac{k}{N+1}\pi \\
&= \varepsilon(\pm\infty)
\end{aligned}
\qquad , \qquad (4\text{-}61)
$$

$$
\begin{aligned}
&-\pi\sum_{n=1}^{N} H_n^r \left(G\frac{\left(\lambda_{rk}^{'} - \operatorname{sgn}\left(\lambda_{rk}^{'}\right)\sqrt{\left(\lambda_{rk}^{'}\right)^2 - 1} \right)^n}{\operatorname{sgn}\left(\lambda_{rk}^{'}\right)\sqrt{\left(\lambda_{rk}^{'}\right)^2 - 1}} + G\frac{\sin\left(n\frac{k}{N+1}\pi \right)}{\sin\left(\frac{k-1}{N-1}\pi \right)} + C\int_{-1}^{\lambda_{rk}} \left(\lambda_{rk} - \zeta\right)^2 \frac{\cos\left(n\frac{k}{N+1}\pi \right)}{\sin\left(\frac{k}{N+1}\pi \right)} d\xi \right) \\
&\sum_{n=1}^{N} H_n^r \left(-\frac{1}{K_2} \left\{ \frac{\cos\left(n\frac{k}{N+1}\pi \right)\cot\left(\frac{k}{N+1}\pi \right) + n\sin\left(n\frac{k}{N+1}\pi \right)}{\left(\sin\left(\frac{k}{N+1}\pi \right) \right)^2} \right\} \right) \\
&+\frac{M_d^* l_r}{I}\lambda_{rk} + A\sum_{n=o}^{N} F_n^r \frac{\cos\left(n\frac{k}{N+1}\pi \right)}{\sin\left(\frac{k}{N+1}\pi \right)} = 0
\end{aligned}
\qquad , \qquad (4\text{-}62)
$$

$$\sum_{n=0}^{N} F_n^r G\left[\int_1^{\lambda_l^*} \frac{\left(\lambda_{lk}^{'} - \text{sign}(\lambda_{lk}^{'})\sqrt{(\lambda_{lk}^{'})^2 - 1}\right)^n}{\left(\text{sign}(\lambda_{lk}^{'})\sqrt{(\lambda_{lk}^{'})^2 - 1}\right)} d\lambda_{lk}^{'} + \int_{\lambda_r^*}^{-1} \frac{\left(\lambda_{rk}^{'} - \text{sign}(\lambda_{rk}^{'})\sqrt{(\lambda_{rk}^{'})^2 - 1}\right)^n}{\left(\text{sign}(\lambda_{rk}^{'})\sqrt{(\lambda_{rk}^{'})^2 - 1}\right)} d\lambda_{rk}^{'}\right]$$
$$-wd - \frac{XT_c^*}{l_r} d - Yd \sum_{n=1}^{N} H_n^r \frac{\cos\left(n\frac{k}{N+1}\pi\right)}{\sin\left(\frac{k}{N+1}\pi\right)} - \frac{l_r}{K_1}\tau^r(-1) = 0 \quad . \tag{4-63}$$

From Eqs. (4-55) to (4-57)

$$F_0^r = \frac{T_c^*}{l_r \pi},\ H_0^r = 0,\ H_1^r = \frac{M_d^*}{dl_r}. \tag{4-64}$$

Thus, F_0^r and H_1^r are related to the axial force, T_c and bending moment, M_d, respectively.

4.2 Results and Discussion

4.2.1 Perfect bonding in the coating-substrate system with bending effects

Figure 4-3 shows the typical local shear stress distributions of a bi-layered coating-substrate system for the physical properties shown in Table 3-1. The normalized interfacial shear stress, τ^* and normalized interfacial normal stress, σ_o^* were plotted along the normalized length, λ of the coating layer. The ratio of the thickness of the insulating layer to its length was varied to study its effects on the interfacial stresses. Both forms of interfacial stresses are concentrated at the ends of the coating layers and this is expected to significantly affect the local deformation of the bonded surface. For the range of insulating layer thickness chosen, there is very little changes in the interfacial shear stress distribution but significant ones for the axial stress which means the bending

effects are significant with changes in the thickness. As is common knowledge, increasing the thickness of a layer decreases the bending stress. Therefore, Fig. 4-4 is consistent with the changes that should be observed for the relationship between thickness of the insulating layer and σ_o^*.

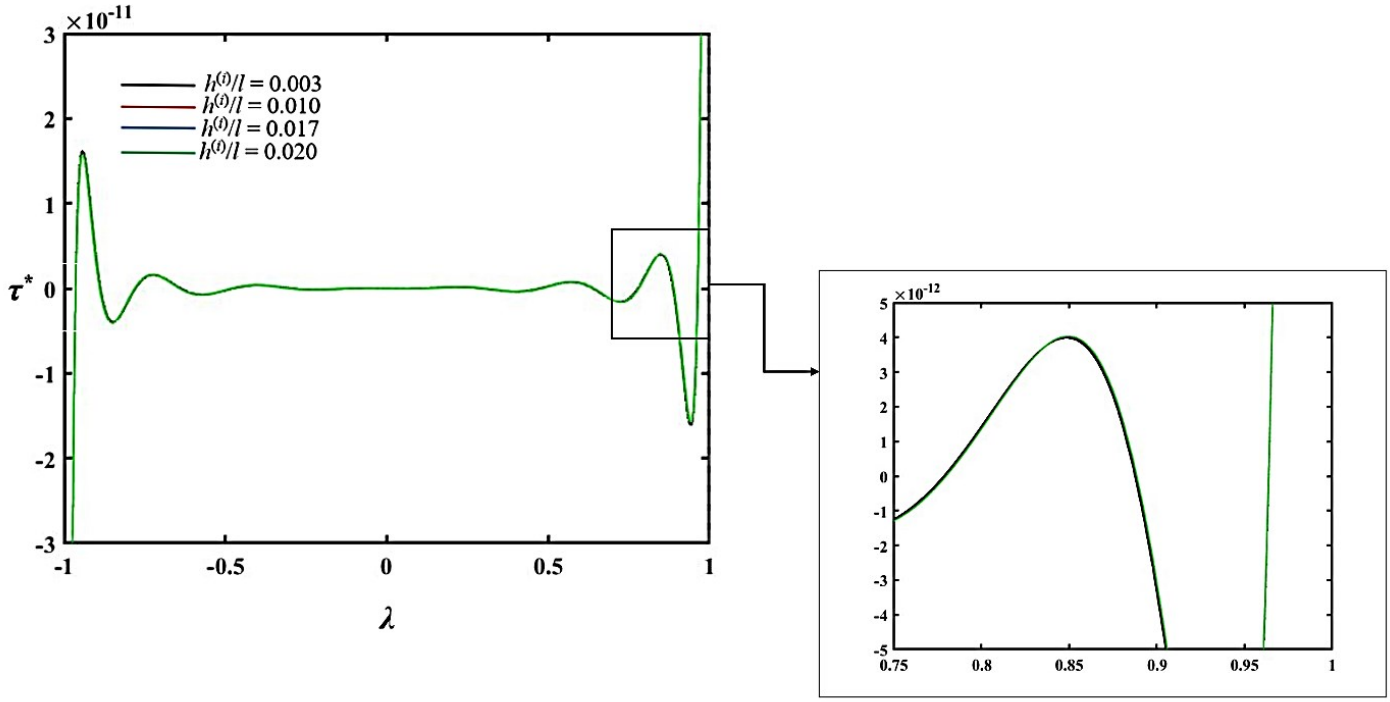

Figure 4.3 Plot of the interfacial shear stress distribution against the normalized length of the coating layers at varying thickness of the insulating layer

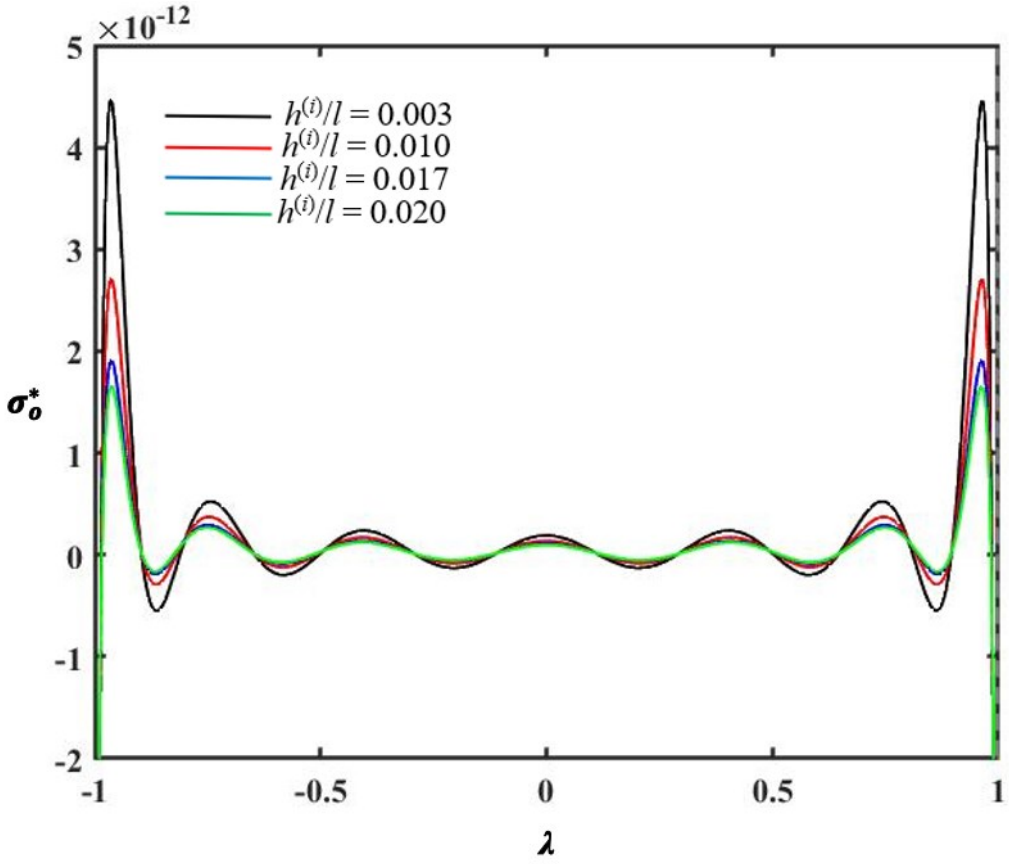

Figure 4.4 Plot of the interfacial axial stress distribution against the normalized length of the coating layers at varying thickness of the insulating layer

When the thickness of the piezoresistive layer was varied in the same range as that of the insulating layer (Figs. 4-5 and 4-6), the effects on the interfacial stresses were more significant. However, unlike the insulating layer, the interfacial stresses increase close to the ends of the piezoresistive layer with increasing thickness. This means increasing the thickness of the piezoresistive layer based on the loading conditions increases the vulnerability of the coating to edge delamination, as predicted by the case without bending effects [81].

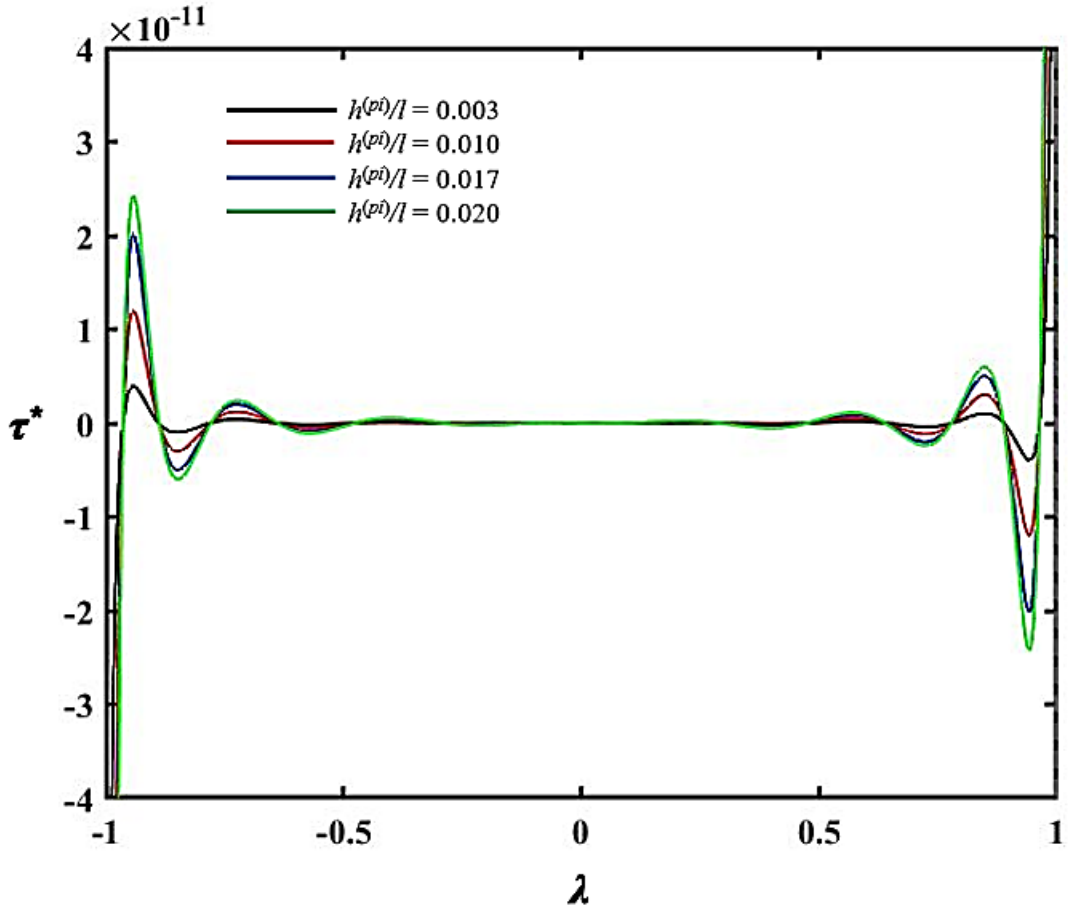

Figure 4.5 Plot of the interfacial shear stress distribution, against the normalized length of the coating layers at varying thickness of the piezoresistive layer

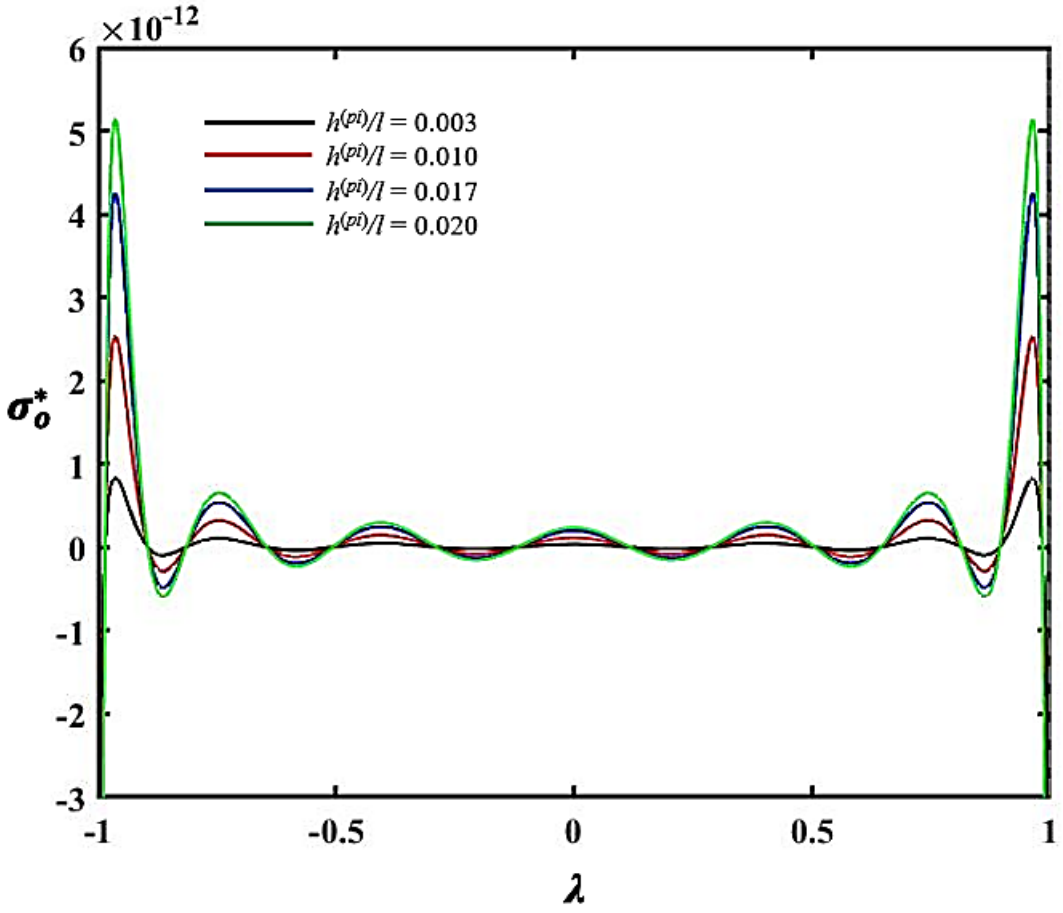

Figure 4.6 Plot of the interfacial axial stress distribution against the normalized length of the coating layers at varying thickness of the piezoresistive layer

4.2.2 Central delamination in the coating-substrate system with bending effects

The delamination length of the centrally delaminated coating-substrate system was also varied while keeping other physical properties of the system constant. In the following illustrations for the centrally delaminated system, the symmetry of the stresses was considered and only the right part of the delaminated coating was plotted. The delamination length was varied from 0.067 to 0.267 (equivalent to 1 mm/15 mm and 4 mm/15 mm, respectively) As expected, the stresses are concentrated at the delaminated ends as shown in Fig. 4-7. However, close to the delaminated

edges, the interfacial shear stress increases with the delamination length. The opposite of this relationship is true for the interfacial axial stress. This can be observed in Figs. 4-7 and 4-8 as the variation in the minimum and maximum points for all the cases of the interfacial shear stress and axial stress respectively.

On the other hand, keeping the delamination length constant and increasing the thickness of the insulating layer has very little effect on the interfacial shear stress distribution. Although, this effect is significant for the axial stress distribution as shown in Figs. 4-9 and 4-10.

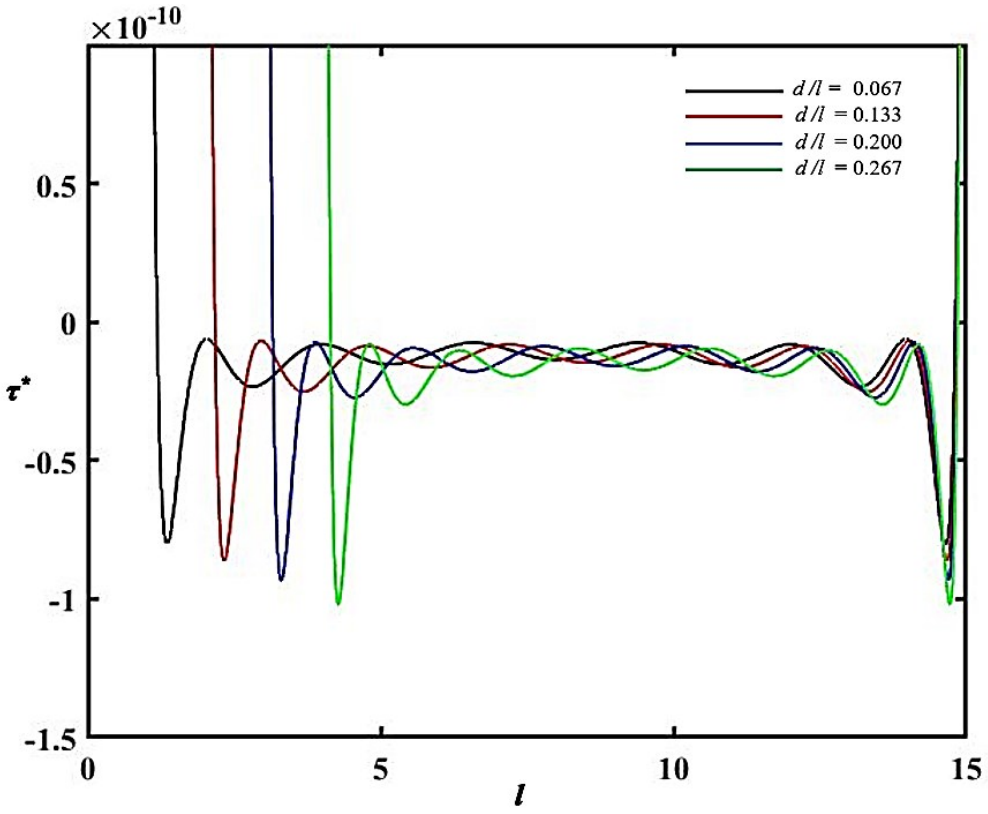

Figure 4.7 Plot of the interfacial shear stress distribution against the length of the coating layers at varying delamination length

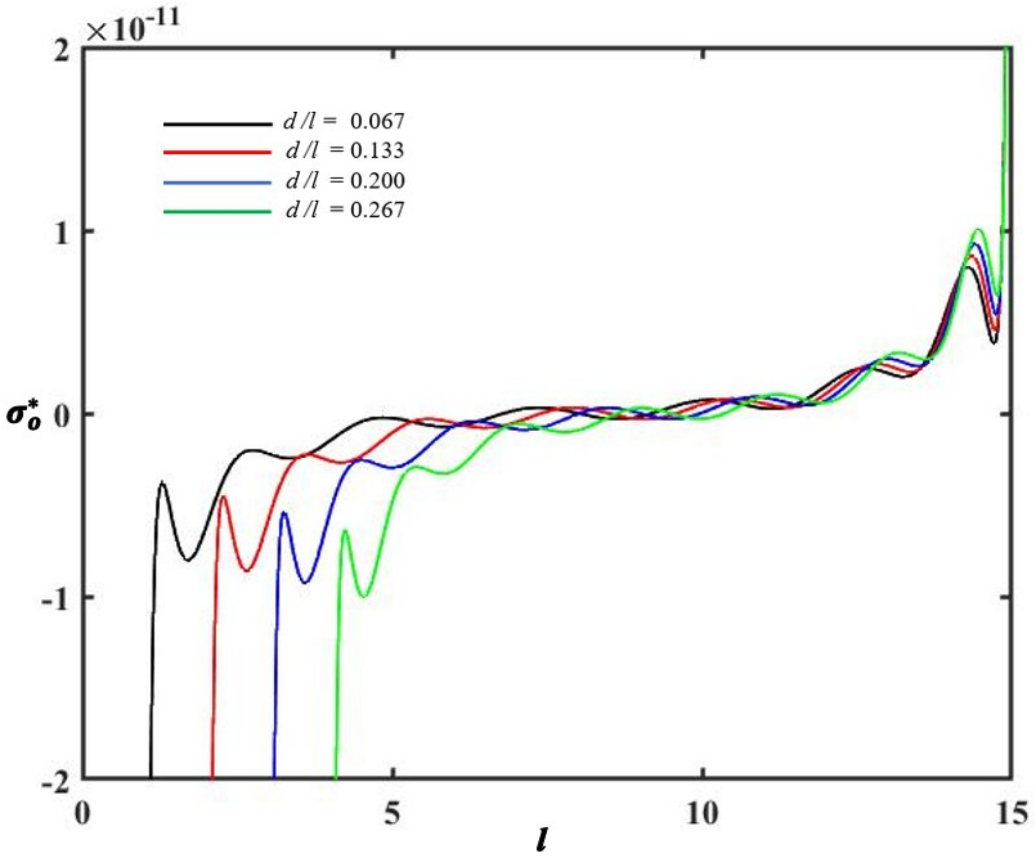

Figure 4.8 Plot of the interfacial axial stress distribution against the length of the coating layers at varying delamination length

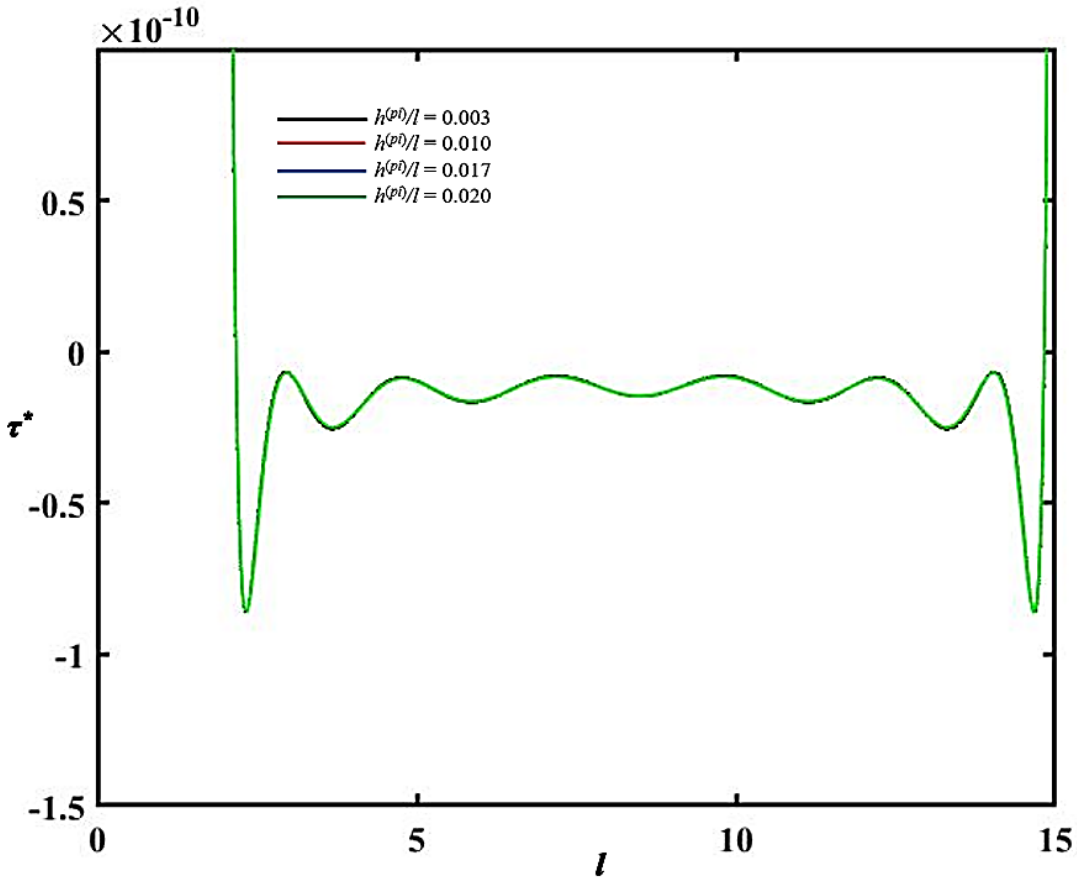

Figure 4.9 Plot of the interfacial shear stress distribution for the centrally delaminated system against the length of the coating layers at varying insulating thickness

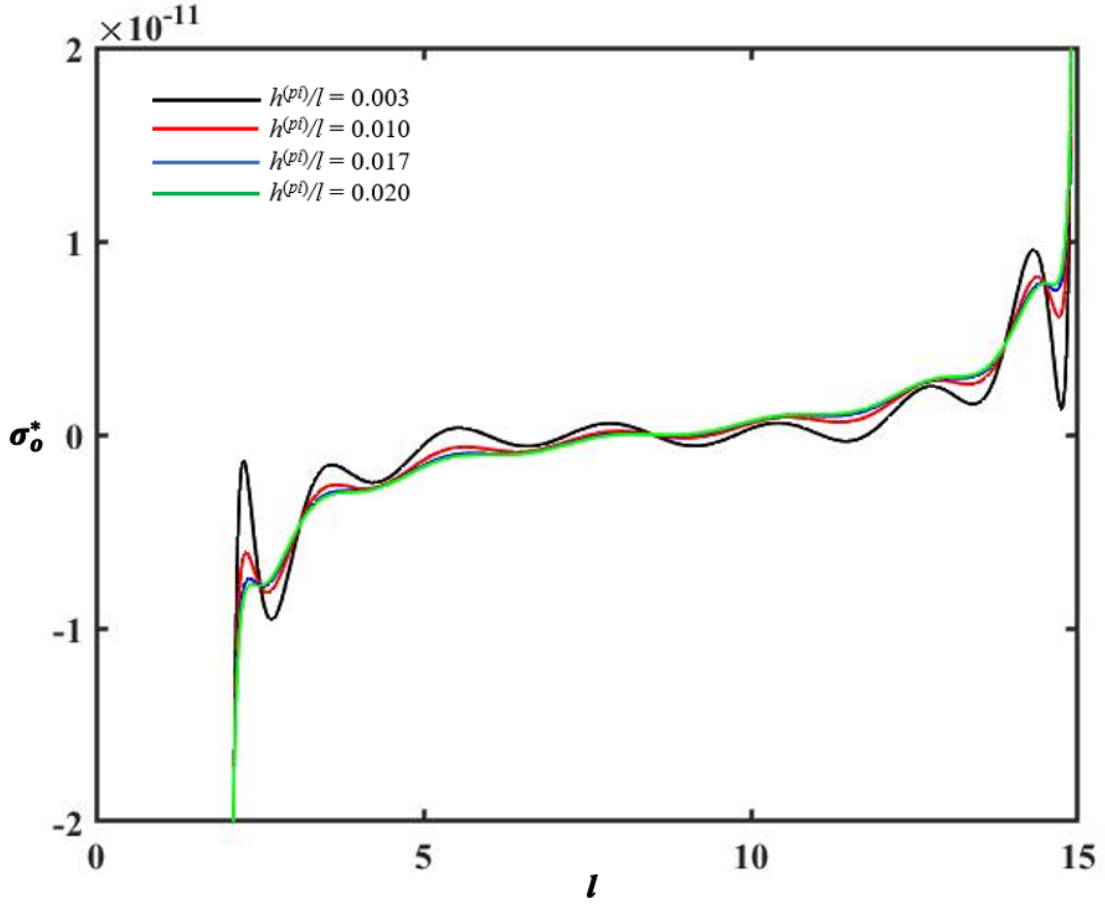

Figure 4.10 Plot of the interfacial axial stress distribution for the centrally delaminated system against the length of the coating layers at varying insulating thickness

4.3 Conclusions

Just as interfacial stress at the interface of a bi-layered coating-substrate system could be a shear stress; it could also be axial or a combination of both. The combination of both will affect the interfacial condition in a coating-substrate system and consequently the piezoresistive functionality of the system. In this regard, this Chapter focused on modelling the interfacial shear and normal stresses to predict the piezoresistive response of the of a coating-substrate system. Without loss of generality, the system was assumed to be a unit width for a simpler analysis and .

A plane strain analysis was done with the coating layers assumed to be several orders of magnitude thinner than the substrate, hence, the substrate was modelled as an elastic, isotropic and homogenous half-plane. The analysis was also extended to imperfect bonding conditions within the system in the form of central delamination. At the end of the analysis, the following conclusions were reached:

- Increasing the thickness of the piezoresistive layer based on the loading conditions increases the vulnerability of the coating to edge delamination more than increasing the thickness of the insulating layer in the same range.
- Also, as the coating continues to delaminate at the center, the interfacial stresses at the edges continue to increase.
- Increasing the insulating layer thickness while keeping the delamination length constant makes the interfacial stresses more concentrated at the edges.

Chapter 5
Conclusions

The primary focus of this research is the application of flame-sprayed coating as damage detection sensor. To first establish the selected coating as a piezoresistive sensor, its sensitivity to temperature, electrical resistance changes under mechanical load and strain changes was tested. These sensitivities are crucial to the sensor design. Also, its elastic properties were evaluated through nanoindentation to study the possible effect of material mismatch within the system. Also, the compatibility of the NiCoCrAlTaY and TiO_2 in terms of the dispersion phenomenon after deposition was checked in the SEM images of the final deposited coating. Eventually, the coating showed possibility of being used as a piezoresistive sensor because the sensitivity can be made negligible so as not to contribute to strain changes and it experienced good sensitivity to electrical resistance and strain changes under mechanical load.

Based on these test results, extensive experimentation was done on the bi-layered coating-substrate system. The electromechanical performance of the coating-substrate system was assessed by conducting quasi-static tensile and quasi-static cyclic test with *in* situ electrical measurements on the system. The microstructure of some of the fabricated coating-substrate system was also examined before and after conducting the electromechanical tests by using scanning electron microscopy (SEM) and energy-dispersive X-ray spectroscopy (EDX) to correlate it to the changes observed in the electromechanical tests and to observe the extent of damage, if any to the coating. The selected materials for the bi-layered system: materials, namely alumina, as an electrically insulating layer, the blended nickel alloy, as the sensor, and the silver-filled epoxy were suitable for strain sensing objective. This because a well-integrated coating-substrate system was formed

for adequate strain measurement, there was negligible contribution of the temperature to the strain changes in the conductive layer and electrical resistance changes corresponded to strain changes. The interfacial adhesion was strong because interfaces were still mostly intact after mechanical loading. Also of equal importance was that flame spray deposition on the CFRP without first depositing a low temperature heat sink as is always obtainable in literature.

Developing analytical models to predict the piezoresistive response of the bi-layered coating-substrate system was another objective of this research. The central themes were the effects of the interfacial stresses, shear and axial, on the piezoresistive response since these stresses contribute significantly to the piezoresistive performance of the system. Also included in this study is the effect of material and geometric properties on these strain transfer mechanisms.

To this end, a plane strain analysis was done with the coating layers assumed to be several orders of magnitude thinner than the substrate and the substrate was modelled as an elastic, isotropic and homogenous half-plane. Since delamination sometimes occurs due to residual stresses or mechanical loads, the study was expanded to include edge and central delamination in the system. Subsequently, effects of bending will have on the piezoresistive layer was studied. At the end of the analysis, it was found that material and geometric properties of the coating layers and the substrate largely influence the strain transfer mechanism in the bi-layered coating-substrate system. the study revealed that introducing dielectric/insulating layer reduces the stress concentration at the edges of the coating and the axial stress distribution at the centrally delaminated part of the piezoresistive layer. It also reduces the tendency for edge delamination to continue growing. It has little effect on axial stress within the delaminated length when the length is above 20% of the total coating length but significant when the delaminated length is otherwise.

Also, when bending effects were introduced in the model, increasing the thickness of the piezoresistive layer increases the vulnerability of the coating to edge delamination more than increasing the thickness of the insulating layer in the same range. In addition, central delamination growth increases the interfacial stresses at the delaminated edges.

Overall, the model can predict the piezoresistive behaviour of an integrated coating-substrate system under perfect and imperfect bonding conditions. Further analysis could be done to include effect of bending on this behaviour. The study could also be improved to predict piezoresistive performance of the integrated system in a mechanically dynamic environment.

Chapter 6

Recommendations for Future Work

This research program has made noteworthy contributions in the areas of fabrication of coating-based piezoresistive systems for damage detection protocol and the development of analytical models to predict the effect of interfacial stresses, material, and geometric properties on the coating-based piezoresistive system. However, these contributions can be further enhanced and expanded. Few recommendations for conducting further research in these areas can be provided as follows:

- It was noticed in the research that the relative change in electrical resistance for the cyclic loading was inconsistent for the first 250-300 cycles. This was attributed to collapse of the pores for this duration since flame spray technique produce relatively high porosity than some other thermal spray technique. Therefore, densification of the coating through other thermal spray techniques that produce relatively less porous coating or carrying out a postprocessing, thermal spray techniques for denser coating for a more consistent electrical resistance change could overcome this phenomenon. The thermal spray technique that would be employed could also be one that can control final composition of the deposited mechanically blended coating powders.

- Another issue with the coating was that it failed under uniaxial loading before the failure of the flat steel substrate. Though the coating appeared to remain intact under cyclic loading, its behavior under uniaxial tensile loading is important. In this case, a thermal

sprayed coating that will produce a deposited stretchable coating will be very significant in overcoming this problem.

- Flame-sprayed technique produce coatings that have anisotropic properties. In the analytical modelling, the effective material properties of the coating layers were used. The analytical model provided the flexibility of knowing the exact material and geometric properties that influence the piezoresistive response of the coating-substrate system. Therefore, a more robust model can be developed to incorporate the random porosities common with flame spray technique and allow for a more accurate model that predicts the piezoresistive performance of the system.

- Integrated coating-substrate systems are subjected to different loading conditions and not just uniaxial loading as done in this program. To give a more accurate account of what happens during working conditions of the integrated system, more loading conditions can be incorporated. This will open up the possibility of integrating multi-axial loading and temperature effects on the system. Also, the model could be extended to damage detection in cylindrical samples. Essentially, 3-D models would be required in these cases.

References

[1] Farrar CR, Worden K. "An introduction to structural health monitoring," *Phil. Trans. R. Soc*. *A:Mathematical, Physical and Engineering Sciences* 2007; 365:303–15. https://doi.org/10.1098/rsta.2006.1928.

[2] Farrar CR, Doebling SW, Nix DA. "Vibration-based structural damage identification," *Phil. Trans. R. Soc. A: Mathematical, Physical and Engineering Sciences* 2001;359:131–49. https://doi.org/10.1098/rsta.2000.0717.

[3] Reed R, Smith J, Christ B. "The economic effects of fracture in the United States," Natl. Bur. Stand. 1983: 647-1:1–7.

[4] Inflation Calculator, available at https://www.bankofcanada.ca/rates/related/inflation-calculator/

[5] Eldukair Z, Ayyub B. "Analysis of Recent U.S Structural and Construction Failures," *J. Perform. Constr. Facil*.1991;5:57–73.

[6] Li D, Ho SCM, Song G, Ren L, Li H. "A review of damage detection methods for wind turbine blades," *Smart Mater. Struct.* 2015;24. https://doi.org/10.1088/0964-1726/24/3/033001.

[7] Du Y, Zhou S, Jing X, Peng Y, Wu H, Kwok N. "Damage detection techniques for wind turbine blades: A review," *Mech. Syst. Signal Process.* 2020;141. https://doi.org/10.1016/j.ymssp.2019.106445.

[8] Kim H, Melhem H. "Damage detection of structures by wavelet analysis," *Eng. Struct.* 2004;26:347–62. https://doi.org/10.1016/j.engstruct.2003.10.008.

[9] Martucci D, Civera M, Surace C. "The extreme function theory for damage detection: An application to civil and aerospace structures," *Appl. Sci.* 2021;11:1–23. https://doi.org/10.3390/app11041716.

[10] Gholizadeh S. "A review of non-destructive testing methods of composite materials," Procedia Struct. Integr. 2016;1:50–7. https://doi.org/10.1016/j.prostr.2016.02.008.

[11] Matveenko V, Kosheleva N, Serovaev G. "Damage detection in materials based on strain measurements," *Acta Mech*. 2021;232:1841–51. https://doi.org/10.1007/s00707-020-02830-4.

[12] Schubel PJ, Crossley RJ, Boateng EKG, Hutchinson JR. "Review of structural health and cure monitoring techniques for large wind turbine blades," Renew. Energy 2013;51:113–23. https://doi.org/10.1016/j.renene.2012.08.072.

[13] Hameed Z, Hong YS, Cho YM, Ahn SH, Song CK. "Condition monitoring and fault detection of wind turbines and related algorithms: A review," *Renew. Sust. Energ. Rev* 2009;13:1–39. https://doi.org/10.1016/j.rser.2007.05.008.

[14] Gouldstone C, Brogan J, Greenlaw R, Gambino RJ, Gutleber J, Sampath S, Longtin J. "Embedded resistive strain sensors for harsh environments," 2006 *IEEE Aerospace Conference Proceedings* 2006;10-pp. https://doi.org/10.1109/aero.2006.1656094.

[15] Cheng Y, Ma Y, Li L, Zhu M, Yue Y, Liu W, *et al*. "Bioinspired Microspines for a High-Performance Spray Ti3C2Tx MXene-Based Piezoresistive Sensor." *ACS Nano.* 2020;14:2145–55. https://doi.org/10.1021/acsnano.9b08952.

[16] Nauman S. "Piezoresistive Sensing Approaches for Structural Health Monitoring of Polymer Composites—A Review," Eng. 2021;2:197–226. https://doi.org/10.3390/eng2020013.

[17] Beganovic N, Söffker D. "Structural health management utilization for lifetime prognosis and advanced control strategy deployment of wind turbines: An overview and outlook concerning actual methods, tools, and obtained results," *Renew. Sust. Energ. Rev.* 2016;64:68–83. https://doi.org/10.1016/j.rser.2016.05.083.

[18] Montemor MF. "Functional and smart coatings for corrosion protection: A review of recent advances," Surf. Coat. Technol. 2014;258:17–37. https://doi.org/10.1016/j.surfcoat.2014.06.031.

[19] Zhang Y, Wang YC, Bailey CG, Taylor AP. "Global modelling of fire protection performance of intumescent coating under different cone calorimeter heating conditions," *Fire Saf. J.* 2012;50:51–62. https://doi.org/10.1016/j.firesaf.2012.02.004.

[20] Smith GM, Higgins O, Sampath S. "In-situ observation of strain and cracking in coated laminates by digital image correlation," *Surf. Coat. Technol.* 2017;328:211–8. https://doi.org/10.1016/j.surfcoat.2017.08.057.

[21] Tucker Jr. RC. Introduction to Thermal Spray Technology, Thermal Spray Technology, ASM Handbook, edited by Robert C., Tucker Jr., ASM International. 2013; 5A:3–9, https://doi.org/10.31399/asm.hb.v05a.a0005706

[22] Li GR, Lv BW, Yang GJ, Zhang WX, Li CX, Li CJ. "Relationship Between Lamellar Structure and Elastic Modulus of Thermally Sprayed Thermal Barrier Coatings with Intra-splat Cracks," *J. Therm. Spray Technol*. 2015;24:1355–67. https://doi.org/10.1007/s11666-015-0292-5.

[23] Roy M, Pauschitz A, Bernardi J, Koch T, Franek F. "Microstructure and mechanical properties of HVOF sprayed nanocrystalline Cr_3C_2-25(Ni20Cr) coating," *J. Therm. Spray Technol*. 2006;15:372–81. https://doi.org/10.1361/105996306X124374.

[24] Vardelle A, Moreau C, Akedo J, Ashrafizadeh H, Berndt CC, Berghaus JO, *et al.* "The 2016 Thermal Spray Roadmap," *J. Therm. Spray Technol.* 2016;25:1376–440. https://doi.org/10.1007/s11666-016-0473-x.

[25] Li CJ, Yang GJ, Li CX. "Development of particle interface bonding in thermal spray coatings: A review," *J. Therm. Spray Technol*.2013;22:192–206. https://doi.org/10.1007/s11666-012-9864-9.

[26] Knotek, O and Elsing, R. "Monte Carlo Simulation of the Lamellar Structure of Thermally Sprayed Coatings," *Surf. and Coat. Technol.* 1987:32:261-271

[27] Sharma A, Gambino RJ, Sampath S. "Anisotropic electrical properties in thermal spray metallic coatings," *Acta Mater.* 2006;54:59–65. https://doi.org/10.1016/j.actamat.2005.08.029.

[28] Kumar A, Nayak SK, Bijalwan P, Dutta M, Banerjee A, Laha T. "Optimization of mechanical and corrosion properties of plasma sprayed low-chromium containing Fe-based amorphous/nanocrystalline composite coating," *Surf. Coat. Technol.* 2019;370:255–68. https://doi.org/10.1016/j.surfcoat.2019.05.010.

[29] Movahedi B, Enayati MH, Wong CC. "Structural and thermal behavior of Fe-Cr-Mo-P-B-C-Si amorphous and nanocrystalline HVOF coatings," *J. Therm. Spray Technol.* 2010;19:1093–9. https://doi.org/10.1007/s11666-010-9507-y.

[30] Rani M, Perumal G, Roy M, Grewal HS, Singh H, Arora HS. "Post-processing of Ni-Cr-Al_2O_3 Thermal Spray Coatings Through Friction Stir Processing for Enhanced Erosion–Corrosion Performance," *J. Therm. Spray Technol*. 2019;28:1466–77. https://doi.org/10.1007/s11666-019-00891-z.

[31] Torres B, Garrido MA, Rico A, Rodrigo P, Campo M, Rams J. "Wear behaviour of thermal spray Al/SiCp coatings," *Wear* 2010;268:828–36. https://doi.org/10.1016/j.wear.2009.12.006.

[32] Branland N, Meillot E, Fauchais P, Vardelle A, Gitzhofer F, Boulos M. "Relationships between microstructure and electrical properties of RF and DC plasma-sprayed titania coatings," *J. Therm. Spray Technol*. 2006;15:53–62. https://doi.org/10.1361/105996306X92596.

[33] Prudenziati M, Gualtieri ML. "Electrical properties of thermally sprayed Ni- and Ni20Cr-based resistors," *J. Therm. Spray Technol*. 2008;17:385–94. https://doi.org/10.1007/s11666-008-9187-z.

[34] Prudenziati M, Cirri G, Bo PD. Novel high-temperature reliable heaters in plasma spray technology. *J. Therm. Spray Technol*. 2006;15:329–31. https://doi.org/10.1361/105996306X124293.

[35] Huonnic N, Abdelghani M, Mertiny P, McDonald A. "Deposition and characterization of flame-sprayed aluminum on cured glass and basalt fiber-reinforced epoxy tubes," *Surf. Coat. Technol.* 2010;205:867–73. https://doi.org/10.1016/j.surfcoat.2010.08.029.

[36] Fasching M, Prinz FB, Weiss LE. " Smart " Coatings : A Technical Note. *J. Therm. Spray Technol*. 1995;4:133–6.

[37] Longtin J, Sampath S, Tankiewicz S, Gambino RJ, Greenlaw RJ. "Sensors for Harsh Environments by Direct-Write Thermal Spray," *IEEE Sens. J.* 2004;4:118–21. https://doi.org/10.1109/JSEN.2003.822218.

[38] Longtin J, Sampath S, Gambino RJ, Tankiewicz S, Greenlaw R. "Sensors for Harsh Environments by Direct Write Thermal Spray," *IEEE Sens. J.* 2002;1:598–601.

[39] Gonzalez R, McDonald AG, Mertiny P. "Damage detection method for fiber-reinforced polymer composites using Al-12Si flame-sprayed coatings," *Int. SAMPE tech. conf. ser.* 2014:1–8.

[40] Gonzalez, R., McDonald, AG, Mertiny, P. "Effect of flame-sprayed Al–12Si coatings on the failure behaviour of pressurized fibre-reinforced composite tubes," *Polym. Test.* 2013:32;1522-28.

[41] Panozzo F, Zappalorto M, Quaresimin M. "Analytical model for the prediction of the piezoresistive behavior of CNT modified polymers," *Compos. B. Eng.* 2017;109:53–63. https://doi.org/10.1016/j.compositesb.2016.10.034.

[42] Wang Z, Ye X. "An investigation on piezoresistive behavior of carbon nanotube/polymer composites: II. Positive piezoresistive effect," *Nanotechnology* 2014;25. https://doi.org/10.1088/0957-4484/25/28/285502.

[43] Zhu S, Chung DDL. "Analytical model of piezoresistivity for strain sensing in carbon fiber polymer-matrix structural composite under flexure," *Carbon* 2007;45:1606–13. https://doi.org/10.1016/j.carbon.2007.04.012.

[44] Kuronuma Y, Takeda T, Shindo Y, Narita F, Wei Z. Electrical resistance-based strain sensing in carbon nanotube/polymer composites under tension: Analytical modeling and experiments. *Compos Sci Technol*. 2012;72:1678–82. https://doi.org/10.1016/j.compscitech.2012.07.001.

[45] Wan KT, Leung CKY, Olson NG. "Investigation of the strain transfer for surface-attached optical fiber strain sensors," *Smart Mater. Struct.* 2008;17. https://doi.org/10.1088/0964-1726/17/3/035037.

[46] Santagata F, Iervolino E, Mele L, van Herwaarden AW, Creemer JF, Sarro PM. "An analytical model and verification for MEMS Pirani gauges," *J Micromech Microeng*. 2011;21. https://doi.org/10.1088/0960-1317/21/11/115007.

[47] Xu D, Xiong B, Wang Y. "Modeling of front-etched micromachined thermopile IR detector by CMOS technology," *J Microelectromech Syst*. 2010;19:1331–40. https://doi.org/10.1109/JMEMS.2010.2076790.

[48] Xu D, Wang Y, Xiong B, Li T. "MEMS-based thermoelectric infrared sensors: A review," *Frontiers of Mechanical Engineering* 2017;12:557–66. https://doi.org/10.1007/s11465-017-0441-2.

[49] Moradi M, Sivoththaman S. “Strain transfer analysis of surface-bonded MEMS strain sensors,” *IEEE Sens. J.* 2013;13:637–43. https://doi.org/10.1109/JSEN.2012.2225043.

[50] Hindrichsen CG, Lou-Møller R, Hansen K, Thomsen E v. “Advantages of PZT thick film for MEMS sensors,” Sens Actuators A Phys 2010;163:9–14. https://doi.org/10.1016/j.sna.2010.05.004.

[51] Dorner-Reisel A, Reisel G, Seeger J, Svoboda S, Akhtar WAA. “Thermally sprayed coatings for protection of integrated sensor systems on tribological loaded surfaces,” *Surf. Coat. Technol.* 2021;424. https://doi.org/10.1016/j.surfcoat.2021.127619.

[52] Gonzalez R, McDonald A, Mertiny P. Effect of flame-sprayed Al-12Si coatings on the failure behaviour of pressurized fibre-reinforced composite tubes. Polym Test 2013;32:1522–8. https://doi.org/10.1016/j.polymertesting.2013.10.002.

[53] Zhou XP, Hu X bin, Xu YS. “The Microstructure and Properties of Coating from Mo2FeB 2 Cermet on Surface of H13 Steel by Reactive Flame Spraying,” *Adv. Mat. Res,* 2010 ; 97–101:1321–7. https://doi.org/10.4028/www.scientific.net/AMR.97-101.1321.

[54] Li Y, Khor KA. Li, Y. “A study of processing parameters in thermal-sprayed alumina and zircon mixtures,” *J. Therm. Spray Technol*. 2002;11:186-194.

[55] Schafft HA and Suehle JS. “The measurement, use and interpretation of the temperature coefficient of resistance of metallizations,” *Solid-state electronics* 1992;35:403-410.

[56] Oliver WC, Pharr GM. “An improved technique for determining hardness and elastic modulus using load and displacement sensing indentation experiments,” *J. Mater. Res.* 1992;7:1564–83. https://doi.org/10.1557/jmr.1992.1564.

[57] Wen W, Becker AA, and Sun W. “Determination of material properties of thin films and coatings using indentation tests: a review” *Journal of Materials Science*, 2017;52:12553-12573.

[58] Vullo V. “Circular Cylinders and Pressure Vessels, ” Stress Analysis and Design; *Springer: Berlin/Heidelberg*, Germany 2014.

[59] Ugural AC, Fenster SK. “Advanced strength and applied elasticity,” *Pearson education*; 2003.

[60] Faupel JH. “Yield and bursting characteristics of heavy-wall cylinders,” *Transactions of the American Society of Mechanical Engineers*. 1956;78:1031-61.

[61] Jorgensen SM. “Overstrain and bursting strength of thick-walled cylinders,” *Transactions of the American Society of Mechanical Engineers*. 1958;80:561-7.

[62] Elton, LRB, Jackson, DF, “X-ray diffraction and the Bragg law”, *American Journal of Physics*, 1966;34:1036-8.

[63] Callus PJ, Berndt CC. “Relationships between the mode II fracture toughness and microstructure of thermal spray coatings,” *Surf. Coat. Technol.* 1999;114:114-28.

[64] Yi Z, Liu J, Wei W, Wang J, Lee SW. "Photocatalytic performance and microstructure of thermal-sprayed nanostructured TiO_2 coatings," *Ceram. Int.* 2008;34:351–7. https://doi.org/10.1016/j.ceramint.2006.10.023.

[65] Boire-Lavigne S, Moreau C, Saint-Jacques RG. "The relationship between the microstructure and thermal diffusivity of plasma-sprayed tungsten coatings" *J. Therm. Spray Technol*.1995;4(3):261-7.

[66] Wu J, Guo HB, Zhou L, Wang L, Gong SK. "Microstructure and thermal properties of plasma sprayed thermal barrier coatings from nanostructured YSZ," *J. Therm. Spray Technol*. 2010;19:1186–94. https://doi.org/10.1007/s11666-010-9535-7.

[67] Li CJ, Ohmori A. "Relationships between the microstructure and properties of thermally sprayed deposits," *J. Therm. Spray Technol*. 2002;11(3):365-74.

[68] Garcia E, Miranzo P, Soltani R, Coyle TW. "Microstructure and thermal behavior of thermal barrier coatings," *J. Therm. Spray Technol*. 2008;17:478–85. https://doi.org/10.1007/s11666-008-9200-6.

[69] Li C, Ohmori A, McPherson R. "The relationship between microstructure and Young's modulus of thermally sprayed ceramic coatings," *J. Mater. Sci. Technol.*1997;32(4):997-1004.

[70] Rezvani Rad M, Ngaokere K, Lloyd SM, McDonald A. "Techno-Economic Assessment of Three-Layered Coating-Based Resistive Heating Systems and Conventional Heat Tracing Cables for Industry Pipes," *J. Therm. Spray Technol*. 2021;30:1393–409. https://doi.org/10.1007/s11666-021-01203-0.

[71] Yao JT, Li CJ, Li Y, Chen B, Huo H bin. "Relationships between the properties and microstructure of Mo-Cu composites prepared by infiltrating copper into flame-sprayed porous Mo skeleton," *Mater. Des*. 2015;88:774–80. https://doi.org/10.1016/j.matdes.2015.09.062.

[72] Yao JT, Ren JQ, Huo H bin, Yang GJ, Li CX, Li CJ. "Deposition behavior of semi-molten spray particles during flame spraying of porous metal alloy," *J. Therm. Spray Technol*. 2014;23:991–9. https://doi.org/10.1007/s11666-014-0119-9.

[73] Karimi MR, Salimijazi HR, Golozar MA. "Effects of remelting processes on porosity of NiCrBSi flame sprayed coatings," *Surf. Eng.* 2016;32:238–43. https://doi.org/10.1179/1743294415Y.0000000107.

[74] Ashrafizadeh H, McDonald A, Mertiny P. "Deposition of Electrically Conductive Coatings on Castable Polyurethane Elastomers by the Flame Spraying Process," *J. Therm. Spray Technol*. 2016;25:419–30. https://doi.org/10.1007/s11666-015-0376-2.

[75] Zhang XC, Xu BS, Xuan FZ, Tu ST, Wang HD, Wu YX. "Porosity and effective mechanical properties of plasma-sprayed Ni-based alloy coatings," *Appl. Surf. Sci.* 2009;255:4362–71. https://doi.org/10.1016/j.apsusc.2008.10.120.

[76] Pilliar RM, Nutting J. “Solid-solid interfacial energy determinations in metal-ceramic systems,” *Philos. Mag.* 1967;16:181–8. https://doi.org/10.1080/14786436708229267.

[77] Johnson KL, Kendall K, Roberts A. “Surface energy and the contact of elastic solids,” *Proc. R. Soc. A: Math*. 1971;324(1558):301-13.

[78] Rhee SK. “A Method for Determining Surface Energy of Solids,” *Mater. Sci. Eng.* 1973;9:311-8.

[79] Linford RG. “Surface energy of solids,” *Chemical Society Reviews.* 1972;1(4):445-64.

[80] Kendall K. “The adhesion and surface energy of elastic solids,” *Journal of Physics D: Applied Physics*. 1971 Aug 1;4(8):1186.

[81] Geguzin YE, Ovcharenko NN. “Surface energy and surface processes in solids,” *Soviet Physics Uspekhi.*1962;5(1):129.

[82] Jin C, Wang X. “Analytical modelling of the electromechanical behaviour of surface-bonded piezoelectric actuators including the adhesive layer,” *Eng. Fract. Mech*. 2011;78:2547–62. https://doi.org/10.1016/j.engfracmech.2011.06.014.

[83] Zhang J, Zhang B, Fan J. “A coupled electromechanical analysis of a piezoelectric layer bonded to an elastic substrate: Part I, development of governing equations,” *Int. J. Solids Struct.* 2003;40:6781–97. https://doi.org/10.1016/S0020-7683(03)00307-X.

[84] Hosseini Y, Kermanpur A, Ashrafizadeh F, Keyvani A. “Enhancing hot oxidation resistance of the HVOF-sprayed NiCoCrAlTaY coating by alumina nanoparticles via a modified suspension route,” *J. Mater. Res. Technol.* 2022. https://doi.org/10.1016/j.jmrt.2022.12.185.

[85] Li B, Fan X, Okada H, Wang T. “Mechanisms governing the failure modes of dense vertically cracked thermal barrier coatings,” *Eng. Fract. Mech*. 2018;189:451–80. https://doi.org/10.1016/j.engfracmech.2017.11.037.

[86] Sugiura, T, Takahashi, N, Nakano, N. “The piezoresistive mobility modeling for cubic and hexagonal silicon carbide crystals”, *Journal of Applied Physics*. 2020;127:245113.

[87] Ultra strength chemical resistant paek and carbon fiber sheets, 2022. Available at https://www.mcmaster.com/products/carbon-fiber/easy-to-form-ultra-strength-chemical-resistant-paek-and-carbon-fiber-sheets/

[88] Sehr S, Amidi S, Begley MR. “Interface delamination vs. bulk cracking along wavy interfaces,” Eng. Fract. Mech. 2019;206:64–74. https://doi.org/10.1016/j.engfracmech.2018.10.031.

[89] Chai H, Fox J. “On delamination growth from channel cracks in thin-film coatings,” *Int. J. Solids Struct.* 2012;49:3142–7. https://doi.org/10.1016/j.ijsolstr.2012.06.012.

[90] McPherson R. “A review of microstructure and properties of plasma sprayed ceramic coatings,” *Surf. Coat. Technol.* 1989;39:173-81.

[91] Verwer K, Eberli GP, Weger RJ. “Effect of pore structure on electrical resistivity in carbonates,” *Am. Assoc. Pet. Geol. Bull.* 2011;95:175–90. https://doi.org/10.1306/06301010047.

[92] Montes JM, Cuevas FG, Reina FJV, Ternero F, Astacio R, Caballero ES, *et al.* “Modelling and Simulation of the Electrical Resistance Sintering Process of Iron Powders,” *Met. Mater. Int.* 2020;26:1045–59. https://doi.org/10.1007/s12540-019-00366-4.

[93] Man HN and Jing XD. “Pore network modelling of electrical resistivity and capillary pressure characteristics,” *Transp. Porous Media*. 2000;41(3):263-85.

[94] Montes JM, Cuevas FG, Cintas J. “Electrical resistivity of metal powder aggregates,” *Metall. Mater. Trans. B* 2007;38:957–64. https://doi.org/10.1007/s11663-007-9097-3.

[95] Montes JM, Cuevas FG, Cintas J. “Porosity effect on the electrical conductivity of sintered powder compacts,” *Appl. Phys. A Mater. Sci. Process* 2008;92:375–80. https://doi.org/10.1007/s00339-008-4534-y.

[96] Montes JM, Cuevas FG, Cintas J. “Electrical resistivity of a titanium powder mass,” *Granul. Matter.* 2011;13:439–46. https://doi.org/10.1007/s10035-010-0246-z.

[97] Qiu A, Li P, Yang Z, Yao Y, Lee I, Ma J. “A Path Beyond Metal and Silicon:Polymer/Nanomaterial Composites for Stretchable Strain Sensors,” *Adv. Funct. Mater.* 2019;29. https://doi.org/10.1002/adfm.201806306.

[98] Pujilaksono B, Jonsson T, Halvarsson M, Panas I, Svensson JE, Johansson LG. “Paralinear oxidation of chromium in O_2 + H_2O environment at 600-700°C,” *Oxid. of Met.* 2008;70:163–88. https://doi.org/10.1007/s11085-008-9114-1.

[99] Hoffmann, K. "An introduction to stress analysis and transducer design using strain gauges." *HBM Test and Measurement*. 2012:126-209.

[100] Wang X, Meguid S. “On the electroelastic behaviour of a thin piezoelectric actuator attached to an infinite host structure,” *Int. J. Solids Struct.* 2000;37:3231–51.

[101] Yu H, Wang X. “Modelling and simulation of surface-bonded piezoelectric actuators with bending effects,” J. Intell. Mater. Syst. Struct. 2017;28:507–20. https://doi.org/10.1177/1045389X16649701.

[102] Hu H, Li Z, Wang X. “Modelling and analysis of piezoelectric actuators with partially debonded adhesive layers,” *Math. Mech. Solids* 2021;26:722–37. https://doi.org/10.1177/1081286520966032.

[103] Ciampolini P, Rossi A, Pierantoni A, Rudan M. “Electro-elastic simulation of a piezoresistive pressure sensor,” *Microelectronics journal*. 1995;26(2-3):265-72.

[104] Wu M, Huang L, Zhang X, Chen J, Lv Y. “Two-dimensional piezoresistive response and measurement of sensitivity factor of polymer-matrix carbon fiber mat. *Polymers* (Basel) 2020;12:1–9. https://doi.org/10.3390/polym12123072.

[105] Koo GM, Tallman TN. “On the Development of Tensorial Deformation-Resistivity Constitutive Relations in Conductive Nanofiller-Modified Composites,” *InSmart Materials, Adaptive Structures and Intelligent Systems*. 2018:51951

[106] Zhao Z, Zheng H, Wen A, Li J. “Theory of Piezoresistive Response of Unidirectional CFRP under Spatial Stress,” *IOP Conf. Ser. Mater. Sci. Eng*, vol. 382, Institute of Physics Publishing; 2018. https://doi.org/10.1088/1757-899X/382/4/042060.

[107] Burmister DM. “The general theory of stresses and displacements in layered systems,” *I. J. Appl. Phys.* 1945;16:89–94. https://doi.org/10.1063/1.1707558.

[108] Burmister DM. “The general theory of stresses and displacements in layered soil systems. III.,” *J. Appl. Phys*. 1945;16:296–302. https://doi.org/10.1063/1.1707590.

[109] Yu H, Wang X. Modelling and simulation of surface-bonded piezoelectric actuators with bending effects. *J. Intell. Mater. Syst. Struct.* 2017;28:507–20. https://doi.org/10.1177/1045389X16649701.

[110] Richard CS, Beranger G, Lu J, Flavenot JF. “The influences of heat treatments and interdiffusion on the adhesion of plasma-sprayed NiCrAlY coatings,” *Surf. Coat. Technol.* 1996;82:99-109.

[111] Hsueh CH, Lee S, Lin HY. “Analyses of mode I edge delamination by thermal stresses in multilayer systems,” *Compos. B Eng.* 2006;37:1–9. https://doi.org/10.1016/j.compositesb.2005.05.005.

[112] Kovářík O, Siegl J, Nohava J, Chráska P. “Young’s modulus and fatigue behavior of plasma-sprayed alumina coatings,” *J. of Therm. Spray Technol.* 2005;14:231–8. https://doi.org/10.1361/105996304523809.

[113] Bandyopadhyay PP, Chicot D, Venkateshwarlu B, Racherla V, Decoopman X, Lesage J. “Mechanical properties of conventional and nanostructured plasma sprayed alumina coatings,” *Mech. Mater.* 2012;53:61–71. https://doi.org/10.1016/j.mechmat.2012.05.006.

[114] Hu H, Li Z, Wang X. Modelling and analysis of piezoelectric actuators with partially debonded adhesive layers. *Math. Mech. Solids.* 2021;26:722–37. https://doi.org/10.1177/1081286520966032.

[115] Tong L, Sun D, Atluri SN. “Sensing and actuating behaviours of piezoelectric layers with debonding in smart beams,” *Smart materials and structures.* 2001;10(4):713.

[116] Muskhelishvili NI. Some Basic Problems of the Mathematical Theory of Elasticity. Springer Netherlands; 1977. https://doi.org/10.1007/978-94-017-3034-1.

Appendix

A-1 Piezoresistive Equations

The structural and electrical fields for a piezoresistive component are coupled by means of piezoresistive coefficients matrix[α]:

$$\left\{\frac{\rho_i}{\rho_o}\right\} = [\alpha]\{\sigma\} \tag{A-1}$$

For a material with cubic symmetry, Eq. A-1 can be expressed as:

$$\begin{bmatrix} \Delta\rho_1/\rho_o \\ \Delta\rho_2/\rho_o \\ \Delta\rho_3/\rho_o \\ \Delta\rho_4/\rho_o \\ \Delta\rho_5/\rho_o \\ \Delta\rho_6/\rho_o \end{bmatrix} = \begin{bmatrix} \alpha_{11} & \alpha_{12} & \alpha_{12} & 0 & 0 & 0 \\ \alpha_{12} & \alpha_{11} & \alpha_{12} & 0 & 0 & 0 \\ \alpha_{12} & \alpha_{12} & \alpha_{11} & 0 & 0 & 0 \\ 0 & 0 & 0 & \alpha_{44} & 0 & 0 \\ 0 & 0 & 0 & 0 & \alpha_{44} & 0 \\ 0 & 0 & 0 & 0 & 0 & \alpha_{44} \end{bmatrix} \begin{bmatrix} \sigma_1 \\ \sigma_2 \\ \sigma_3 \\ \sigma_4 \\ \sigma_5 \\ \sigma_6 \end{bmatrix} \tag{A-2}$$

where

$\frac{\rho_i}{\rho_o}$, for i = 1,2...,6 is the relative change in electrical resistivity

ρ_o is the electrical resistivity without mechanical load

$[\alpha]$ is the piezoresistive coefficients matrix

$\{\sigma\}$ is the stress vector

The longitudinal relative electrical resistance change is given by:

$$\frac{\Delta R_1}{R_o} = (1+2v)\varepsilon_x + \frac{\Delta \rho_1}{\rho_o}. \tag{A-3}$$

Substituting Eq. A-2 into A-3 for $\frac{\Delta \rho_1}{\rho_o}$ gives: $\frac{\Delta R_1}{R_o} = (1+2v)\varepsilon_x + \alpha_{11}\sigma_1 + \alpha_{12}\sigma_2 + \alpha_{12}\sigma_3$. (A-4)

With the loading conditions and assumptions in Chapter 4:

$$\frac{\Delta R_1}{R_o} = (1+2v)\varepsilon_x + \alpha_{11}\sigma_1. \tag{A-5}$$

With the loading conditions and assumptions in Chapter 5:

$$\frac{\Delta R_1}{R_o} = (1+2v)\varepsilon_x + \alpha_{11}\sigma_1 + \alpha_{12}\sigma_3 \tag{A-6}$$

A-2 Properties of Chebyshev Polynomials used in this Work.

The following properties of the Chebyshev polynomials were used in this work:

$$\int_{-1}^{s}\frac{T(r)}{\sqrt{1-r^2}}dr=\begin{cases}-\dfrac{1}{n}U_{n-1}(s)\sqrt{1-s^2} & n>0\\ \pi-\cos^{-1}(s) & n=0\end{cases}. \tag{A-7}$$

$$\frac{1}{\pi}\int_{-1}^{1}\frac{T_n(r)T_m(r)}{\sqrt{1-r^2}}dr=\begin{cases}0 & m\neq n\\ 1 & m=n=0\\ \dfrac{1}{2} & m=n\geq 1\end{cases}. \tag{A-8}$$

$$\frac{1}{\pi}\int_{-1}^{1}\frac{T_n(r)T_m(r)}{(r-s)\sqrt{1-r^2}}dr=\begin{cases}0 & n=0,|s|<1\\ U_{n-1}(s) & n>0,|s|<1\\ \dfrac{-\left(s-\text{sign}(s)\sqrt{s^2-1}\right)^n}{sign(s)\sqrt{s^2-1}} & n\geq 0,|s|>1\end{cases}. \tag{A-9}$$